

A Conservative Discontinuous Galerkin Discretization for the Chemically Reacting Navier-Stokes Equations

Ryan F. Johnson and Andrew D. Kercher

Laboratories for Computational Physics and Fluid Dynamics, U.S. Naval Research Laboratory, 4555 Overlook Ave SW, Washington, DC 20375

Abstract

We present a detailed description and verification of a discontinuous Galerkin finite element method (DG) for the multi-component chemically reacting compressible Navier-Stokes equations that retains the desirable properties of DG, namely discrete conservation and high-order accuracy in smooth regions of the flow. Pressure equilibrium between adjacent elements is maintained through the consistent evaluation of the thermodynamics model and the resulting weak form, as well as the proper choice of nodal basis. As such, the discretization does not generate unphysical pressure oscillations in smooth regions of the flow or at material interfaces where the temperature is continuous. Additionally, we present an *hp*-adaptive DG method for solving systems of ordinary differential equations, DGODE, which is used to resolve the temporal evolution of the species concentrations due to stiff chemical reactions. The coupled solver is applied to several challenging test problems including multi-component shocked flows as well as chemically reacting detonations, deflagrations, and shear flows with detailed kinetics. We demonstrate that the discretization does not produce unphysical pressure oscillations and, when applicable, we verify that it maintains discrete conservation. The solver is also shown to reproduce the expected temperature and species profiles throughout a detonation as well as the expected two-dimensional cellular detonation structure. We also demonstrate that the solver can produce accurate, high-order, approximations of temperature and species profiles without artificial stabilization for the case of a one-dimensional pre-mixed flame. Finally, high-order solutions of two- and three-dimensional multi-component chemically reacting shear flows, computed without any additional stabilization, are presented.

Keywords: High order finite elements; Discontinuous Galerkin method; Chemistry; Combustion;

1. Introduction

In this work we provide a detailed description and verification of a conservative, high-order, method for the multi-component chemically reacting Navier-Stokes flows [1]. The method is based on the discontinuous Galerkin finite element method (DG) [2, 3, 4, 5, 6, 7, 8, 9, 10, 11, 12, 13, 14], which has become an increasingly popular approach for modeling a wide range of fluid dynamics. This is due to the fact that the method is fully conservative, able to achieve high-order accuracy on unstructured grids, and it naturally supports local polynomial, p , adaptivity. Furthermore, in contrast to the continuous Galerkin finite element method, DG does not require additional stabilization for pure advection problems. As such, DG has the potential to be a powerful tool for simulating multi-component chemically reacting flows. However, previous applications of DG to multi-component chemically reacting flows were not capable of maintaining pressure equilibrium, which resulted in unphysical pressure oscillations not only at material interfaces but in smooth regions of the flow [15, 16]. These unphysical oscillations were suppressed by incorporating a nonconservative flux,

Distribution A. Approved for public release: distribution unlimited.

an approach previously developed in the context of finite volume methods, where the discrete solution is inherently discontinuous. This approach is known as the *double flux method*, and it has the undesirable effect that the discretization no longer achieves the discrete conservation of energy, which is critical for the reliable approximation of shock locations and speeds, as well as the correct determination of heat release in combustion processes.

In this work, we present a DG discretization for the multi-component chemically reacting Navier-Stokes equations that does not generate unphysical pressure oscillations in smooth regions of the flow and across material interfaces when the temperature is continuous without the use of additional stabilization. This is achieved by

- Evaluating the thermodynamics exactly, i.e., defining temperature such that the internal energy of a discrete solution and the species weighted polynomial representation for internal energy are equivalent.
- Representing the discrete solution in terms of a nodal basis with coefficients defined on the element interfaces so that pressure equilibrium between adjacent elements is maintained in smooth regions of the flow as well as defining the basis coefficients of the nonlinear flux, which is used to numerically evaluate the resulting weak form, in a manner that maintains pressure equilibrium.

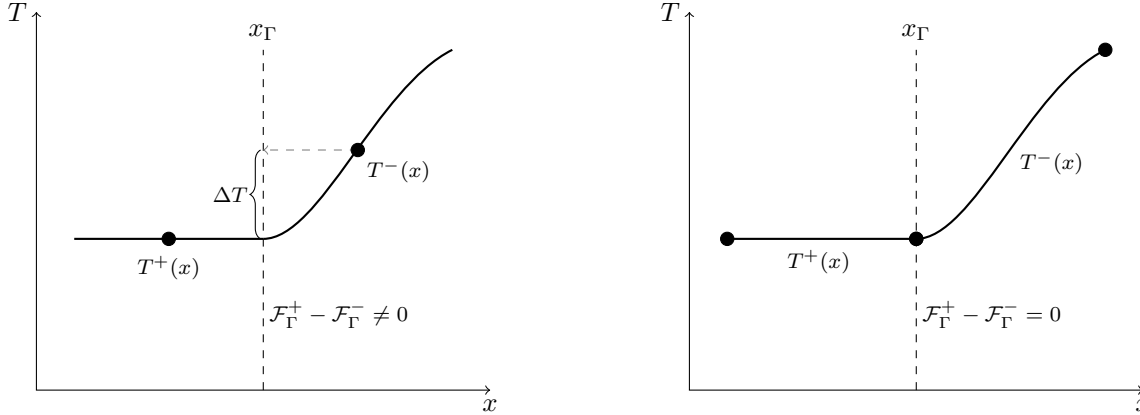
By preserving pressure equilibrium between adjacent elements in smooth regions of the flow at each stage of the approximation, i.e., evaluation of the exact thermodynamics, through the representation of the discrete solution, and approximation of the weak form, the discretization is capable of simulating multi-component flows without generating unphysical pressure oscillations and therefore maintains the desirable properties of DG, namely discrete conservation and high order accuracy for smooth flows. As with all numerical methods for convection dominated flows, instabilities in the solution are generated at discontinuous interfaces, e.g., shocks and detonation fronts, that are not grid aligned. In this case, additional stabilization is required, which we implement via residual based artificial viscosity of the form of [14].

In addition to applying DG to the spatial formulation, we have developed an *hp*-adaptive DG method to solve the ordinary differential equations (ODEs) that describes the time split species evolution for chemically reacting flows. The method, termed DGODE, removes the need for a third party library since it is built on the existing DG infrastructure. Accurate and efficient integration of the potentially stiff chemical source term is ensured via local adaptive refinement of both the temporal resolution, h , as well as the polynomial degree, p . The effectiveness of local *hp*-adaptivity for resolving the disparate chemical times scales is studied in the context of the GRI-3.0 mechanism [17] where the polynomial degree of the local approximation, p , is compared to the stiffness associated with the Jacobian of the chemical source term for both a homogeneous reactor and a one-dimensional C_2H_4 and air detonation wave.

Finally, the coupled reacting Navier-Stokes flow solver is applied to several multi-component non-reacting and chemically reacting test cases in one, two, and three dimensions. In particular, we study a one-dimensional multi-component shock tube and two-dimensional shock-bubble interaction to test the ability of the solver to compute high-order solutions to multi-component high-speed flows. We study a detonation wave in one and two dimensions and analyze the ability of DGODE to locally adapt the polynomial degree in order to accurately and efficiently integrate complex chemical source terms in the presence of non-trivial fluid dynamics. We analyze the conservation error of the formulation for problems with shocks and detonations and comment on the stability for smooth unsteady reacting flows. Where applicable, we present these results in comparison to previous experimental and computational work. Finally, we solve a three-dimensional multi-component chemically reacting shear flow in the presence of a splitter plate to test the ability of the solver to compute high-order solutions of smooth reacting Navier-Stokes flows without the need for additional stabilization.

1.1. Background

Overcoming unphysical pressure oscillations generated at material interfaces of multi-component flows has been one of the primary challenges in the simulation of chemically reacting flows. The source of these oscillations has been attributed to variations in the thermodynamic properties of multi-component gases. Furthermore, it was previously concluded that any fully conservative Godunov-type scheme would be unable



(a) Loss of discrete temperature equilibrium between adjacent elements in the case of low order finite volume methods where piecewise constant, $p = 0$, interpolation is used. High-order reconstruction can reduce the error at the interface but cannot, in general, eliminate it.

(b) Satisfaction of discrete temperature equilibrium in the case of finite element methods, with $p > 0$, where the solution is given in terms of, possibly piecewise, continuous basis functions defined over the element.

Figure 1.1: The loss of temperature equilibrium between adjacent elements leads to unphysical pressure oscillations generated at the interface of adjacent elements where the jump in the normal flux does not vanish, i.e., $\mathcal{F}_\Gamma^+ - \mathcal{F}_\Gamma^- \neq 0$.

to maintain a pressure equilibrium across material fronts [18]. However, the original analysis assumed that the variable ratio of specific heats, γ , was only a function of species concentrations and was frozen at each time step [19, 20]. Jenny et al. [21] also analyzed the conditions under which pressure oscillations are generated and concluded that the pressure remains in equilibrium across a material interface if

1. The interface is grid aligned throughout the time step.
2. The ratio of specific heats, γ , is continuous across the interface.
3. The temperature is continuous across the interface, i.e., discrete temperature equilibrium between adjacent elements is maintained.

Satisfaction of item 1 is outside the scope of this work as it would require an implicit shock-fitting approach [22, 23] or a Lagrangian method for chemically reacting flows [24]. Item 2 represents a special case and is not generally satisfied in multi-component flows. However, item 3 is generally satisfied in smooth regions of the flow, therefore a numerical scheme, if applied to multi-component compressible Navier-Stokes flows, should be capable of satisfying this condition discretely while also maintaining pressure equilibrium.

In the case of finite volume methods, discrete temperature equilibrium is not, in general, easily maintained. For a piece-wise constant discrete solution, i.e., DG($p = 0$), only a constant temperature profile will remain in equilibrium at the interfaces between adjacent elements. In the case of a smoothly varying temperature profile, equilibrium between adjacent elements will be lost, as shown in Figure 1.1a. A more accurate reconstruction of the interface state, based on information from the neighboring elements, may reduce this error, but cannot, in general, eliminate it. Furthermore, the reconstruction would need to maintain equilibrium between all adjacent elements in a fully multi-dimensional setting, where as most reconstruction algorithms are dimensionally split for efficiency. For the DG($p > 0$) discretization described in this work, the discrete solution is given in terms piecewise continuous basis functions with basis coefficients located on the element boundary as shown in Figure 1.1b. As such, interpolation is not required to define the interface state, and discrete equilibrium is automatically maintained between adjacent elements regardless of the dimensional setting.

As with the DG method described in this work, continuous Galerkin finite element methods (CG) also trivially maintain pressure equilibrium between adjacent elements since the discrete solution is continuous throughout the domain by design, see Figure 1.1. However, in contrast to DG methods, CG methods require additional stabilization for smooth convection dominated flows and are therefore not considered in this work.

Alternatively, finite difference methods discretize the strong form of the equations where the discrete solution is coupled through a discrete difference operator applied directly to the, linear or nonlinear, function corresponding to the underlying equation. In the case of computational fluid dynamics, stability of the advection operator is maintained by evaluating the flux at the state with components defined in terms of weighted sums with adjacent elements. The weighted sums are unique for each component of the state, which is problematic for maintaining pressure equilibrium since any deviation in the relationship defining pressure will result in the loss of equilibrium and the subsequent generation of unphysical pressure oscillations.

Due to the difficulties described above, various techniques have been developed for avoiding the generation of unphysical pressure oscillations. A nonconservative approach, referred to as the *double flux method*, is one popular option [25, 26, 27, 15, 16]. The method assumes consistent fluid thermal properties through a material interface, thereby breaking energy conservation but maintaining pressure equilibrium across interfaces. It has been successfully applied to complex multidimensional reacting Navier-Stokes flows, including detonations, in the context of both finite volume [27] and DG discretizations [15, 16] with frozen thermodynamics.

Quasi-conservative methods based on the solution of an additional transport equation for a given function of the ratio of specific heats has been developed. Early attempts using this approach did not conserve species mass concentrations [20], which lead to temperature errors across material interfaces and subsequent unphysical heating due to thermal diffusion. In response, a modified weighted essentially non-oscillatory scheme was developed that solved for the mass fraction in conservative form, thereby preventing temperature and species conservation errors [28].

Methods based on the inclusion of additional transport equations have also been proposed, as reviewed by [29] in their presentation of the five equation quasi-conservative model. This approach employs a number fraction model to avoid pressure oscillations and is applicable to Navier-Stokes flows since it includes the effects of species diffusion, viscosity, and thermal conductivity. Although these methods have been successful at preventing unphysical pressure oscillations, their applicability to chemically reacting flows has yet to be demonstrated. In contrast, the formulation presented in this work is fully conservative and does not require the solution of additional transport equations while being directly applicable to both inviscid and viscous multi-component chemically reacting flows.

Conservative schemes based on exact thermodynamics have also been successfully developed for compressible chemically reacting flows [30, 31, 32, 33, 34, 35]. However, this alone will not prevent the generation of unphysical oscillations at material interfaces. Specifically, oscillations are still generated in smooth regions of the flow if the discrete representation of the solution is discontinuous, as is the case for finite volume and finite difference methods. These oscillations are then suppressed via limiting, artificial viscosity, or filtering.

In the case of structured grids, conservative high-order finite difference methods have been developed for compressible reacting flow problems without shocks [36, 32, 33]. In this approach, a numerical filter is used to create artificial viscosity and suppress unphysical oscillations, for details see [36]. Although high-order finite difference stencils are readily available on the interior of the domain, ensuring the formal order of accuracy of the method at the boundaries of the domain is not always obvious. In some cases, the formal order of accuracy can be ensured through the application of specially derived difference formulas at the boundary. In general, this is not the case, especially when embedded surfaces must be employed to represent non-cartesian aligned geometries. The DG discretization we employ also supports arbitrarily high-order approximations. However, unlike finite difference methods, it is capable of achieving high-order accuracy on unstructured grids and it does not require special treatment at the boundaries. Furthermore, the DG discretization purposed in this work does not require additional stabilization for well resolved smooth flows.

Additionally, finite volume schemes with detailed finite rate chemistry, which derive the exact thermodynamic quantities from the energy have been used to successfully simulate detonations and deflagrations. Methods based on flux corrected transport (FCT) have been used to study two-dimensional cellular detonation structures [30, 35]. These results have been reproduced in two- and three-dimensional simulations using an extended Roe solver for self-sustaining detonations where unphysical oscillations did not corrupt the numerical results [37]. Simulations of detonations were also successfully performed using a second order Godunov scheme and the Colella–Glaz Riemann solver [34]. In this work, we show that the our method

is also capable of simulating self-sustaining detonations, the results of which are reported in Sections 5.3 and 5.4.

In addition, total variational diminishing type finite volume schemes where the exact thermodynamics quantities were derived from the energy have been used to carry out direct numerical simulations. Turbulent three-dimensional flames have been simulated using a finite volume formulation [38]. The interfacial fluxes were computed using an HLLC approximate Riemann solver where the reconstructed solutions at the cell interfaces are limited using the piecewise-parabolic method of Colella and Woodward [39].

In this work we also derive exact thermodynamics quantities from the conserved energy, however, the formulation presented in this work does not require stabilization or limiting in smooth regions of the flow. The formulation is based on a DG discretization, and we show that unphysical pressure oscillations exist as derived by [21], and as detailed in Appendix C. These conclusions are verified in Section 4, where we apply the conservative DG formulation to a series of problems containing various types of material interfaces and analyze the magnitude of pressure oscillations generated.

2. Chemically Reacting Navier-Stokes Equations

Let $\Omega \subset \mathbb{R}^d$ be a given d -dimensional domain. We consider the nonlinear conservation law governing the unsteady chemically reacting Navier-Stokes equations, in strong form, defined for piecewise smooth, \mathbb{R}^m -valued functions y , and gradient ∇y , given as

$$\frac{\partial y}{\partial t} + \nabla \cdot \mathcal{F}(y, \nabla y) - \mathcal{S}(y) = 0 \text{ in } \Omega, \quad (2.1)$$

where $\mathcal{F} : \mathbb{R}^m \rightarrow \mathbb{R}^{m \times d}$ is a given flux function, $\mathcal{S} : \mathbb{R}^m \rightarrow \mathbb{R}^m$ is a given source term, and t denotes time. The flux function

$$F(y, \nabla y) = (\mathcal{F}^c(y) - \mathcal{F}^v(y, \nabla y)) \quad (2.2)$$

is defined in terms of the convective flux $\mathcal{F}^c(y)$, which is only a function of the state y , and viscous flux $\mathcal{F}^v(y, \nabla y)$, which is a function of the state and the gradient, ∇y . The chemically reacting Navier-Stokes flow state variable is given by

$$y = (\rho v_1, \dots, \rho v_d, \rho e_t, C_1, \dots, C_{n_s}), \quad (2.3)$$

where $m = d + n_s + 1$, n_s is the number of thermally perfect species, $\rho : \mathbb{R}^{n_s} \rightarrow \mathbb{R}$ is density, $(v_1, \dots, v_d) : \mathbb{R}^m \rightarrow \mathbb{R}^d$ is velocity, $e_t : \mathbb{R}^m \rightarrow \mathbb{R}$ is the specific total energy, and $C : \Omega \rightarrow \mathbb{R}^{n_s}$ are the species concentrations. The density is calculated from the concentrations as

$$\rho = \sum_{i=1}^{n_s} W_i C_i, \quad (2.4)$$

where W_i is the molecular weight of species i .

The k -th spatial convective flux component is given by

$$\mathcal{F}_k^c(y) = (\rho v_k v_1 + p \delta_{k1}, \dots, \rho v_k v_d + p \delta_{kd}, v_k (\rho e_t + p), v_k C_1, \dots, v_k C_{n_s}). \quad (2.5)$$

The pressure, $p : \mathbb{R}^m \rightarrow \mathbb{R}$, is calculated from the equation of state,

$$p = R^0 T \sum_{i=1}^{n_s} C_i, \quad (2.6)$$

where $T : \mathbb{R}^m \rightarrow \mathbb{R}$, is the temperature and $R^0 = 8314.4621 \text{ J/Kmol/K}$ is the universal gas constant. The total energy, ρe_t , is given as the sum of the internal and kinetic and energies as

$$\rho e_t = \rho u + \frac{1}{2} \sum_{k=1}^d \rho v_k v_k, \quad (2.7)$$

where $\rho u : \mathbb{R}^m \rightarrow \mathbb{R}$ is the internal energy. The internal energy is also defined as the mass weighted sum of thermally perfect species specific internal energies that are n_p -order polynomials with respect to temperature,

$$\rho u = \sum_{i=1}^{n_s} W_i C_i \sum_{k=0}^{n_p} a_{ik} T^k. \quad (2.8)$$

In this work, all thermodynamic polynomials are continuous refits of the analytic form from NASA's polynomial representations [40]. The temperature is defined consistently to ensure equivalency between the definition of internal energy, ρu , given by Equation (2.7) and the definition given by Equation (2.8), i.e., find T such that

$$\begin{aligned} 0 &= \rho u - \sum_{i=1}^{n_s} W_i C_i \sum_{k=1}^K a_{ik} T^k, \\ &= \left(\rho e_t - \frac{1}{2} \sum_{k=1}^d \rho v_k v_k \right) - \sum_{i=1}^{n_s} W_i C_i \sum_{k=1}^K a_{ik} T^k. \end{aligned} \quad (2.9)$$

The temperature is computed such that the following is satisfied to machine precision for a given an initial temperature:

$$\delta T = \frac{\rho u - \sum_{i=1}^{n_s} W_i C_i \sum_{k=1}^K a_{ik} T^k}{\frac{\partial \rho u}{\partial T}}, \quad (2.10)$$

where δT is the temperature decrement corresponding to Newton's method and

$$\frac{\partial \rho u}{\partial T} = \sum_{i=1}^{n_s} W_i C_i \sum_{k=1}^K k a_{ik} T^{k-1} \quad (2.11)$$

is the partial derivative of internal energy with respect to temperature, see Appendix A. In practice, we observe that the temperature converges within five nonlinear iterations with an initial guess of $T = 500$ K. In our experience, divergence of the nonlinear solver very rarely occurs. In the case that the solution does diverge, the cause is attributed to other numerical issues such as negative concentrations. Once the temperature and state are known, pressure is computed by evaluating Equation (2.6) thereby satisfying the thermodynamics state exactly. It is important to note that we do not rely on the ratio of specific heats, γ , to evaluate pressure to calculate the fluxes from the conserved state.

The k -th spatial component of the viscous flux is given by

$$\mathcal{F}_k^v(y, \nabla y) = \left(\tau_{1k}, \dots, \tau_{dk}, \sum_{j=1}^d \tau_{kj} v_j - W_i C_i h_i V_{ik} - q_k, C_1 V_{1k}, \dots, C_{n_s} V_{n_s k} \right), \quad (2.12)$$

where $q : \mathbb{R}^m \times \mathbb{R}^{m \times d} \rightarrow \mathbb{R}^d$ is the thermal heat flux, $\tau : \mathbb{R}^m \times \mathbb{R}^{m \times d} \rightarrow \mathbb{R}^{d \times d}$ is the viscous stress tensor, $(h_1, \dots, h_{n_s}) : \mathbb{R}^m \rightarrow \mathbb{R}^{n_s}$ are the species specific enthalpies, and $((V_{11}, \dots, V_{1d}), \dots, (V_{n_s 1}, \dots, V_{n_s d})) : \mathbb{R}^m \times \mathbb{R}^{n_s \times d} \rightarrow \mathbb{R}^{n_s \times d}$ are the species diffusion velocities. The k -th spatial component of the viscous stress tensor is given by

$$\tau_k(y, \nabla y) = \mu \left(\frac{\partial v_1}{\partial x_k} + \frac{\partial v_k}{\partial x_1} - \delta_{k1} \frac{2}{3} \sum_{j=1}^d \frac{\partial v_j}{\partial x_j}, \dots, \frac{\partial v_d}{\partial x_k} + \frac{\partial v_k}{\partial x_d} - \delta_{kd} \frac{2}{3} \sum_{j=1}^d \frac{\partial v_j}{\partial x_j} \right), \quad (2.13)$$

where $\mu : \mathbb{R}^m \rightarrow \mathbb{R}$ is the dynamic viscosity. The k -th spatial component of the heat flux is given as

$$\begin{aligned} q_k(y, \nabla y) &= -\lambda \sum_{j=1}^m T_{y_j}(y) \frac{\partial y_j}{\partial x_k}, \\ &= -\lambda \frac{\partial T}{\partial x_k}. \end{aligned} \quad (2.14)$$

where $\lambda : \mathbb{R}^m \rightarrow \mathbb{R}$ is the thermal conductivity and where T_{y_j} is the partial derivatives of T with respect to state component y_j , see Appendix A.

The transport properties are calculated using mixture averaged properties. The k -th spatial component of the diffusion velocity for the i -th species is given as

$$V_{ik} = \frac{\bar{D}_i}{C_i} \frac{\partial C_i}{\partial x_k} - \frac{\bar{D}_i}{\rho} \frac{\partial \rho}{\partial x_k}, \quad (2.15)$$

and the species mixture averaged diffusion coefficients $(\bar{D}_1, \dots, \bar{D}_{n_s}) : \mathbb{R}^m \rightarrow \mathbb{R}^{n_s}$, from [41], are defined for the i -th species as

$$\bar{D}_i = \frac{p_{atm}}{p\bar{W}} \frac{\sum_{j=1, j \neq i}^{n_s} X_j W_j}{\sum_{j=1, j \neq i}^{n_s} X_j / D_{ij}}, \quad (2.16)$$

where $p_{atm} = 101325$ Pa, X_j is the mole fraction of species j , D_{ij} is the diffusion coefficient of species i to species j , and $\bar{W} : \mathbb{R}^m \rightarrow \mathbb{R}$ is the mixture molecular weight, defined as

$$\bar{W} = \rho / \sum_{i=1}^{n_s} C_i. \quad (2.17)$$

and the mole fractions $(X_1, \dots, X_{n_s}) : \mathbb{R}^{n_s} \rightarrow \mathbb{R}^{n_s}$ can be calculated directly from concentrations,

$$X_i = C_i / \sum_{i=1}^{n_s} C_i. \quad (2.18)$$

The Wilke model [42] is used to calculate viscosity

$$\mu = \sum_{i=1}^{n_s} \frac{X_i \mu_i}{X_i + \sum_{i=1, i \neq j}^{n_s} (X_j \phi_{ij})}, \quad (2.19)$$

where

$$\phi_{ij} = \frac{\left(1 + \left(\frac{W_j}{W_i}\right)^{1/4} \sqrt{\left(\frac{\mu_i}{\mu_j}\right)}\right)^2}{\sqrt{8 \left(1 + \frac{W_i}{W_j}\right)}},$$

and μ_i and μ_j are the species specific viscosities for species i and j , respectively. The Mathur model [43] is used to calculate conductivity,

$$\lambda = \frac{1}{2} \left(\sum_{i=1}^{n_s} X_i \lambda_i + \frac{1}{\sum_{i=1}^{n_s} \frac{X_i}{\lambda_i}} \right), \quad (2.20)$$

where λ_i is the conductivity of species i .

Finally, the source term, which includes the detailed chemical kinetics, is given by

$$\mathcal{S}(y) = (0, \dots, 0, 0, \omega_1, \dots, \omega_{n_s}), \quad (2.21)$$

where ω_i is the production rate of species i , which is the sum of the progress reaction rates from any arbitrary number of reactions and reaction types, cf. [44].

2.1. Additional thermodynamic relationships

It is often useful to extract from the aforementioned formulation a relationship where internal energy is linearly related to pressure at the current state, $\rho u = p/(\bar{\gamma} - 1)$. The relationship using $\bar{\gamma}$ can then be used to apply specific conditions, e.g., characteristic boundary conditions, see Appendix B, that were developed in the context of calorically perfect gases [45]. Here we present the steps to formulate $\bar{\gamma}$ and comment on where $\bar{\gamma}$ is equivalent to the ratio of specific heats

$$\gamma = \frac{c_p}{c_v} = \frac{c_p}{c_p - R}, \quad (2.22)$$

where c_p is the specific heat at constant pressure, c_v is the specific heat at constant volume, and R is the mixture gas constant

$$R = \frac{R^0 \sum_{i=1}^{n_s} C_i}{\rho}. \quad (2.23)$$

To find $\bar{\gamma}$ we use the definition of internal energy in terms of enthalpy and pressure,

$$\rho u = \rho h - p. \quad (2.24)$$

Here the enthalpy is

$$\rho h = \rho \sum_{i=1}^{n_s} Y_i \int_0^T c_{p,i} dT = \rho \sum_{i=1}^{n_s} Y_i h_i, \quad (2.25)$$

where

$$Y_i = W_i C_i / \rho, \quad (2.26)$$

is the mass fraction of species i , $c_{p,i}$ is the specific heat at constant pressure per unit mass of species i , and h_i is the species specific enthalpy polynomial of temperature that is degree n_p , $h_i = \sum_{k=0}^{n_p} a_{ik} T^k + R^0 T$. We reduce the definition of internal energy to achieve the equivalent formulation that contains the expression $\rho u = \frac{p}{\bar{\gamma} - 1}$ by introducing the mean value of c_p and $c_{p,i}$ from reference temperature, T_0 , to current temperature, T ,

$$\bar{c}_{p,i} = \frac{1}{T - T_0} \int_{T_0}^T c_{p,i} dT = \frac{h_i - h_i^0}{T - T_0} \quad (2.27)$$

and

$$\bar{c}_p = \sum_{i=1}^{n_s} \frac{Y_i}{T - T_0} \int_{T_0}^T c_{p,i} dT = \frac{\sum_{i=1}^{n_s} Y_i (h_i - h_i^0)}{T - T_0}, \quad (2.28)$$

where h_i^0 is the species specific enthalpy at T_0 . Using the following definitions

$$\bar{\gamma} = \frac{\bar{c}_p}{\bar{c}_p - R} = \frac{\sum_{i=1}^{n_s} \frac{Y_i (h_i - h_i^0)}{T - T_0}}{\sum_{i=1}^{n_s} \frac{Y_i (h_i - h_i^0)}{T - T_0} - R}, \quad (2.29)$$

$$\rho u = \frac{p}{\bar{\gamma} - 1} + \rho \sum_{i=1}^{n_s} Y_i (h_i^0 - \bar{c}_{p,i} T_0), \quad (2.30)$$

the inviscid total energy conservation without reactions becomes

$$\frac{\partial \left(\frac{p}{\bar{\gamma} - 1} + \frac{1}{2} \sum_{k=1}^d \rho v_k v_k \right)}{\partial t} + \nabla \cdot \left(\left(\frac{p}{\bar{\gamma} - 1} + \frac{1}{2} \sum_{k=1}^d \rho v_k v_k + p \right) (v_1, \dots, v_d) \right) = 0, \quad (2.31)$$

where the term $\rho \sum_{i=1}^{n_s} Y_i (h_i^0 - \bar{c}_{p,i} T_0)$ in Equation (2.30) is eliminated from Equation (2.31) by fixing T_0 to 0 K and multiplying the non-reacting inviscid form of the species conservation equations from Equation (3.6) by $W_i h_i^0$ and summing over all species conservation equations. Equation (2.31) is equivalent to the non-reacting inviscid form of the conservation of energy from Equation (2.1). Equation (2.31) has the same form of the compressible Euler equations, and therefore is convenient for evaluating characteristic boundary conditions and other functions that rely on a linear relationship between internal energy in pressure. However, those formulations may require the flow to be non-reacting with constant thermodynamic properties as $\bar{\gamma}$ is assumed to be constant in calorically perfect flows.

It is also important to note that $\bar{c}_{p,i}$, given by Equation (2.27), and \bar{c}_p , given by Equation (2.28), are not equivalent to the evaluations of $c_{p,i}$ and c_p from polynomial expressions, e.g., the analytic form of NASA's polynomial representations [40]. This is also true for γ , Equation (2.22), and $\bar{\gamma}$, Equation (2.29). Rather, $\bar{c}_{p,i}$ and \bar{c}_p can be viewed as the mean value of $c_{p,i}$ and c_p , where \bar{c}_p approaches c_p and $\bar{\gamma}$ approaches γ as $T - T_0 \rightarrow 0$. This difference can be shown mathematically by using the following polynomial definitions of specific heat at constant pressure,

$$c_{pi} = \sum_{k=0}^{n_p} b_{ik} T^k \quad (2.32)$$

and mixture averaged c_p ,

$$c_p = \sum_{i=1}^{n_s} Y_i \sum_{k=0}^{n_p} b_{ik} T^k. \quad (2.33)$$

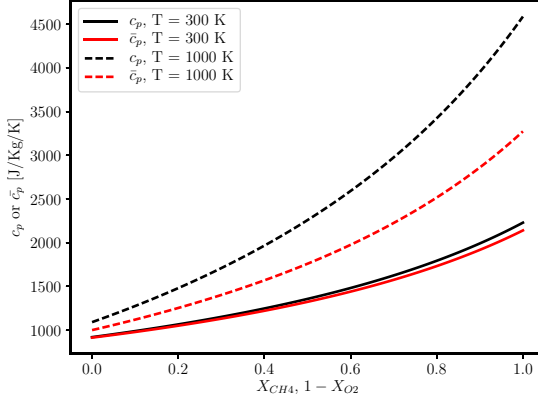
We arrive at the total enthalpy in polynomial form by integrating of Equations (2.32) and (2.33) from 0 to T and substituting the result into Equation (2.25),

$$\rho h = \rho \sum_{i=1}^{n_s} Y_i \left(\int_0^T c_{p,i} dT \right) = \rho \sum_{i=1}^{n_s} Y_i \left(\sum_{k=0}^{n_p} b_{ik} \frac{T^{k+1}}{k+1} \right). \quad (2.34)$$

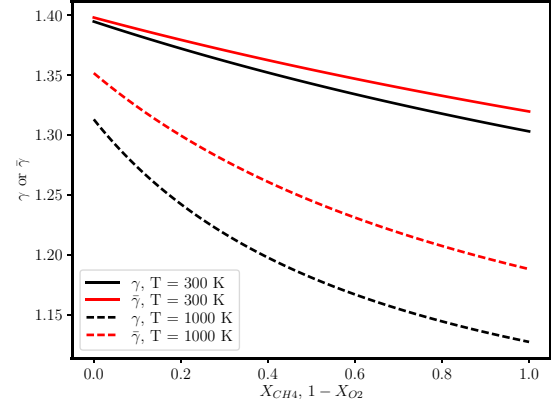
By substituting Equation (2.34) in Equation (2.28), we arrive at \bar{c}_p in terms of the $c_{p,i}$ polynomial coefficients and temperature,

$$\bar{c}_p = \frac{\sum_{i=1}^{n_s} Y_i \left(\sum_{k=0}^{n_p} b_{ik} \frac{T^{k+1}}{k+1} - \sum_{k=0}^{n_p} b_{ik} \frac{T_0^{k+1}}{k+1} \right)}{T - T_0}. \quad (2.35)$$

Therefore, \bar{c}_p and c_p as well as $\bar{\gamma}$ and γ are only equivalent if c_p is constant with respect to temperature, i.e., $n_p = 0$. Figure 2.1a shows the difference between c_p evaluated from NASA polynomials and \bar{c}_p evaluated from Equation (2.28). Additionally, Figure 2.1b shows the difference between γ evaluated from Equation (2.22) with c_p from Equation (2.33) and $\bar{\gamma}$ evaluated from Equation (2.29). The displayed values were calculated using a reference temperature, T_0 , of 200 K and mixture of methane, CH_4 , and oxygen, O_2 . The thermodynamic properties were evaluated at a temperature, T , of 300 K and 1000 K with the mixture varying from pure methane to pure oxygen, $X_{CH_4} = 1 - X_{O_2}$. The values for c_p and \bar{c}_p as well as γ and $\bar{\gamma}$ are significantly different at higher temperatures due to the large difference between the actual temperature and the reference temperature, $T - T_0$. This is indicative the care that must be taken when using formulations or relationships that rely on the ratio of specific heats with mixture varying thermodynamics properties.



(a) The difference between \bar{c}_p and c_p with reference temperature $T_0 = 200$ K, for a varying mixture of CH_4 and O_2 at two different temperatures, $T = 300$ K and $T = 1000$ K.



(b) The difference between $\bar{\gamma}$ and $\gamma = c_p/(c_p - R)$ with reference temperature $T_0 = 200$ K, for a varying mixture of CH_4 and O_2 at two different temperatures, $T = 300$ K and $T = 1000$ K.

Figure 2.1: The difference between c_p evaluated from NASA polynomials, Equation (2.33), and \bar{c}_p evaluated from Equation (2.28) and the difference between γ evaluated from NASA polynomials, Equation (2.22), and $\bar{\gamma}$ evaluated from Equation (2.29).

An additional source of confusion would be in the use of γ or $\bar{\gamma}$ in the evaluation of the speed of sound. The speed of sound is derived in the context of constant entropy and involves the ratio of the derivatives of internal energy and enthalpy, as outlined in Anderson [46]. Using the same steps outlined in Anderson for chemically reacting flows with variable thermodynamics, we came to the conclusion that the formulation presented here does not require any mean valued thermodynamics, such as \bar{c}_p , to evaluate the speed of sound. Therefore the mixture speed of sound is

$$c = \sqrt{\gamma RT}, \quad (2.36)$$

where γ is evaluated using c_p from Equation (2.33). In general, the formulation presented in this work does not rely on the speed of sound. However, we do make for the evaluation of both the numerical flux and characteristic boundary conditions.

3. Formulation

In this section we present DG discretizations for nonlinear conservation laws over a given d -dimensional domain $\Omega \subset \mathbb{R}^d$. In particular, we consider the multi-dimensional unsteady chemically reacting Navier-Stokes equations described in Section 2 and a one-dimensional system of ordinary differential equations (ODEs) in Section 3.2. We assume that Ω is partitioned by \mathcal{T} , consisting of disjoint sub-domains or cells κ , so that $\Omega = \cup_{\kappa \in \mathcal{T}} \bar{\kappa}$, with interfaces ϵ composing a set \mathcal{E} so that $\cup_{\epsilon \in \mathcal{E}} \epsilon = \cup_{\kappa \in \mathcal{T}} \partial\kappa$, over which an oriented normal $n : \epsilon \rightarrow \mathbb{R}^d$ is defined. Furthermore, we assume that \mathcal{E} consists of two disjoint subsets: the interior interfaces

$$\epsilon_{\mathcal{I}} \in \mathcal{E}_{\mathcal{I}} = \{\epsilon_{\mathcal{I}} \in \mathcal{E} \mid \epsilon_{\mathcal{I}} \cap \partial\Omega = \emptyset\} \quad (3.1)$$

and exterior interfaces

$$\epsilon_{\partial} \in \mathcal{E}_{\partial} = \{\epsilon_{\partial} \in \mathcal{E} \mid \epsilon_{\partial} \subset \partial\Omega\}, \quad (3.2)$$

so that $\mathcal{E} = \mathcal{E}_{\mathcal{I}} \cup \mathcal{E}_{\partial}$. For interior interfaces, $\epsilon_{\mathcal{I}} \in \mathcal{E}_{\mathcal{I}}$, there exists $\kappa^+, \kappa^- \in \mathcal{T}$ such that $\epsilon_{\mathcal{I}} = \partial\kappa^+ \cap \partial\kappa^-$ and n^+, n^- denote the outward facing normal of κ^+, κ^- respectively, so that $n^+ = -n^-$.

In order to discretize the nonlinear conservation laws considered in this work, we assume that there is a continuous, invertible mapping

$$u : \hat{\Omega} \rightarrow \Omega, \quad (3.3)$$

from a reference domain $\hat{\Omega} \subset \mathbb{R}^d$ to the physical domain $\Omega \subset \mathbb{R}^d$, see [47, 48, Section 2.4.1] for additional details. We introduce a discrete (finite-dimensional) subspace V_h^p over \mathcal{T} using standard piecewise polynomials, cf. [14]. Let \mathcal{P}_p denote the space of polynomials spanned by the monomials \mathbf{x}^α with multi-index $\alpha \in \mathbb{N}_0^d$, satisfying $\sum_{i=1}^d \alpha_i \leq p$. In the case of a simplicial grid,

$$V_h^p = \left\{ v \in [L^2(\Omega)]^m \mid \forall \kappa \in \mathcal{T}, v|_\kappa \circ u \in [\mathcal{P}_p]^m \right\}. \quad (3.4)$$

Let \mathcal{Q}_p denote the tensor-product space of polynomials spanned by the monomials \mathbf{x}^α with multi-index $\alpha \in \mathbb{N}_0^d$, satisfying $\alpha_i \leq p$ for $i = 1 \dots d$. In the case of a cuboid grid,

$$V_h^p = \left\{ v \in [L^2(\Omega)]^m \mid \forall \kappa \in \mathcal{T}, v|_\kappa \circ u \in [\mathcal{Q}_p]^m \right\}. \quad (3.5)$$

3.1. Discretization

We augment (2.1) with initial and boundary conditions as follows

$$\frac{\partial y}{\partial t} + \nabla \cdot \mathcal{F}(y, \nabla y) - \mathcal{S}(y) = 0 \text{ in } \kappa \quad \forall \kappa \in \mathcal{T}, \quad (3.6)$$

$$y(\cdot, t_0) - y_0 = 0 \text{ in } \kappa \quad \forall \kappa \in \mathcal{T}, \quad (3.7)$$

$$n \cdot \mathcal{F}(y, \nabla y) - n \cdot \mathcal{F}_\partial(y, \nabla y) = 0 \text{ on } \epsilon \quad \forall \epsilon \in \mathcal{E}_\partial, \quad (3.8)$$

$$G_\partial(y_\partial) : (y^+ - y_\partial) \otimes n = 0 \text{ on } \epsilon \quad \forall \epsilon \in \mathcal{E}_\partial, \quad (3.9)$$

where $G(y)$ is the partial linearization of the viscous, or diffusive, flux, \mathcal{F}^ν , with respect to gradient, ∇y , sometimes referred to as the homogeneity tensor [14]. The initial conditions are given by y_0 in Equation (3.7).

Following Hartmann and Leicht [14], the boundary conditions given by Equation (3.8) are imposed through the boundary flux, $\mathcal{F}_\partial(y, \nabla y) = \mathcal{F}_\partial^c(y) - \mathcal{F}_\partial^\nu(y, \nabla y)$, where $\mathcal{F}_\partial^c(y)$ and $\mathcal{F}_\partial^\nu(y, \nabla y)$ are the convective and viscous fluxes, respectively, at the boundary and boundary. The condition on the state at the boundary given by Equation (3.9) is imposed through the boundary state y_∂ and the boundary modified homogeneity tensor, $G_\partial(y_\partial)$.

The DG (semi-)discretization of Equations (3.6)- (3.8) is given as: find $\frac{\partial y}{\partial t} \in V_h^p$ such that

$$\begin{aligned} \sum_{\kappa \in \mathcal{T}} \left(\frac{\partial y}{\partial t}, v \right)_\kappa - \sum_{\kappa \in \mathcal{T}} (\mathcal{F}(y, \nabla y), \nabla v)_\kappa + \sum_{\epsilon \in \mathcal{E}} (h(y, n), \llbracket v \rrbracket)_\epsilon - \sum_{\epsilon \in \mathcal{E}} (\{\mathcal{F}^\nu(y, \nabla y)\} \cdot n - \delta(y, n), \llbracket v \rrbracket)_\epsilon \\ + \sum_{\kappa \in \mathcal{T}} ((\{y\} - y^+) \otimes n, (G^\top(y^+) : \nabla v))_{\partial \kappa} - \sum_{\kappa \in \mathcal{T}} (\mathcal{S}(y), v)_\kappa = 0 \quad \forall v \in V_h^p, \end{aligned} \quad (3.10)$$

where (\cdot, \cdot) denotes the inner product, $h(y, n)$ is the numerical flux, and $\delta(y, n)$ is a penalty term that is required for stability, $\llbracket \cdot \rrbracket$ denotes the jump operator, $\{\cdot\}$ denotes the average operator. In this work, the numerical flux chosen to be the HLLC approximate Riemann [49], see also Appendix B of [16]. The penalty term δ is implemented via the modified formulation of Bassi and Rebay [50, 51, 52], commonly known as BR2.

The DG space semi-discretization is integrated temporally with either a second or third order strong-stability-preserving Runge-Kutta method [53, 54], denoted SSP-RK2 and SSP-RK3 respectively. The time step is restricted by the Courant-Friedrichs-Lowy number, CFL, defined as

$$\text{CFL} = \frac{\Delta t}{(2p+1) \min(\Delta x)} (|v| + c), \quad (3.11)$$

where p is the polynomial degree. The optimal error estimates associated with the RK2+DG method are $\mathcal{O}(h^{p+1} + \tau^2)$ where h and τ are the length and time scales respectively [55]. This is verified for the

formulation presented in this manuscript in Section 4.4 where we study convergence under grid refinement for the advection of a thermal bubble for approximations corresponding to $p = 3, 4, 5$.

The discretization of the convection and diffusion operators is decoupled from the source term discretization via Strang operator splitting [56]. As such, we have developed an hp -adaptive finite element method for stiff ordinary differential equation (ODE) integration, which is described in Section 3.2, to facilitate integration of the system that arises from this type of splitting.

The discrete solution is given by the coefficients of a nodal basis defined over each element. In this work, the coefficients are defined at the corresponding Gauss-Lobatto points of the element. In this case, the trace of the solution is readily available, and does not require interpolation, therefore maintaining pressure equilibrium across element interfaces. The volume and surface terms of Equation (3.10) are numerically evaluated using a quadrature free approach [57, 58]. In the case of multi-component flows, the evaluation of the nonlinear flux presents unique challenges, the details of which are discussed in Section 3.1.1.

On interior interfaces, \mathcal{E}_I , the jump, average, numerical flux, and penalty term are defined in terms of the interior and exterior traces, as follows

$$[\![v]\!] = v^+ - v^- \text{ on } \epsilon \quad \forall \epsilon \in \mathcal{E}_I, \quad (3.12)$$

$$\{\!\{y\}\!\} = \frac{1}{2} (y^+ + y^-) \text{ on } \epsilon \quad \forall \epsilon \in \mathcal{E}_I, \quad (3.13)$$

$$\{\!\{\mathcal{F}^\nu(y, \nabla y)\}\!} = \frac{1}{2} (\mathcal{F}^\nu(y^+, \nabla y^+) + \mathcal{F}^\nu(y^-, \nabla y^-)) \text{ on } \epsilon \quad \forall \epsilon \in \mathcal{E}_I, \quad (3.14)$$

$$h(y, n) = h(y^+, y^-, n) \text{ on } \epsilon \quad \forall \epsilon \in \mathcal{E}_I, \quad (3.15)$$

$$\delta(y, n) = \delta(y^+, y^-, n) \text{ on } \epsilon \quad \forall \epsilon \in \mathcal{E}_I. \quad (3.16)$$

On the exterior interfaces, \mathcal{E}_∂ , we define the following,

$$[\![v]\!] = v^+ \text{ on } \epsilon \quad \forall \epsilon \in \mathcal{E}_\partial, \quad (3.17)$$

$$\{\!\{y\}\!\} = y_\partial(y^+, n^+) \text{ on } \epsilon \quad \forall \epsilon \in \mathcal{E}_\partial, \quad (3.18)$$

$$\{\!\{\mathcal{F}^\nu(y, \nabla y)\}\!} = \mathcal{F}_\partial^\nu(y_\partial(y^+, n^+), \nabla y^+) \text{ on } \epsilon \quad \forall \epsilon \in \mathcal{E}_\partial, \quad (3.19)$$

$$h(y, n) = h_\partial(y^+, n^+) \text{ on } \epsilon \quad \forall \epsilon \in \mathcal{E}_\partial, \quad (3.20)$$

$$\delta(y, n) = \delta_\partial(y^+, n^+) \text{ on } \epsilon \quad \forall \epsilon \in \mathcal{E}_\partial, \quad (3.21)$$

where $y_\partial(y^+, n^+)$ is the prescribed boundary state, $h_\partial(y^+, n^+)$ is the numerical boundary flux, and $\mathcal{F}_\partial^\nu(y_\partial(y^+), \nabla y^+, n^+)$ is the viscous boundary flux. The numerical and viscous fluxes are defined consistently with the imposed boundary condition such that (3.8) is satisfied, cf. [14].

In this work we apply the following boundary conditions, where k -th spatial component of the viscous boundary flux is denoted $\mathcal{F}_{\partial,k}^\nu(y_\partial(y^+), \nabla y^+)$, the boundary stress tensor, $\tau_\partial = \tau(y_\partial(y^+, n^+), \nabla y^+)$, and boundary heat flux, $q_\partial = q(y_\partial(y^+, n^+), \nabla y^+)$, are both evaluated at the boundary state and the interior gradient.

Inflow:

The inflow boundary condition is specified as

$$y_\partial(y^+, n^+) = y_\infty \text{ on } \epsilon \quad \forall \epsilon \in \mathcal{E}_{\text{in}}, \quad (3.22)$$

$$\mathcal{F}_{\partial,k}^\nu(y_\partial(y^+, n^+), \nabla y^+) = \mathcal{F}_k^\nu(y_\infty, \nabla y^+) \text{ on } \epsilon \quad \forall \epsilon \in \mathcal{E}_{\text{in}}, \quad (3.23)$$

$$h_\partial(y^+, n^+) = \mathcal{F}^c(y_\infty) \cdot n^+ \text{ on } \epsilon \quad \forall \epsilon \in \mathcal{E}_{\text{in}}, \quad (3.24)$$

$$\delta_\partial(y^+, n^+) = \delta(y^+, y_\infty) \text{ on } \epsilon \quad \forall \epsilon \in \mathcal{E}_{\text{in}}, \quad (3.25)$$

where $y_\infty : \Omega \rightarrow \mathbb{R}^m$ is a prescribed state.

Outflow:

We do not restrict the flow at an outflow boundary. The boundary condition is therefore given by

$$y_\partial(y^+, n^+) = y^+ \text{ on } \epsilon \quad \forall \epsilon \in \mathcal{E}_{\text{out}}, \quad (3.26)$$

$$\mathcal{F}_{\partial,k}^\nu(y_\partial(y^+, n^+), \nabla y^+) = \mathcal{F}_k^\nu(y^+, \nabla y^+) \text{ on } \epsilon \quad \forall \epsilon \in \mathcal{E}_{\text{out}}, \quad (3.27)$$

$$h_\partial(y^+, n^+) = \mathcal{F}^c(y^+) \cdot n^+ \text{ on } \epsilon \quad \forall \epsilon \in \mathcal{E}_{\text{out}}, \quad (3.28)$$

$$\delta_\partial(y^+, n^+) = 0 \text{ on } \epsilon \quad \forall \epsilon \in \mathcal{E}_{\text{out}}. \quad (3.29)$$

Here the penalty term is evaluated at the interior state, $\delta(y^+, y^+)$, which is trivially zero.

Slip wall:

At a slip wall we require the flow be parallel to the boundary. We therefore define the boundary velocity, $(v_{\partial,1}, \dots, v_{\partial,d}) : \mathbb{R}^m \times \mathbb{R}^d \rightarrow \mathbb{R}^d$ as

$$v_\partial(y^+, n^+) = \left(v_1^+ - \left(\sum_{k=1}^d v_k^+ n_k^+ \right) n_1^+ \right), \dots, \left(v_d^+ - \left(\sum_{k=1}^d v_k^+ n_k^+ \right) n_d^+ \right). \quad (3.30)$$

where the normal component has been set to zero. The boundary condition is specified as

$$y_\partial(y^+, n^+) = (\rho^+ v_{\partial,1}, \dots, \rho^+ v_{\partial,d}, (\rho e_t)^+, C_i^+, \dots, C_{n_s}^+) \text{ on } \epsilon \quad \forall \epsilon \in \mathcal{E}_{\text{slip}}, \quad (3.31)$$

$$\mathcal{F}_{\partial,k}^\nu(y_\partial(y^+, n^+), \nabla y^+) = (\tau_{\partial,1k}, \dots, \tau_{\partial,dk}, \sum_{j=1}^d \tau_{\partial,kj} v_j, 0, \dots, 0) \text{ on } \epsilon \quad \forall \epsilon \in \mathcal{E}_{\text{slip}}, \quad (3.32)$$

$$h_\partial(y^+, n^+) = h(y^+, 2y_\partial(y^+, n^+) - y^+, n^+) \text{ on } \epsilon \quad \forall \epsilon \in \mathcal{E}_{\text{slip}}, \quad (3.33)$$

$$\delta_\partial(y^+, n^+) = \delta(y^+, y_\partial(y^+, n^+)) \text{ on } \epsilon \quad \forall \epsilon \in \mathcal{E}_{\text{slip}}, \quad (3.34)$$

where we have also required the species diffusion velocities and thermal heat flux be zero. The viscous flux is computed from the boundary state and the interior gradient. Following Hartmann and Leicht [14], the numerical flux is evaluated at the interior state and the reflected state, $2y_\partial(y^+, n^+) - y^+$, which differs from the boundary state given by (3.31).

Adiabatic wall:

At an adiabatic wall, the flow moves at a specified wall velocity, while the species diffusion velocities and thermal heat flux are set to zero. The boundary condition is given as

$$y_\partial(y^+, n^+) = (\rho^+ v_{\partial,1}, \dots, \rho^+ v_{\partial,d}, (\rho e_t)^+, C_i^+, \dots, C_{n_s}^+) \text{ on } \epsilon \quad \forall \epsilon \in \mathcal{E}_{\text{adi}}, \quad (3.35)$$

$$\mathcal{F}_{\partial,k}^\nu(y_\partial(y^+, n^+), \nabla y^+) = (\tau_{\partial,1k}, \dots, \tau_{\partial,dk}, \sum_{j=1}^d \tau_{\partial,kj} v_j, 0, \dots, 0) \text{ on } \epsilon \quad \forall \epsilon \in \mathcal{E}_{\text{adi}}, \quad (3.36)$$

$$h_\partial(y^+, n^+) = \mathcal{F}^c(y_\partial(y^+, n^+)) \cdot n^+ \text{ on } \epsilon \quad \forall \epsilon \in \mathcal{E}_{\text{adi}}, \quad (3.37)$$

$$\delta_\partial(y^+, n^+) = \delta(y^+, y_\partial(y^+, n^+)) \text{ on } \epsilon \quad \forall \epsilon \in \mathcal{E}_{\text{adi}}, \quad (3.38)$$

where $(v_{\partial,1}, \dots, v_{\partial,d}) : \Omega \rightarrow \mathbb{R}^d$ is the prescribed boundary velocity.

Isothermal wall:

At an isothermal wall, the flow moves at a specified wall velocity and is actively heated, or cooled, to a specified temperature. Again, the species diffusion velocities are set to zero, but the thermal heat flux is unspecified. The boundary condition is given as

$$y_\partial(y^+, n^+) = \left(\rho_\partial v_{\partial,1}, \dots, \rho_\partial v_{\partial,d}, \rho u_\partial + 0.5 \cdot \sum_{j=1}^d \rho_\partial v_{\partial,k} v_{\partial,k}, C_{\partial,i}, \dots, C_{\partial,n_s} \right) \text{ on } \epsilon \quad \forall \epsilon \in \mathcal{E}_{\text{iso}}, \quad (3.39)$$

$$\mathcal{F}_{\partial,k}^\nu(y_\partial(y^+, n^+), \nabla y^+) = \left(\tau_{\partial,1k}, \dots, \tau_{\partial,dk}, \sum_{j=1}^d \tau_{\partial,kj} v_{\partial,j} - q_{\partial,k}, 0, \dots, 0 \right) \text{ on } \epsilon \quad \forall \epsilon \in \mathcal{E}_{\text{iso}}, \quad (3.40)$$

$$h_\partial(y^+, n^+) = \mathcal{F}^c(y_\partial(y^+, n^+)) \cdot n^+ \text{ on } \epsilon \quad \forall \epsilon \in \mathcal{E}_{\text{iso}}, \quad (3.41)$$

$$\delta_\partial(y^+, n^+) = \delta(y^+, y_\partial(y^+, n^+)) \text{ on } \epsilon \quad \forall \epsilon \in \mathcal{E}_{\text{iso}}, \quad (3.42)$$

where $(v_{\partial,1}, \dots, v_{\partial,d}) : \Omega \rightarrow \mathbb{R}^d$ is the prescribed boundary velocity, $T_\partial : \Omega \rightarrow \mathbb{R}$ is the prescribed boundary temperature, $(C_{\partial,i}, \dots, C_{\partial,n_s}) : \mathbb{R}^m \rightarrow \mathbb{R}^{n_s}$ are the boundary concentrations, where the i -th component is given as

$$C_{\partial,i}(y^+) = \frac{T^+}{T_\partial} C_i^+. \quad (3.43)$$

The boundary density is defined as

$$\rho_\partial = \sum_{i=1}^{n_s} W_i C_{\partial,i}, \quad (3.44)$$

and the boundary internal energy is given by

$$\rho u_\partial = \sum_{i=1}^{n_s} W_i C_{\partial,i} \sum_{k=0}^{n_p} a_{ik} T_\partial^k. \quad (3.45)$$

Characteristic:

The conserved state at characteristic boundaries is determined based on incoming and outgoing characteristics. The boundary condition is given as

$$y_\partial(y^+, n^+) = y^*(y^+, y_\infty, n^+) \text{ on } \epsilon \quad \forall \epsilon \in \mathcal{E}_{\text{cha}}, \quad (3.46)$$

$$\mathcal{F}_{\partial,k}^\nu(y_\partial(y^+, n^+), \nabla y^+) = \mathcal{F}_k^\nu(y_\partial(y^+, n^+), \nabla y^+) \text{ on } \epsilon \quad \forall \epsilon \in \mathcal{E}_{\text{cha}}, \quad (3.47)$$

$$h_\partial(y^+, n^+) = h(y^+, y_\partial(y^+, n^+), n^+) \text{ on } \epsilon \quad \forall \epsilon \in \mathcal{E}_{\text{cha}}, \quad (3.48)$$

$$\delta_\partial(y^+, n^+) = \delta(y^+, y_\partial(y^+, n^+)) \text{ on } \epsilon \quad \forall \epsilon \in \mathcal{E}_{\text{cha}}, \quad (3.49)$$

where $y^*(y^+, y_\infty, n^+)$ is the characteristic boundary value. The derivation $y^*(y^+, y_\infty, n^+)$ for non-reflecting inflow and outflow boundary conditions is given in Appendix B.

3.1.1. Nonlinear flux evaluation and consistent interpolation

In the case of single component flows, methods for computing the nodal basis coefficients corresponding to the flux⁰ include: interpolation, i.e., defining the high order basis coefficients corresponding to the solution, y , in terms of a linear combination of the low order basis function that are then used in the nonlinear flux evaluation, and L^2 projection, which requires the solution of an auxiliary problem but redistributes the error more evenly throughout the element, see [57, 58]. To analyze both approaches in the case of multi-component flows, we must consider the trial functions corresponding to the solution variables, i.e., the conserved state variables, which interpolate onto the span of $\{\varphi_1, \dots, \varphi_s\}$

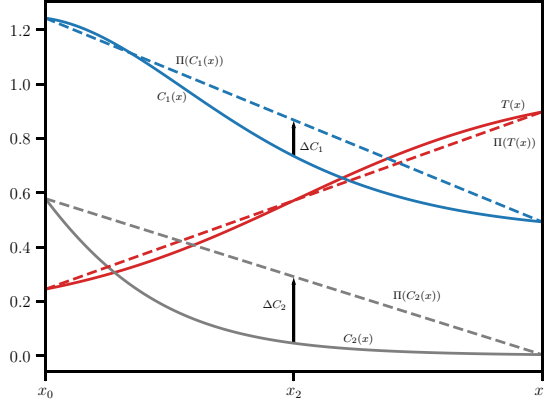
$$y_i = \sum_s y_i(x_s) \varphi_s, \quad (3.50)$$

⁰We restrict the discussion to the nonlinear convective flux, where the k -th spatial-component is given by (2.5), as we have found this term to be the most sensitive to the loss in pressure equilibrium, however, the viscous terms of (3.10) are also evaluated in this same manner.

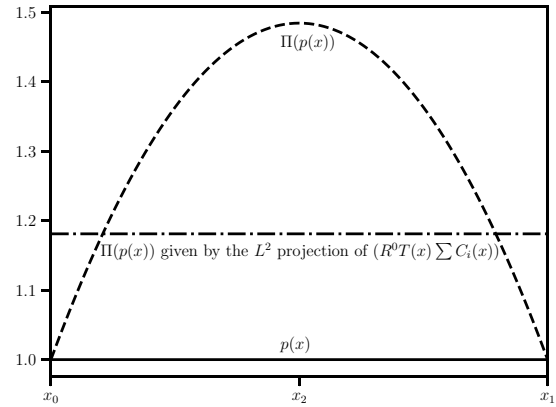
as well as the flux projection, which interpolates onto the span of $\{\varphi_1, \dots, \varphi_r\}$

$$(\Pi(\mathcal{F}(y)))_{ij} = \sum_r \mathcal{F}_{ij}(y(x_r)) \varphi_r, \quad (3.51)$$

where $r \geq s$.



(a) The normalized exact and discrete solutions corresponding to a piecewise linear approximation, i.e., $p = 1$, with basis coefficients defined at the points x_0 and x_1 . In this example, the error associated with the discrete approximation of the species concentrations results in a loss of pressure equilibrium when represented in a higher degree basis, e.g., $p = 2$, with basis coefficients defined at the points x_0, x_1 and x_2 . The difference between the exact and discrete values of the species concentrations are denoted ΔC_i for $i = 1, 2$. Equilibrium is maintained at the points corresponding to the original linear basis as there is no error associated with the discrete approximations in regards to pressure equilibrium.



(b) The exact pressure, $p(x)$, and the resulting discrete projection of the pressure, $\Pi(p(x))$, corresponding to a piecewise quadratic flux approximation, i.e., $p = 2$, defined in terms of both interpolation and the L^2 projection. Defining the basis coefficients via interpolation maintains pressure equilibrium between adjacent elements but it is lost within the element. In contrast, if the basis coefficients defined by the L^2 projection of $R^0 T(x) \sum_i C_i(x)$, pressure equilibrium is maintained within the element but lost between adjacent elements. Equilibrium is only maintained if the pressure is projected onto the same basis as the discrete solution.

Figure 3.1: The loss of pressure equilibrium for the higher degree basis coefficients corresponding to the nonlinear flux resulting from the error associated with the projection of the discrete solution. As a simplification, the analysis is given in terms of species concentrations and temperature, thereby avoiding the nonlinear relationship between the total energy, ρe_t , of the conserved state, y , and the pressure. However, the analysis would not change if we were to consider the more complicated case where temperature was not substituted for total energy.

At this point, the basis coefficients of the flux, \mathcal{F}_{ij} , can be directly evaluated in terms of the trial functions corresponding to the conserved state (3.50). For multi-component flows, this is only guaranteed to maintain pressure equilibrium for $r = s$, as the basis coefficients corresponding to the nodal values of pressure that are evaluated from the interpolated state, y , which is not constrained to remain in equilibrium as shown in Figure 3.1. This results in a loss of equilibrium within the element, while it is maintained between adjacent elements since the nodal values of the interpolated state correspond to the original space, define over s . However, the error associated with the loss of equilibrium is reduced as the discrete approximation is refined.

Alternatively, we can define an auxiliary problem and solve for the coefficients \mathcal{F}_{ij} via an L^2 projection. This approach redistributes the error throughout the element, in contrast to the approach based on interpolation of the trial space [57, 58]. In the case of multi-component flows, one might seek to minimize the error associated with the pressure projection for the evaluation of the flux coefficients. In this case, we must consider the temperature projection, which interpolates onto the span $\{\varphi_1, \dots, \varphi_m\}$

$$\Pi(T) = \sum_m T(y(x_m)) \varphi_m, \quad (3.52)$$

and species concentrations, which interpolate onto the span of $\{\varphi_1, \dots, \varphi_s\}$

$$C_i = \sum_s C_i(x_s) \varphi_s, \quad (3.53)$$

where $m \geq s$. The pressure, the projection of which is onto the span $\{\varphi_1, \dots, \varphi_r\}$

$$\Pi(p) = \sum_r p(y(x_r)) \varphi_r, \quad (3.54)$$

is defined via (2.6), and is given in terms of the sum of the concentrations, which is computed as

$$\sum_i C_i = \sum_i \sum_s C_i(x_s) \varphi_s \quad (3.55)$$

$$= \left(\sum_s C_1(x_s) \varphi_s + \dots + \sum_s C_{ns}(x_s) \varphi_s \right) \quad (3.56)$$

$$= (C_1(x_1) \varphi_1 + \dots + C_1(x_s) \varphi_s + \dots + C_{ns}(x_1) \varphi_1 + \dots + C_{ns}(x_s) \varphi_s) \quad (3.57)$$

$$= (C_1(x_1) \varphi_1 + \dots + C_{ns}(x_1) \varphi_1 + \dots + C_1(x_s) \varphi_s + \dots + C_{ns}(x_s) \varphi_s) \quad (3.58)$$

$$= ((C_1(x_1) + \dots + C_{ns}(x_1)) \varphi_1 + \dots + (C_1(x_s) + \dots + C_{ns}(x_s)) \varphi_s) \quad (3.59)$$

$$= \sum_s \left(\sum_i C_i(x_s) \right) \varphi_s \quad (3.60)$$

Furthermore, we introduce a scalar valued test function that interpolates onto the span of $\{\varphi_1, \dots, \varphi_q\}$

$$v = \sum_q v(x_q) \varphi_q. \quad (3.61)$$

Finally, the following linear system can be solved in order to determine the expansion coefficients of pressure, $p(y(x_r))$,

$$\left(\sum_r p(y(x_r)) \varphi_r, \sum_q v(x_q) \varphi_q \right)_\Omega = \left(R^o \sum_m T(y(x_m)) \varphi_m, \sum_s \left(\sum_i C_i(x_s) \varphi_s \right), \sum_q v(x_q) \varphi_q \right)_\Omega. \quad (3.62)$$

By factoring out the constants and rearranging the sums, we can write the resulting system as

$$\sum_q v(x_q) \left(\sum_r p(y(x_r)) (\varphi_r, \varphi_q)_\Omega \right) = \sum_q v(x_q) \left(R^o \sum_m T(y(x_m)) \sum_s \left(\sum_i C_i(x_s) \right) (\varphi_m, \varphi_q)_\Omega \right). \quad (3.63)$$

This approach is attractive because it will maintain equilibrium within an element. However, if the temperature or the species concentrations vary within the element, the value of pressure can be modified away from the equilibrium value as shown in Figure 3.1. As such, pressure equilibrium between adjacent elements will be lost and unphysical pressure oscillations will be generated.

Since both approaches described above result in the loss of equilibrium, either with an element or between adjacent elements, we must consider alternative approaches. In the case of multi-component flows, we have found the simplest approach to work best. We project the pressure such that equilibrium is maintained, i.e., into the same space as the conserved state, y . Therefore, the pressure projection interpolates onto the span $\{\varphi_1, \dots, \varphi_s\}$

$$\Pi(p) = \sum_s p(y(x_s)) \varphi_s. \quad (3.64)$$

Furthermore, the modified flux projection interpolates onto the span of $\{\varphi_1, \dots, \varphi_r\}$

$$(\Pi(\mathcal{F}(y)))_{ij} = \sum_r \mathcal{F}_{ij}(\tilde{y}(x_r)) \varphi_r, \quad (3.65)$$

where $r \geq s$, and it is now evaluated in terms of the modified state $\tilde{y} : \mathbb{R}^m \times \mathbb{R} \rightarrow \mathbb{R}^m$, which is defined as

$$\tilde{y}(y, p) = \left(\rho v_1, \dots, \rho v_d, \tilde{\rho} u + \frac{1}{2} \sum_{k=1}^d \rho v_k v_k, C_i, \dots, C_{n_s} \right). \quad (3.66)$$

The internal energy, $\tilde{\rho} u$, is given in terms of the pressure and the unmodified concentrations as

$$\tilde{\rho} u = \sum_{i=1}^{n_s} W_i C_i \sum_{k=0}^{n_p} a_{ik} \left(\frac{p}{R^o \sum_{i=1}^{n_s} C_i} \right)^k. \quad (3.67)$$

In this way, consistency between the volume and surface terms is preserved as well as pressure equilibrium both internally and between adjacent elements. A similar conclusion was reached in the context of reconstructed finite volume methods where it was found necessary to reconstruct the primitive variables, which include velocity and pressure, in order to maintain equilibrium at an isolated material or contact discontinuity [59, 60]. However, in the case of the formulation presented in this work, the above analysis applies to all regions of the flow, as the discussion was not restricted to the case of an isolated discontinuity, where equilibrium is trivially maintained since the primitive variables are readily available at the interface, see Section 4.

3.1.2. Artificial Viscosity

In order to stabilize the solution at physical discontinuities, we augment the nonlinear flux locally on each cell with a residual based artificial viscosity similar to [14], of the form

$$\mathcal{F}^{av}(y, \nabla y) = \left(S_{av}(p) + \left(C_{av} \tilde{h}_k^2 \left| \frac{\partial T}{\partial y} \cdot \frac{\mathcal{R}(y, \nabla y)}{T} \right| \right) \right) \nabla y, \quad (3.68)$$

here $\tilde{h}_k = h_k/(p+1)$ is evaluated using the characteristic length scale of the element, h_k , and the polynomial degree, p , of the element, $\mathcal{R}(y, \nabla y)$ is the strong form of the residual (3.6), $T' = \partial T / \partial y$ is the Jacobian of temperature with respect to the state variables, see Appendix A, C_{av} is a user defined coefficient, and S_{av} is a pressure dependent shock sensor. The exact form of the S_{av} used in this work is given by Ching et al. [61], which is based on the shock sensor originally described by Persson and Peraire [62].

3.2. DGODE: an hp -adaptive discontinuous Galerkin method for ordinary differential equation integration

We present an hp -adaptive discontinuous Galerkin method for the integration of potentially stiff ordinary differential equations, termed DGODE. Consider the case of a one-dimensional nonlinear ODE integration, given in strong form, defined for piecewise smooth, \mathbb{R}^m -valued, functions y , as

$$y' - \mathcal{S}(y) = 0 \text{ in } \kappa \quad \forall \kappa \in \mathcal{T}, \quad (3.69)$$

$$y(t_0) - y_0 = 0 \text{ on } \epsilon \quad \forall \epsilon \in \mathcal{E}_0, \quad (3.70)$$

where we have decomposed the exterior interfaces \mathcal{E}_∂ into disjoint subsets of inflow and outflow interfaces $\mathcal{E}_\partial = \mathcal{E}_0 \cup \mathcal{E}_f$ over which a boundary state, $y_\partial(y^+)$, which may be a function of the interior state y^+ , is defined. At the inflow interface $\epsilon_0 \in \mathcal{E}_0$ located at $t = t_0$, the inflow boundary condition (3.70) is applied, i.e., $y_\partial(y^+) = y_0$. No boundary condition is imposed at the outflow interface $\epsilon_f \in \mathcal{E}_f$ located at $t = t_f$, i.e., $y_\partial(y^+) = y^+$.

3.2.1. Weak formulation

Let V be vector-valued Sobolev space,

$$V = [H^1(\mathcal{T})]^m = \left\{ y \in [L^2(\Omega)]^m \mid \forall \kappa \in \mathcal{T}, y|_\kappa \in [H^1(\kappa)]^m \right\}, \quad (3.71)$$

defined over a mesh \mathcal{T} . The weak formulation is obtained by integrating the conservation law (3.69) against a test function and integrating by parts: find $y \in V$ such that

$$N(y, v) = \sum_{\epsilon \in \mathcal{E}} (h(y, n), \llbracket v \rrbracket)_{\mathcal{E}_{\epsilon}} - \sum_{\kappa \in \mathcal{T}} (y, \nabla v)_{\kappa} - \sum_{\kappa \in \mathcal{T}} (\mathcal{S}(y), v)_{\kappa} = 0 \quad \forall v \in V, \quad (3.72)$$

where $h(y, n)$ is the numerical flux function and the jump operator is defined by Equations (3.12) and (3.17) on interior and exterior interfaces respectively.

On interior interfaces the numerical flux is defined as the upwind numerical flux for linear advection based on the normal velocity $n \cdot v$,

$$h(y, n) = h(y^+, y^-, n) = \begin{cases} (n \cdot v) y^- & \text{if } n \cdot v < 0 \\ (n \cdot v) y^+ & \text{if } n \cdot v \geq 0 \end{cases}, \text{ on } \epsilon \quad \forall \epsilon \in \mathcal{E}_{\mathcal{I}}, \quad (3.73)$$

where the velocity is defined as $v = (1)$ and is constant throughout the domain.

On exterior interfaces the numerical flux is defined as

$$h(y, n) = h_{\partial}(y^+, n) = \begin{cases} (n \cdot v) y_{\partial}(y^+) & \text{if } n \cdot v < 0 \\ (n \cdot v) y^+ & \text{if } n \cdot v \geq 0 \end{cases}, \text{ on } \epsilon \quad \forall \epsilon \in \mathcal{E}_{\partial}. \quad (3.74)$$

where $y_{\partial}(y^+)$ is a prescribed boundary state, which may or may not depend on y^+ , the interior trace of y .

3.2.2. Discretization

In order to discretize Equation (3.72), we restrict V to a discrete (finite-dimensional) subspace V_h^p , as defined by Equation (3.4), so that the discretized weak formulation is: find $y \in V_h^p$ such that

$$N_h(y, v) = \sum_{\epsilon \in \mathcal{E}} (h(y, n), \llbracket v \rrbracket)_{\mathcal{E}} - \sum_{\kappa \in \mathcal{T}_h} (y, \nabla v)_{\kappa} - \sum_{\kappa \in \mathcal{T}_h} (\mathcal{S}(y), v)_{\kappa} = 0 \quad \forall v \in V_h^p. \quad (3.75)$$

Furthermore, let $n = \dim V_h^p$ and $(\varphi_1, \dots, \varphi_n)$ be a basis for V_h^p , then the discrete residual $(\mathcal{R}_1(y), \dots, \mathcal{R}_n(y)) \in \mathbb{R}^n$ is defined by

$$\mathcal{R}_i(y) = \sum_{\epsilon \in \mathcal{E}} (h(y, n), \llbracket \varphi_i \rrbracket)_{\mathcal{E}} - \sum_{\kappa \in \mathcal{T}} (\mathcal{F}(y), \nabla \varphi_i)_{\kappa} - \sum_{\kappa \in \mathcal{T}} (\mathcal{S}(y), \varphi_i)_{\kappa} \quad (3.76)$$

for $i = 1, \dots, n$.

We can therefore, write 3.75 as

$$\mathcal{R}(y) = 0, \quad (3.77)$$

and we can solve (3.77) iteratively via Newton's method: starting with an initial guess y^0 , we can solve for y^1, y^2, \dots by solving the linear system of equations

$$\mathcal{R}'[y^k](y^{k+1} - y^k) = -\mathcal{R}(y^k) \quad (3.78)$$

until a certain convergence criterion is satisfied and the application of the Jacobian of the discrete residual to a function $(\mathcal{R}'_1[y] \delta y, \dots, \mathcal{R}'_n[y] \delta y) \in \mathbb{R}^n$ is then given as

$$\mathcal{R}'_i[y] w = \sum_{\epsilon \in \mathcal{E}} (h_y(y, n) \delta y, \llbracket \varphi_i \rrbracket)_{\mathcal{E}} - \sum_{\kappa \in \mathcal{T}} (\delta y, \nabla \varphi_i)_{\kappa} - \sum_{\kappa \in \mathcal{T}} (\mathcal{S}'(y) \delta y, \varphi_i)_{\kappa} \quad (3.79)$$

where the $\mathcal{S}'(y) \delta y$ is the Jacobian of the chemical source term, the derivation of which is given in Appendix A.

The DG discretization converges optimally with order $O(h^{p+1})$ in the $L_2(\Omega)$ norm, i.e., $\|y - y_{\text{exact}}\|_{L_2(\Omega)}$, when no interior faces are present in the domain, but it converges sub-optimally with order $O(h^{p+1/2})$ in the $L_2(\Omega)$ norm due to the numerical flux at interior faces. Furthermore, since the discretization is adjoint consistent, we expect super-optimal convergence of the order $2p + 1$ for a functional output [14]. In the context of ODE integration, we are interested in the behavior of the error of the terminal condition, i.e., $|y(t_f) - y_{\text{exact}}(t_f)|$ and can therefore expect the error to exhibit $O(h^{2p+1})$ super-convergence [63, 14]. Finally, DGODE is stiffly A-stable for all polynomial degrees p [64, 63].

3.2.3. *hp*-adaptivity

We adaptively control both the time step, h , and the degree of the polynomial approximation, p , to ensure efficient integration of the nonlinear system and that the solution achieved is within a desired accuracy. The the norm of the local error estimate

$$\text{err}_h = \left\| \frac{\mathcal{R}_i(y)}{\epsilon_{\text{abs}} + \epsilon_{\text{rel}} |y_i|} \right\| \quad (3.80)$$

is used to define the nonlinear convergence criteria, which is given as

$$\text{err}_h < 1 \quad (3.81)$$

for $i = 1, \dots, n$, where $\epsilon_{\text{abs}} = 10^{-6}$ and $\epsilon_{\text{rel}} = 10^{-12}$ are user specified absolute and relative tolerances. If (3.81) is not satisfied within $n = 5$ iterations, the time step is reduced by a factor of ten. Otherwise, we estimate the accuracy of the solution and adapt the polynomial degree of the approximation accordingly.

In order to determine if adaptation of the polynomial degree is necessary, we apply a residual based a posteriori error estimation [14]. This approach has proved to be simple and robust. The the residual based error estimate is defined in terms of the interior cell residual and the interface residual:

$$\mathcal{R}_i^p(y) = \sum_{\kappa \in \mathcal{T}} (\nabla \cdot \mathcal{F}(y), \varphi_i)_\kappa - \sum_{\kappa \in \mathcal{T}} (\mathcal{S}(y), \varphi_i)_\kappa, \quad (3.82)$$

$$r_i^p(y) = \sum_{\epsilon \in \mathcal{E}_\partial} (h_\partial(y^+, n), \varphi_i^+)_{\mathcal{E}_\partial} + \sum_{\epsilon \in \mathcal{E}_\mathcal{T}} (h(y^+, y^-, n), [\varphi_i])_{\mathcal{E}_\mathcal{T}}. \quad (3.83)$$

In the case of the single-element, $\Omega = \kappa = (t_0, t_f)$, spectral discretization, Equation (3.83) reduces to

$$r_i^p(y) = ((y_0 - y^+), \varphi_i^+)_{\mathcal{E}_0}, \quad (3.84)$$

where the only interface contribution is due to the inflow boundary condition.

The norm of the local error estimate for p -refinement is

$$\text{err}_p = \|\mathcal{R}_i^p(y)\|_{L^2(\Omega)} + \|r_i^p(y)\|_{L^2(\Omega)}, \quad (3.85)$$

and the accuracy criteria is

$$\text{err}_p < \epsilon_p, \quad (3.86)$$

where $\epsilon_p = 10^{-6}$ is a user specified tolerance.

If the nonlinear solver converges, i.e. (3.81) is satisfied within $n = 5$ iterations, and (3.86) is satisfied, the solution is updated and a new time-step is determined using Gustafsson's method [65]. Otherwise, the polynomial degree of the approximation is refined until a user specified maximum polynomial degree is reached. Algorithm 1 summarizes the *hp*-adaptive DGODE method.

Algorithm 1 DGODE: hp -adaptive discontinuous Galerkin method for ordinary differential equation integration.

```

1: while  $t < t_f$  do
2:   Initialize the one-dimensional space-time solution  $y$  by extruding the initial condition  $y_0$ .
3:   for  $k = 1, \dots, n$  do
4:     Solve  $\mathcal{R}'[y^k] \delta y = -\mathcal{R}(y^k)$  for  $\delta y$ .
5:     Increment the solution  $y^{k+1} += \delta y$ .
6:     if  $\left\| \frac{\mathcal{R}(y^k)}{\epsilon_{\text{abs}} + \epsilon_{\text{rel}} |y^k|} \right\| < 1$  then
7:       Converged return;
8:     end if
9:   end for
10:  if converged then
11:    if  $(\|(\nabla y - S(y), v)_\kappa\| < \epsilon_p)$  or  $(p == p_{\text{max}})$  then
12:      Restrict the space-time solution  $y_0 = y(t + \delta t)$ .
13:      increment  $t += \delta t$ .
14:      Compute a new time step  $\delta t$ .
15:    else
16:       $p$ -refine the space-time solution  $y$  and goto 3.
17:    end if
18:  else
19:    reduce the time step  $\delta t$ .
20:  end if
21: end while

```

3.2.4. Convergence of the ordinary differential equation integration under hp -refinement

We apply the DGODE discretization to Equation (3.69) and study convergence under hp -refinement. In this case, we consider the initial value problem defined for the piecewise smooth, \mathbb{R}^1 -valued, function y as

$$y' - \lambda y = 0 \text{ in } (0, 1), \quad (3.87)$$

$$y(0) - 1 = 0 \text{ on } 0, \quad (3.88)$$

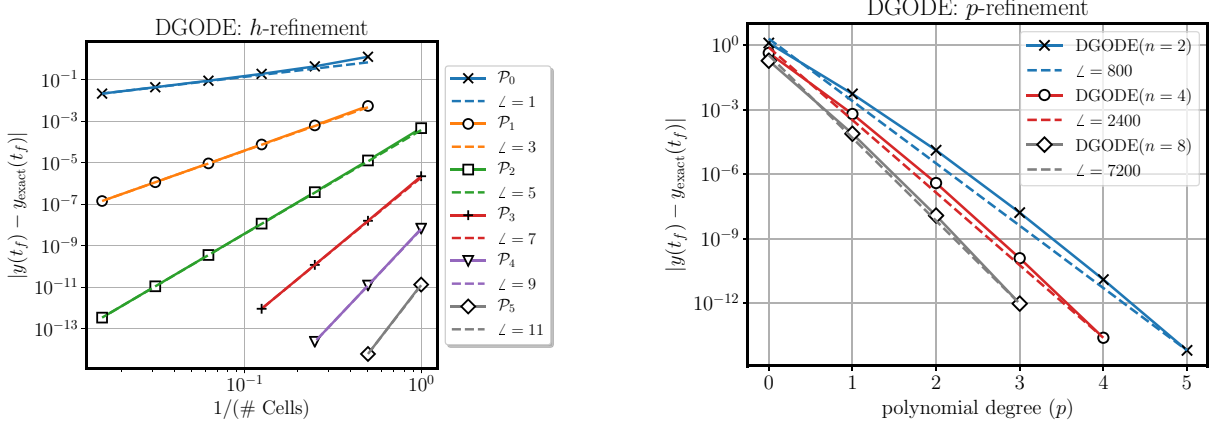
where $\lambda = -1$.

The exact solution is given as

$$y(t) = \exp(\lambda t). \quad (3.89)$$

Since the DG discretization is adjoint consistent, we expect super-optimal convergence of the order $2p+1$ for a functional output. In the context of ODE integration, the functional output we are most concerned with is the L_∞ error of the solution at the final time, i.e., the terminal condition: $|y(t_f) - y_{\text{exact}}(t_f)|$. Figure 3.2 presents convergence plots for the terminal condition corresponding to the exact solution with respect to both grid, h , and polynomial, p , refinement. Figure 3.2a presents the convergence of the terminal condition under grid refinement for polynomial degrees $p = 0, \dots, 5$. The coarsest grid consisted of one linear line cell and the finest grid consisted of 64 linear line cells. The DGODE discretization converges at the expected super-optimal rate of $2p+1$.

Polynomial refinement is also an effective strategy for increasing the accuracy of the approximation. Figure 3.2b presents the convergence of the terminal condition under polynomial refinement for grids consisting of 2, 4, and 8 linear line cells. For each grid resolution, the error associated with the terminal condition decreases exponentially.



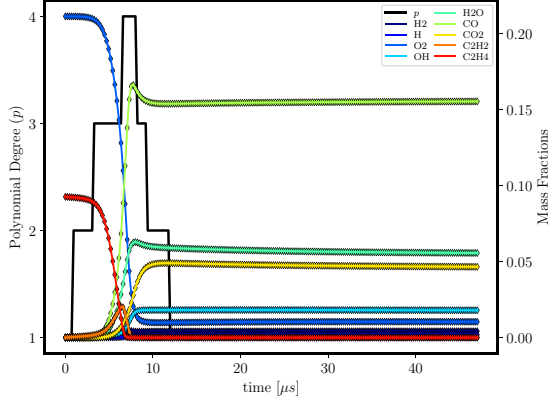
(a) Convergence with respect to grid (h) refinement. The coarsest grid consisted of one linear line cell and the finest grid consisted of 64 linear line cells. The DGODE discretization converges with the expected super-optimal ($2p + 1$) order for a functional output.

(b) Convergence with respect to polynomial (p) refinement for grids consisting of 2, 4, and 8 linear line cells.

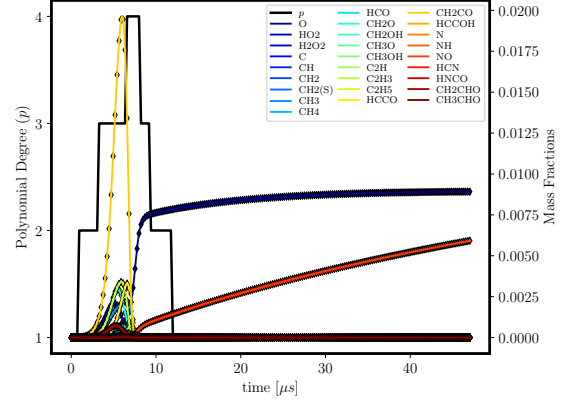
Figure 3.2: Convergence plots for the terminal condition, $|y(t_f) - y_{\text{exact}}(t_f)|$, with respect to both grid (h) and polynomial (p) refinement. The exact solution at $t_f = 1$, given by Equation (3.89), is $\exp(-1)$.

3.2.5. Ordinary differential equation integration of a homogeneous reactor

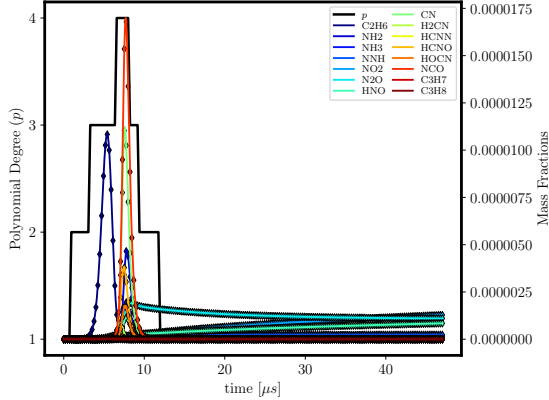
We solve the one-dimensional system of ODEs corresponding to a homogeneous reactor with detailed kinetics using the GRI-3.0 mechanism [17] to demonstrate the ability of DGODE to employ hp -adaptivity to ensure accurate and efficient integration of the stiff chemical system. The mechanism consists of 53 species and 325 reactions. We initialized the solution with an equivalence ratio of one, $\phi = 1$, for ethylene-air and an initial pressure, $p_0 = 1 \text{ atm}$, and an initial temperature, $T_0 = 2000 \text{ K}$. Figures 3.3a-3.3d show the results of the species mass fractions and temperature as a function of time as well as the adapted polynomial degree compared to results using Cantera [66]. The adapted polynomial degree is the greatest in the region of highest chemical activity. Almost all species are created and destroyed in regions where $p > 1$. As time progresses, all species reach an equilibrium with the exception of NO , which is slowly created in regions of hot products.



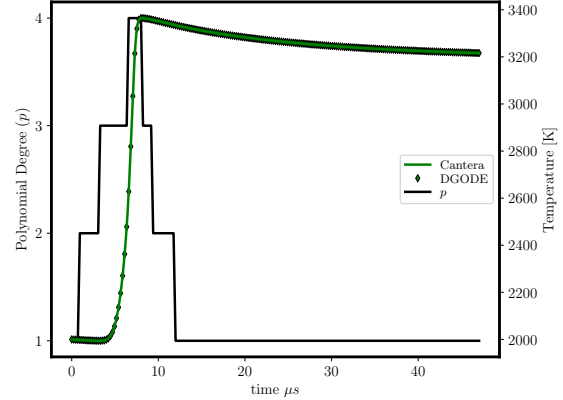
(a) The mass fractions of species with peak value $2 \times 10^{-2} < Y_i < 2$ and adapted polynomial degree, p (solid black line), computed with DGODE for the homogeneous reactor corresponding to the GRI-3.0 mechanism (\diamond) compared with the mass fractions computed using Cantera (solid colored lines).



(b) The mass fractions of species $2 \times 10^{-5} < Y_i < 2 \times 10^{-2}$ and adapted polynomial degree, p (solid black line), computed with DGODE for the homogeneous reactor corresponding to the GRI-3.0 mechanism (\diamond) compared with the mass fractions computed using Cantera (solid colored lines).



(c) The mass fractions of species $Y_i < 2 \times 10^{-5}$ and adapted polynomial degree, p (solid black line), computed with DGODE for the homogeneous reactor corresponding to the GRI-3.0 mechanism (\diamond) compared with the mass fractions computed using Cantera (solid colored lines).



(d) The temperature (\diamond) and adapted polynomial degree, p (solid black line), computed with DGODE for the homogeneous reactor corresponding to the GRI-3.0 mechanism compared with the temperature profile computed using Cantera (solid green line).

Figure 3.3: The DGODE solution for mass fractions, temperature, and adapted polynomial degree for homogeneous reactor corresponding to the GRI-3.0 mechanism. DGODE automatically adapts the polynomial degree to accurately resolve the disparate time-scales associated with the various species

The stiffness associated with the analytical Jacobian of the chemical source term is defined as the ratio of the absolute value of the the real part of the largest and smallest eigenvalues,

$$\frac{|Re(\lambda_{\max})|}{|Re(\lambda_{\min})|}, \quad (3.90)$$

where λ_{\max} and λ_{\min} are the largest and smallest eigenvalues respectively of the source term Jacobian, \mathcal{S}' , see Appendix A. Figure 3.4 shows the stiffness from Equation (3.90) as a function of time for the aforementioned homogeneous reactor as well as the adapted polynomial degree, p . The adapted polynomial degree is at a maximum in regions where the stiffness is greatest, indicating that DGODE is efficiently integrating the source term using high-order approximations when necessary.

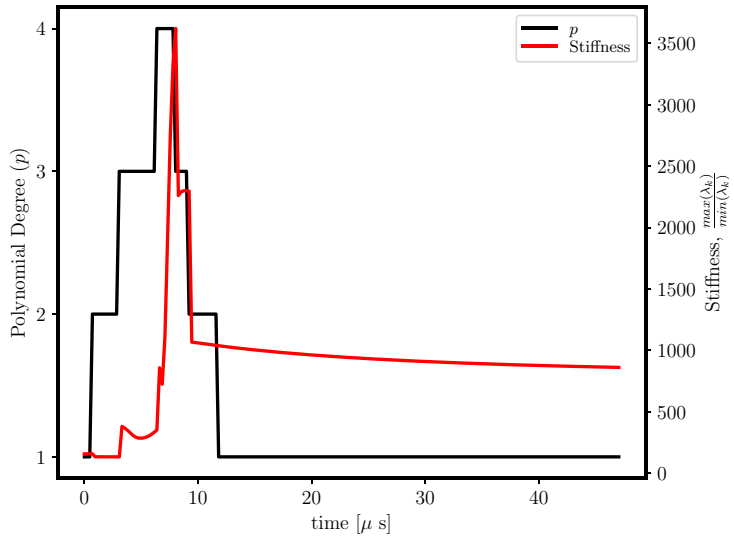
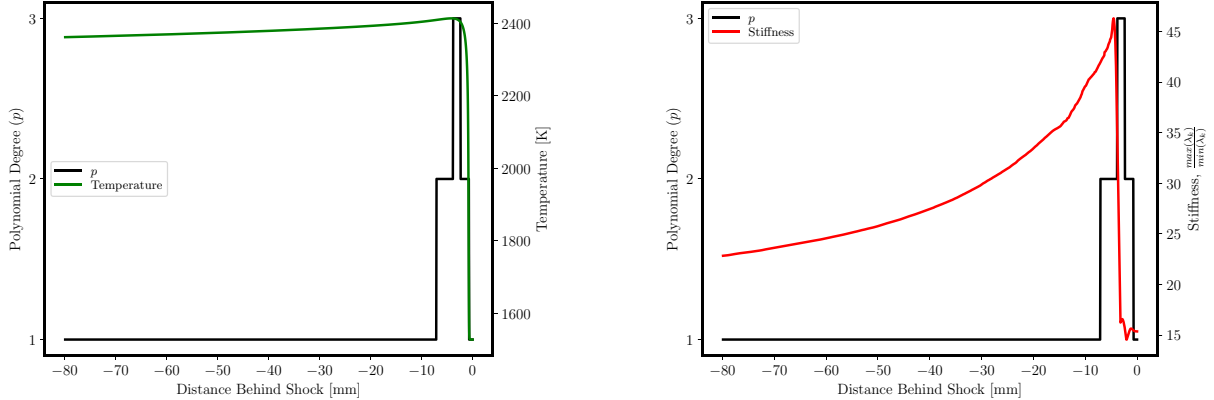


Figure 3.4: Stiffness ratio of the analytical Jacobian for the chemical source term corresponding to the GRI-3.0 mechanism compared to the adapted polynomial degree computed using DGODE for the homogeneous reactor. DGODE automatically adapts the polynomial degree to accurately integrate the potentially stiff chemical source term. High-order integration is only used in the stiffest regions.

We test the effectiveness of local polynomial adaptivity in the case of a temporally evolving and spatially varying problem with stiff chemistry by analyzing a one dimensional detonation wave propagating through a premixed medium of ethylene-air at equivalence ratio of one, $\phi = 1$. The mixture ahead of the detonation is at a pressure of $p = 101325$ Pa and a temperature of $T = 300$ K. The detonation wave is moving from left to right. To the left of the shock, a region of high temperature and pressure causes the mixture to react and sustain the detonation. In a stable scenario, this detonation velocity is steady in time, and the structures can be numerically predicted. For this example, the profiles for species and the thermodynamic state in the reacting region to left of the shock were obtained via the Shock and Detonation Toolbox [67]. Figures 3.5a and 3.5b show the temperature and the stiffness as well as the adapted polynomial degree for a time step of $\Delta t = 10^{-8}$ s using DGODE. As expected, the polynomial degree of the approximation adapts to the stiffness of the chemical system, which sharply increases to the left of the detonation front, where heat release is the greatest, and decays as the distance from the detonation front increases.

The local adaptation of the polynomial order is also demonstrated for time dependent results in combination with our method for simulating multi-component fluid dynamics corresponding to hydrogen detonations in Sections 5.3 and 5.4. Finally, the polynomial degree of the local ODE approximation can be used to accurately, and unambiguously, identify regions of stiff chemical reactions. This is potentially a useful indicator for load balancing across multiple processors, cf. [30, 68].



(a) The temperature profile compared to the polynomial degree of the ODE integration for the one-dimensional C_2H_4 and air detonation wave.

(b) Stiffness associated with the analytical Jacobian of the chemical source term corresponding to the GRI-3.0 mechanism compared to the polynomial degree of the ODE integration.

Figure 3.5: The temperature profile and stiffness, measured as the ratio of the largest and smallest eigenvalue of the chemical source term Jacobian corresponding to the GRI-3.0 mechanism compared to the polynomial degree of the ODE integration for the one-dimensional C_2H_4 and air detonation wave. DGODE automatically adapts the polynomial degree to accurately integrate the potentially stiff chemical source term. High-order integration is only used in the stiffest regions in space.

4. Discrete pressure equilibrium at material interfaces

Various methods have been used to suppress unwanted pressure oscillations in smooth regions of multi-component flows [25, 26, 15, 27, 16]. Jenny et al. summarized the conditions where pressure oscillations do not exist in [21], which were restated in the Section 1.1 of this work. Their conclusions also apply to the formulation presented in this work, as detailed in Appendix C. Therefore, we do not expect the conservative DG formulation to generate pressure oscillations via numerical mixing of species concentrations at the same temperature. Discontinuities in temperature will generate pressure oscillations if the species internal energies are nonlinear with respect to temperature. However, the magnitude of these oscillations is reduced as the solution is better resolved and the oscillations do not cause the numerical simulation to fail. In this section we study several test cases in order to verify the results of Appendix C, which were derived in the context of simplified numerics.

To study the generation of unphysical pressure oscillations for the formulation presented in Section 3, we test three different methods for evaluating the thermodynamic quantities required to evaluate the convective and numerical fluxes. These methods are listed in Table 1, where basic steps for evolving the state temporally are listed. The first column corresponds to the formulation with the exact thermodynamics considered in this work and the second column corresponds to a formulation with frozen thermodynamics where $\bar{\gamma}$ and \bar{c}_p are held constant throughout each time step. The formulation with exact thermodynamics does not evaluate \bar{c}_p in order to calculate the convective flux, or numerical flux, however the speed of sound (2.36) is required for the evaluation of the numerical flux. Instead the nonlinear equation (2.9) for temperature is solved and pressure is then calculated via (2.6). For the formulation with frozen thermodynamics, we consider two methods for evaluating the specific heat at constant pressure: the mean value \bar{c}_p given by (2.28) and directly evaluating c_p given by (2.33) based on the NASA polynomials expressions.

Table 1: Procedure for temporally evolving the state.

Step	Formulation with Exact Thermodynamics	Formulation with Frozen Thermodynamics
1	Calculate pressure from (2.6) using the temperature obtained by solving (2.7).	Calculate pressure from (2.31) based on frozen $\bar{\gamma}$.
2	Update state using $h_{HLLC}(y^+, y^-, n)$ and $\mathcal{F}_k^c(y)$.	Update state using $h_{HLLC}(y^+, y^-, n)$ and $\mathcal{F}_k^c(y)$.
3		Calculate and freeze the new \bar{c}_p from (2.28) using the updated state and temperature, which is calculated from (2.6) where the pressure is calculated via (2.31) using the frozen $\bar{\gamma}$. Calculate and freeze the new \bar{c}_p as equivalent to c_p from (2.33) using the updated state and temperature, which is calculated from (2.6) where the pressure is calculated via (2.31) using the frozen $\bar{\gamma}$.
4		Calculate and freeze new $\bar{\gamma}$ from \bar{c}_p in Step 3 and R from the updated state.

If $\bar{\gamma}$ is frozen as presented in the second column of Table 1, then pressure oscillations will occur as derived in [19, 20]. This is problematic for smooth regions of reacting multi-component flows, as it requires additional methods for suppressing the unphysical pressure oscillations, even in regions of the flow where temperature is continuous. Although, we do not make use of it otherwise, the formulation with frozen thermodynamics is considered in this section to demonstrate that it is potential source of unphysical pressure oscillations.

In Sections 4.1-4.3 we consider the advection of material discontinuities for different species and temperature profiles where the concentrations are comprised of two fictitious species for reproducibility purposes. The initial conditions all have the form

$$(v, T, p, Y_1, Y_2) = \begin{cases} (10 \text{ m/s}, T, 1 \text{ atm}, 0, 1) & \text{if } 0.025 < x < 0.075 \\ (10 \text{ m/s}, T, 1 \text{ atm}, 1, 0) & \text{otherwise} \end{cases}, \quad (4.1)$$

where T is problem specific.

In Section 4.4 we revisit the case of a slowly moving one dimensional hydrogen and oxygen thermal bubble previously considered by [16] where it was reported that conservative schemes would generate unphysical pressure oscillations. For the cases considered in this section, numerical instabilities are not suppressed via artificial viscosity, limiting, or filtering in order to emphasize the effect of numerical mixing on pressure in the absence of any additional stabilization.

4.1. Species discontinuities at constant temperature

In this Section, and Sections 4.2 and 4.3 as well, we approximate exact solutions corresponding to material interfaces by solving the non-reacting, inviscid formulation of Equations (3.6)-(3.8) using $DG(p = 1)$, $DG(p = 2)$, and $DG(p = 3)$, without artificial viscosity or limiting. For ease of reproducibility, we constructed two fictitious species, $n_s = 2$, with different molecular weights, $W_1 = 20$ and $W_2 = 70$. Here we used a nonlinear function for internal energy, with $n_p = 3$, $a_{1k} = \{0, 2.08 \times 10^4, 83.1, -2.77 \times 10^{-2}\}$ and $a_{2k} = \{0, 3.33 \times 10^4, 83.1, -2.22 \times 10^{-2}\}$, of the form $u_i = \sum_{k=0}^{n_p} a_{ik} T^k$ where u_i is the units J/kg with temperature, T , in K. The enthalpy of each species is therefore $h_i = \sum_{k=0}^{n_p} a_{ik} T^k + R^0 T$ and the specific heat at constant pressure of each species is $c_{p,i} = \sum_{k=0}^{n_p} k a_{ik} T^{k-1} + R^0$. For each test case the domain is 0.1 m,

with grid spacing of $h = 0.002$ m. All reported results are using the formulation with exact thermodynamics unless otherwise specified.

In this first test case, we consider a species discontinuity at a constant temperature, $T = 300$ K, given by (4.1). The test problem is run on a periodic domain for one full cycle with $CFL = 0.1$. Figures 4.1a, 4.1b, and 4.1c show the species mass fractions for the $DG(p = 1)$, $DG(p = 2)$, and $DG(p = 3)$ solutions. All three solutions present numerical overshoots and mixing of the species mass fractions across the discontinuities. Some of these numerical instabilities cause the mass fractions to be greater than one or less than zero, and, as expected, the higher order solutions are more oscillatory for the species mass fractions. In practical simulations, these instabilities would be suppressed via limiting or artificial viscosity, however these approaches would also suppress pressure oscillations, the generation of which these test cases were created to study.

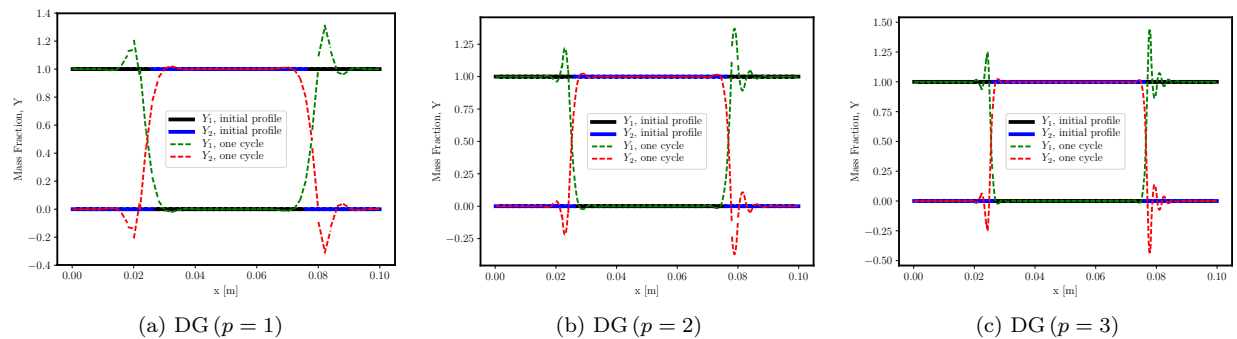


Figure 4.1: The mass fractions profiles of the DG solutions for $p = 1, 2, 3$ corresponding to the species discontinuity (4.1) at a constant temperature, $T = 300$ K, test case after one cycle through the domain where the thermodynamics were evaluated exactly. The formulation behaves exactly like its single-component counterpart, discontinuous interfaces generate numerical instabilities that need to be suppressed in practical simulations with artificial viscosity, as in Section 5.2, or physical diffusion as in Section 5.6, but they do not lead to unphysical pressure oscillations, as shown in Figure 4.2, when the thermodynamics are evaluated exactly.

Figure 4.2 shows the pressure after one cycle for the formulation with exact thermodynamics and for the formulation using frozen \bar{c}_p and frozen c_p . The frozen c_p solution has pressure oscillations that are on the order of one percent error. Small perturbations of pressure caused by freezing \bar{c}_p are shown in Figure 4.2b. The error caused by the frozen \bar{c}_p formulation is reduced as the approximation order is increased from $DG(p = 1)$ to $DG(p = 3)$. In contrast, the pressure for each solution using the exact thermodynamics maintains a flat profile despite numerical instabilities generated at the discontinuous interface and the error never exceeds 10^{-7} atm, which is consistent with the analysis in Appendix C and [21].

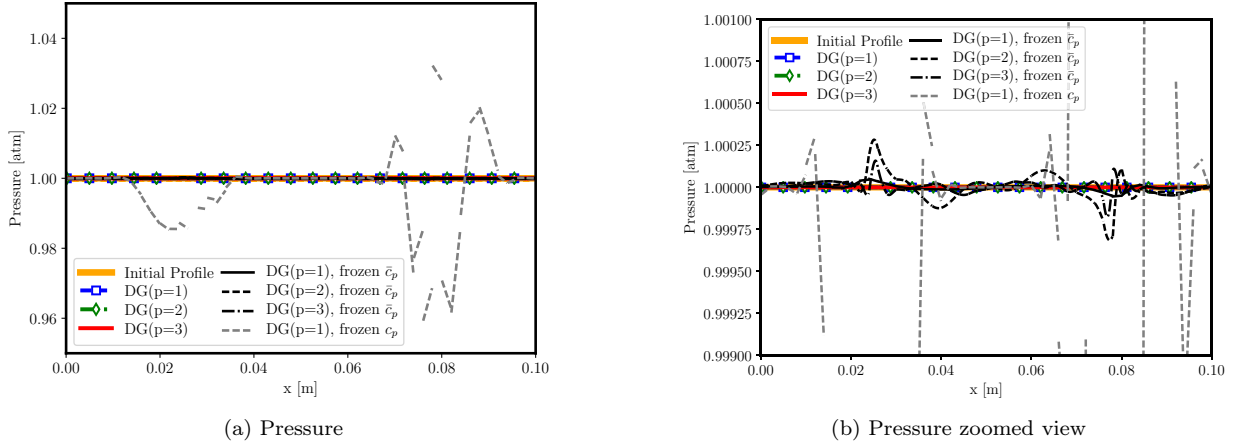
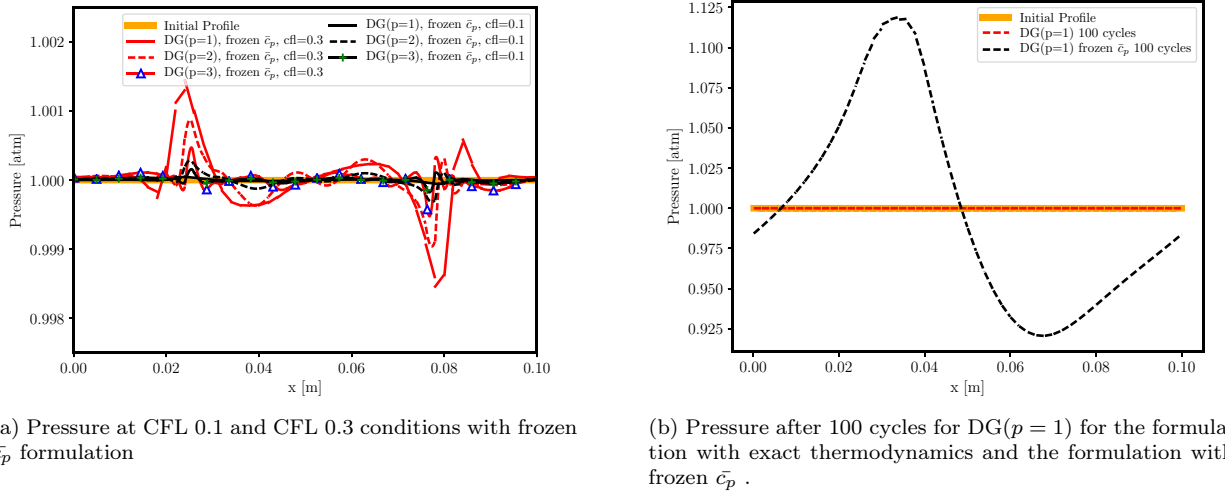


Figure 4.2: The pressure profiles corresponding to the $DG(p = 1)$, $DG(p = 2)$, and $DG(p = 3)$ solutions after one cycle for species discontinuity (4.1) at a constant temperature, $T = 300$ K, test case. The formulation behaves exactly like its single-component counterpart, discontinuous interfaces generate numerical instabilities, as shown in Figure 4.1, that need to be suppressed in practical simulations with artificial viscosity, as in Section 5.2, or physical diffusion as in Section 5.6, but they do not lead to unphysical pressure oscillations when the thermodynamics are evaluated exactly, as shown above.

Figure 4.3a shows the solutions for $DG(p = 1)$, $DG(p = 2)$, and $DG(p = 3)$ for the formulation with frozen \bar{c}_p at CFL of 0.1 and 0.3. The larger time steps exacerbate the instability introduced by freezing \bar{c}_p to exceed 0.001 atm, which is still an order of magnitude less than the error of the frozen c_p solutions. The solutions for the formulation with exact thermodynamics is unaffected by the time step and therefore the corresponding results are not shown.

Additionally, Figure 4.3b shows the pressure profile from the $DG(p = 1)$ solution for the formulation with frozen \bar{c}_p and the formulation with exact thermodynamics after 100 cycles, i.e., $t = 1$ s. The pressure oscillations for the 100 cycle solution using the formulation with frozen \bar{c}_p grow in time to be on the order of the one cycle with frozen c_p . The pressure solution for the formulation with exact thermodynamics remains constant after 100 cycles.

For brevity, the temperature solutions are not presented. The formulation with frozen c_p temperature solution fluctuated on the order of 1 K whereas the formulation with frozen \bar{c}_p solution fluctuates less than 0.025 K. These fluctuations were located at the species interfaces. The temperature solution corresponding to the formulation using exact thermodynamics remains flat and does not deviate by more than 10^{-4} K from the exact value of 300 K.



(a) Pressure at CFL 0.1 and CFL 0.3 conditions with frozen \bar{c}_p formulation

(b) Pressure after 100 cycles for DG($p = 1$) for the formulation with exact thermodynamics and the formulation with frozen \bar{c}_p .

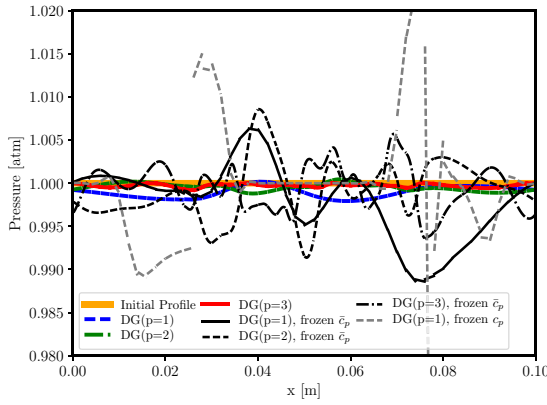
Figure 4.3: Pressure for DG($p = 1$), DG($p = 2$), and DG($p = 3$) solutions for the advection of a species discontinuity (4.1) at a constant temperature, $T = 300$ K, after one cycle using CFL of 0.1 and CFL of 0.3 with frozen \bar{c}_p and pressure after 100 cycles using the formulation with exact thermodynamics and the formulation with frozen \bar{c}_p for DG($p = 1$). The solutions were computed without additional stabilization, e.g., artificial viscosity, limiting, or filtering, in order to emphasize the effect of the thermodynamic formulation on the generation of unphysical pressure oscillations.

4.2. Species discontinuities with temperature discontinuities

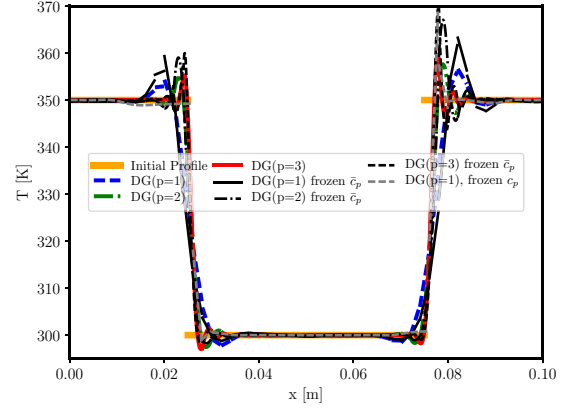
We consider the same discontinuous profile as in Section 4.1 and introduce a temperature discontinuity defined as

$$T = \begin{cases} 300 \text{ K} & \text{if } 0.025 < x < 0.075 \\ 350 \text{ K} & \text{otherwise} \end{cases}. \quad (4.2)$$

Similar to the previous test case, the three solutions present numerical overshoots and mixing of the species mass fractions across the discontinuities but are not shown graphically for brevity. Figures 4.4a and 4.4b show the pressure and temperature, respectively, after one cycle for the formulation using exact and frozen thermodynamics. The formulation with frozen c_p fails before one complete cycle and is shown after 100 time steps as a dashed grey line. The pressure for the solutions using the formulation with exact thermodynamics causes pressure oscillations that are an order of magnitude less than the frozen \bar{c}_p simulations. The oscillations in the formulation with exact thermodynamics are due to the numerical mixing of species across a temperature discontinuity and are expected based on the discussion in Appendix C and [21]. Both the formulation with exact thermodynamics and formulation with frozen \bar{c}_p produce overshoots and undershoots at the temperature discontinuities. The temperature oscillations associated with the formulation using frozen \bar{c}_p are larger than the oscillations corresponding the formulation with exact thermodynamics.



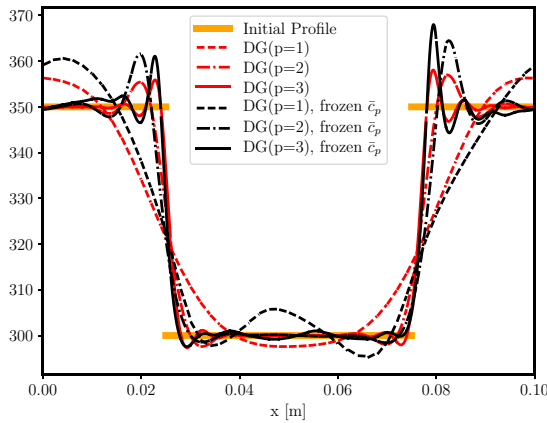
(a) Pressure solutions after one cycle.



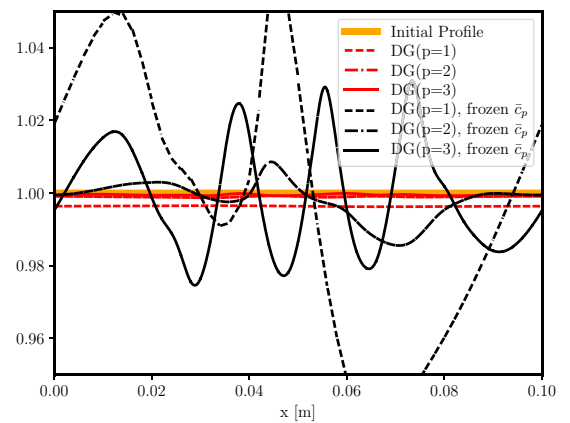
(b) Temperature solutions after one cycle.

Figure 4.4: The pressure and temperature profiles of the $DG(p = 1)$, $DG(p = 2)$, and $DG(p = 3)$ solutions after one cycle for the advection of both discontinuous species and temperature profiles. The initial condition is given by (4.1) and the piece-wise constant temperature profile is given by (4.2). The frozen c_p solution at 100 steps is shown in grey. The solutions were computed without additional stabilization, e.g., artificial viscosity, limiting, or filtering, in order to emphasize the effect of the thermodynamic formulation on the generation of unphysical pressure oscillations.

Figures 4.5a and 4.5b present the temperature and pressure solutions, respectively, for the formulation with exact thermodynamics and the formulation with frozen \bar{c}_p after 100 cycles, i.e. $t = 1$ s. The temperature profiles become more diffuse with the larger number of cycles (see Figure 4.4b for the comparison of one cycle). The pressure oscillations for the formulation with exact thermodynamics cause the ambient pressure to fall below 1 atm. This departure from ambient was improved by increasing the approximation order from $DG(p = 1)$ to $DG(p = 3)$. The pressure oscillations for the 100 cycle solution using the formulation with frozen \bar{c}_p grew in time regardless of approximation order as shown in Figure 4.4a for the one cycle solution for frozen \bar{c}_p . Furthermore, the oscillations associated with the frozen \bar{c}_p formulation are an order of magnitude larger than the oscillations associated with the formulation using exact thermodynamics.



(a) Temperature solutions after 100 cycles.



(b) Pressure solutions after 100 cycles.

Figure 4.5: The pressure and temperature profiles for $DG(p = 1)$, $DG(p = 2)$, and $DG(p = 3)$ solutions after 100 cycles for the advection of both discontinuous species and temperature profiles. The initial condition is given by (4.1) and the piece-wise constant temperature profile is given by (4.2). The solutions were computed without additional stabilization, e.g., artificial viscosity, limiting, or filtering, in order to emphasize the effect of the thermodynamic formulation on the generation of unphysical pressure oscillations.

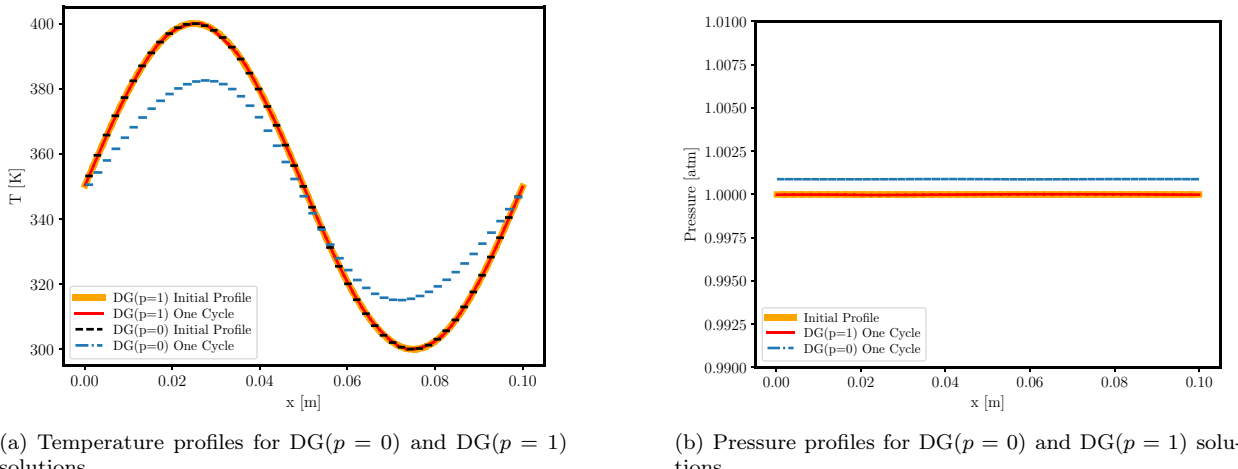
4.3. Discrete pressure equilibrium $DG(p = 0)$

It is important to note that the $DG(p = 0)$ method is equivalent to low order finite volume methods. For $DG(p > 0)$ discrete approximation can accurately represent a continuous solution, however, for $DG(p = 0)$ the discrete approximation is inherently discontinuous. These discontinuities cause unphysical pressure oscillations for species that are nonlinear with respect to temperature as shown in Section 4.2. As such, we expect the method to generate unphysical pressure oscillations for smooth profiles of temperature.

Again, we consider the discontinuous species profile given by (4.1) and introduce a continuous variation in temperature, defined as

$$T = 350 + 50 \sin(20\pi x) \text{ K.} \quad (4.3)$$

Figure 4.6a and 4.6b show the initial and final profiles of temperature and pressure, respectively, for solutions using $DG(p = 1)$ and $DG(p = 0)$. The initial temperature profile for $DG(p = 1)$ is represented smoothly, whereas the initial profile using $DG(p = 0)$ is piecewise constant. The initial discontinuities between adjacent elements in the $DG(p = 0)$ solution lead to small pressure oscillations. After one cycle the pressure errors have dispersed and the overall pressure has diverged by 0.1 % for $DG(p = 0)$. As expected the $DG(p = 1)$ pressure does not diverge from the expected constant solution after one cycle and is consistent with the initial profile.



(a) Temperature profiles for $DG(p = 0)$ and $DG(p = 1)$ solutions.

(b) Pressure profiles for $DG(p = 0)$ and $DG(p = 1)$ solutions.

Figure 4.6: The temperature and pressure profiles of the $DG(p = 0)$ and $DG(p = 1)$ solutions after one cycle for the advection of a species discontinuity (4.1) and a continuous temperate profile, $T = 350 + 50 \sin(20\pi x)$ K.

Although not the focus of this manuscript, it is worth noting that discontinuous discrete solution corresponding to $DG(p = 0)$ generates unphysical pressure oscillations even when the formulation with exact thermodynamics is used. However, it is also important to note that the solution remains stable even in the presence of unphysical pressure oscillations. Finally, these issues are not present for $DG(p > 0)$ solutions as temperature and pressure equilibrium are maintained in well resolved regions of the flow.

4.4. Thermal bubble

Here we present the one dimensional thermal bubble test case previously presented by [16]. For this test case, a periodic 50 m domain, $(-25, 25)$ m, with grid spacing $h = 0.5$ m, and the following initial conditions

$$\begin{aligned}
v &= 1 \text{ m/s}, \\
Y_{H_2} &= \frac{1}{2} [1 - \tanh(|x| - 10)], \\
Y_{O_2} &= 1 - Y_{H_2}, \\
T &= 1200 - 900 \tanh(|x| - 10) \text{ K}, \\
p &= 1 \text{ bar}.
\end{aligned} \tag{4.4}$$

The test case is run for 1 cycle, $t = 50$ s, using $\text{DG}(p = 2)$ with $\text{CFL} = 0.1$ and the inviscid, non-reacting formulation of Equations (3.6)-(3.8). No artificial viscosity or limiting is used in this test case. The mesh resolution was too coarse to stably compute a $\text{DG}(p = 1)$ solution without artificial viscosity, limiting, or filtering. Like the previous test cases, the analytical solution after one cycle is the same as the initial profile. Figures 4.7a and 4.7b show the results for pressure and temperature, respectively. The pressure is constant throughout for both the formulation with exact thermodynamics and the formulation with frozen \bar{c}_p having variations on the order of 10^{-5} atm. The pressure for the formulation with frozen c_p fluctuates on the order of 10% of the expected ambient pressure. Previous work reported that without the double flux method the pressure fluctuated throughout the solution by 3% of the expected ambient pressure for frozen thermodynamic formulations [16]. These issues do not occur in the solutions corresponding to the formulation presented in this work when the thermodynamic quantities are computed exactly and or frozen and \bar{c}_p is correctly evaluated.

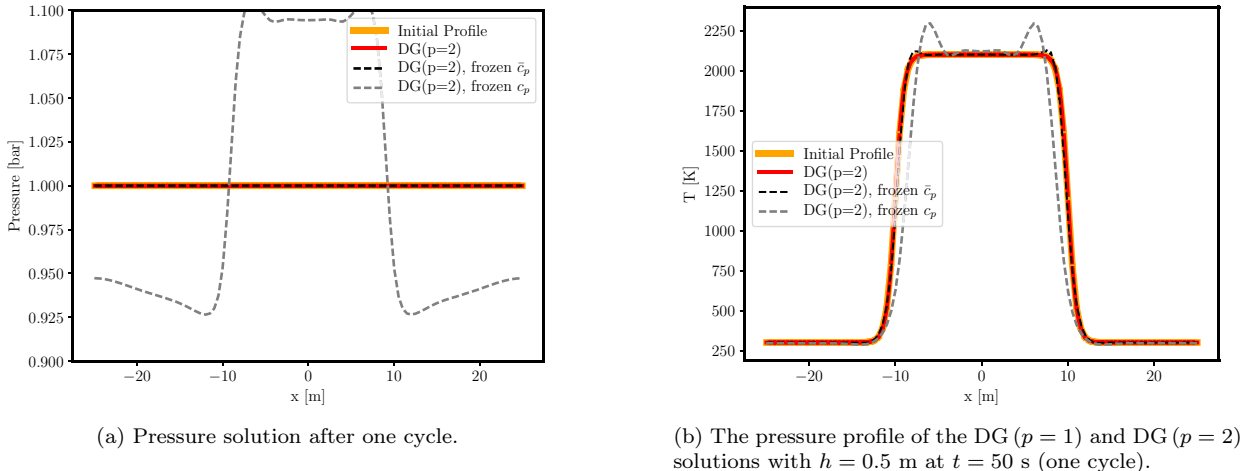
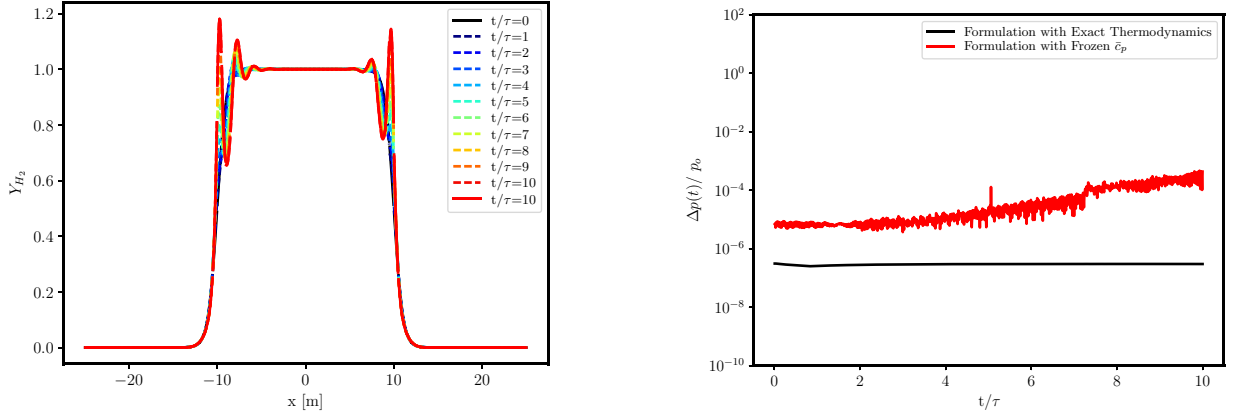


Figure 4.7: The temperature and pressure profiles of the $\text{DG}(p = 2)$ solutions for advection of a thermal bubble (4.4) after one cycle. The solutions were computed without additional stabilization, e.g., artificial viscosity, limiting, or filtering, in order to emphasize the effect of the thermodynamic formulation on the generation of unphysical pressure oscillations.

The formulation with frozen \bar{c}_p does not generate large pressure fluctuations after one cycle. This is due to the fact that the concentrations are represented as a smooth continuous profile, which results in less numerical mixing than the discontinuous interfaces present in the previous test cases. However, after 10 cycles, numerical mixing does occur. Figure 4.8a presents the mass fraction profiles of H_2 for all 10 cycles using the formulation with exact thermodynamics. Without additional stabilization, the species concentrations eventually oscillate in regions of the flow with steep gradients. Figure 4.8b presents the deviation from initial pressure, $\Delta p = p - p_0$, normalized by the initial pressure, $p_0 = 1$ bar as a function of physical time, t , which itself is normalized by the cycle time, $\tau = 50$ s. The error in the formulation with frozen \bar{c}_p has errors that grow to be two orders of magnitude greater than the formulation with exact thermodynamics, which does not grow despite the numerical mixing after 10 cycles.



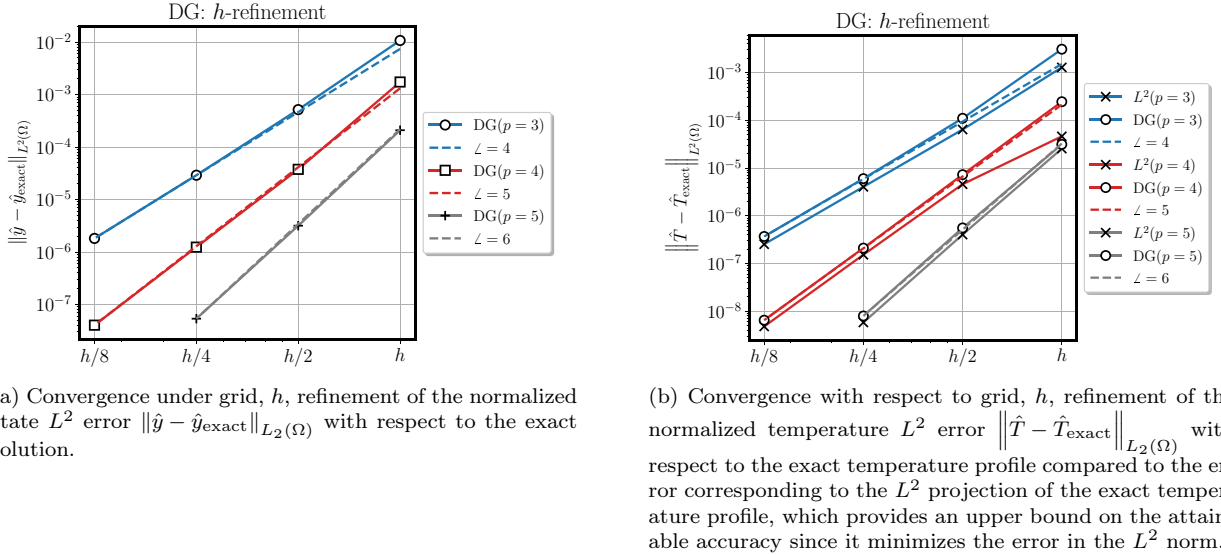
(a) The hydrogen mass fraction profile of the DG ($p = 2$) solution after each cycle for a total of ten cycles using the formulation with exact thermodynamics..

(b) The temporal evolution of the deviation of the pressure from the initial pressure for the DG ($p = 2$) solutions.

Figure 4.8: The hydrogen mass fraction profile and the temporal evolution of the deviation of the pressure from the initial pressure for the DG ($p = 2$) solution after ten cycles for advection of a thermal bubble (4.4). The solutions were computed without additional stabilization, e.g., artificial viscosity, limiting, or filtering, in order to emphasize the effect of the thermodynamic formulation on the generation of unphysical pressure oscillations.

4.4.1. Convergence under grid refinement

As stated in Section 3.1, the expected order of accuracy for the RK2+DG method presented in this work is $\mathcal{O}(h^{p+1} + \tau^2)$. Since we wish to verify that the spatial discretization converges under grid refinement with the optimal rate, we seek to minimize the error due to the temporal discretization by restricting the time-step using a CFL = 0.1 and integrated temporally via SSP-RK3, as opposed to the SSP-RK2 method we apply throughout this work. Therefore, we expect the order of accuracy of the discretization, under these circumstances, to be approximately $\mathcal{O}(h^{p+1})$.



(a) Convergence under grid, h , refinement of the normalized state L^2 error $\|\hat{y} - \hat{y}_{\text{exact}}\|_{L^2(\Omega)}$ with respect to the exact solution.

(b) Convergence with respect to grid, h , refinement of the normalized temperature L^2 error $\|\hat{T} - \hat{T}_{\text{exact}}\|_{L^2(\Omega)}$ with respect to the exact temperature profile compared to the error corresponding to the L^2 projection of the exact temperature profile, which provides an upper bound on the attainable accuracy since it minimizes the error in the L^2 norm.

Figure 4.9: Convergence under grid refinement for the advection of a thermal bubble at time $t = 5$ s on a grid consisting linear line elements with $h = 1$ m, where the initial condition is given by (4.4). The RKDG spatial discretization converges with the expected optimal $(p+1)$ rate, thus confirming that the multi-component formulation behaves exactly like its single-component counterpart, achieving high-order accuracy in smooth regions of the flow.

The expected order of convergence is verified for the advection of a thermal bubble at time $t = 5$ s, corresponding to one tenth of a cycle, on coarse grid, $h = 1$ m, consisting of linear line elements, where the initial condition given by (4.4). We compute the L_2 error in terms of normalized values, defined via the following relationships

$$T = \hat{T} \cdot T_{\text{ref}}, \quad \rho = \hat{\rho} \cdot \rho_{\text{ref}}, \quad v_i = \hat{v}_i \cdot \sqrt{p_{\text{ref}}/\rho_{\text{ref}}}, \quad \rho e_t = \hat{\rho} \hat{e}_t \cdot p_{\text{ref}}, \quad C_i = \hat{C}_i \cdot p_{\text{ref}} / (R^0 \cdot T_{\text{ref}}), \quad (4.5)$$

where $T_{\text{ref}} = 1000$ K, $\rho_{\text{ref}} = 1 \text{ kg} \cdot \text{m}^{-3}$, and $p_{\text{ref}} = 101325$ Pa are reference values. Figures 4.9a and 4.9b present the convergence results corresponding to the normalized conserved state and the normalized temperature, respectively. The solutions corresponding to DG ($p = 3$), DG ($p = 4$), and DG ($p = 5$) were refined until the error associated with the conserved state was on the order of the time-step at which point error associated with the temporal integration began to pollute the results. Both the conserved state and the nonlinear temperature converge at the expected rate for DG ($p = 3$), DG ($p = 4$), and DG ($p = 5$) as shown in Figure 4.9a and 4.9b. Thus confirming that, in the case of convergence under grid refinement, the multi-component formulation behaves exactly like its single-component counterpart, achieving high-order accuracy in smooth regions of the flow.

In order to access the accuracy of the formulation in relation to other methods, Figure 4.9b also compares the normalized temperature L^2 error $\|\hat{T} - \hat{T}_{\text{exact}}\|_{L^2(\Omega)}$ to the error corresponding to the L^2 projection of the exact temperature profile, which minimizes the error in the L^2 norm, thus providing an upper bound on the attainable accuracy. As solution is better resolved, i.e., smaller h or larger p , the DG approximation approaches the L^2 projection in terms of accuracy. Finally, there is zero temporally integration error associated with the L^2 projection of the exact solution, which might account for the small differences still present in errors associated with the most well resolved approximations as the temporally integration error was limiting but did not vanish in the case of the DG approximations.

4.5. Concluding remarks regarding discrete pressure equilibrium at material interfaces

In the previous Sections we presented several test cases to assess when pressure oscillations would be generated for multi-component non-reacting flows without physical diffusion. Additional stabilization, e.g.,

artificial viscosity, limiting, or filtering, was not applied in any of the test cases to avoid the unintentional suppression of pressure oscillations. The results confirm the analysis presented in Appendix C and are summarized below.

In the case of frozen thermodynamics, unphysical pressure oscillations are generated at material interfaces and in smooth regions where mixing occurs, requiring additional stabilization, or nonconservative methods. The magnitude of the oscillations depends on the method with which \bar{c}_p is evaluated. Furthermore, these oscillations are dependent on size of time step and grow as the solution evolves, even in smooth regions of the flow, as shown in Figure 4.8b.

In contrast, if the thermodynamics are evaluated exactly, pressure oscillations are not generated when the temperature is continuous, regardless of species mixing at material interfaces. However, pressure oscillations are generated at temperature discontinuities but do not cause the solution to diverge, as the oscillations do not grow as the solution evolves. Finally, pressure oscillations are not generated in regions of sharp continuous profiles of species and temperature, as described in Section 4.4.

Therefore, we expect the $DG(p > 0)$ formulation for the multi-component reacting Navier-Stokes flows described in this work to behave no differently than its counterpart for single-component Navier-Stokes flows, namely: high order accuracy is achieved in smooth regions of the flow and additional stabilization of the form (3.68) is only required in the presence of discontinuities.

5. Results

In order to demonstrate the practicality of the conservative DG method described in this work, we apply it to both reacting and non-reacting multi-component flows. We have selected challenging problems in one, two, and three dimensions that showcase the ability of the discretization to stably compute solutions to problems with both discontinuous interfaces and sharp, but smooth, gradients, while maintaining conservation without generating unphysical pressure oscillations. The first two test cases, presented in Section 5.1 and Section 5.2, approximate the interaction of shocks with multi-component non-reacting gases for cases previously reported in literature.

The final four test cases, presented in Sections 5.3-5.6, consider chemically reacting multi-component flows. The ODEs describing the chemical reactions are all solved using DGODE. The first two test cases, presented in Section 5.3 and Section 5.4, explore sustained detonations formed via an overdriven initialization. These cases require artificial viscosity to stabilize the large pressure and temperature discontinuity present in the region of the detonation.

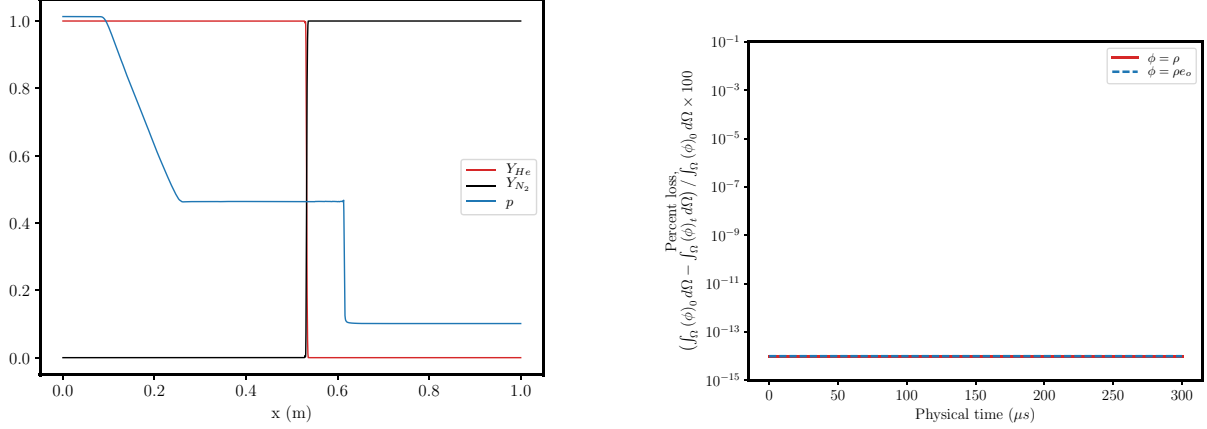
The last two test cases, presented in Section 5.5 and Section 5.6, correspond to full multi-component reacting Navier-Stokes solutions where the thermodynamics and transport properties were given by the *tran.dat* file provided by USC Mech II [69]. The chemically reacting shear layer cases did not require artificial viscosity to run stably.

5.1. One-dimensional non-reacting multi-component shock tube

This case was first presented by Houim and Kuo [27]. A 1 m long one-dimensional domain, $(0, 1)$ m, with walls at both ends, and grid spacing $h = 0.0005$ m is used with the following initial conditions

$$(v_1, T, p, Y_{N_2}, Y_{He}) = \begin{cases} (0 \text{ m/s}, 300 \text{ K}, 1 \text{ atm}, 1, 0) & x > 0.4 \\ (0 \text{ m/s}, 300 \text{ K}, 10 \text{ atm}, 0, 1) & x < 0.4 \end{cases}. \quad (5.1)$$

Figure 5.1b presents the mass fraction profiles for He and N_2 , as well as the pressure, p , profile normalized by 10 atm at time $t = 300 \mu\text{s}$ computed using $DG(p = 2)$ on 2000 linear line elements. The shock front is maintained without spurious pressure oscillations. The exact shock speed calculated by Houim and Kuo [27] was 712 m/s and our solution gave a shock speed of 711.9 m/s. Figure 5.1b shows the energy conservation percent loss and density conservation percent loss as a function of physical time which stays at the expected machine precision of $10^{-14}\%$ assuring that this formulation is indeed conservative.



(a) The mass fraction profiles for He and N_2 , as well as the pressure, p , normalized by 10 atm, at time $t = 300 \mu s$. The initialization is given by (5.1). The estimated shock speed of 711.9 m/s is in close agreement with the exact value 712 m/s [27], as is expected for a fully conservative discretization.

(b) Percent loss of conservation quantities, $(f_\Omega(\phi)_0 - f_\Omega(\phi)_t) / f_\Omega(\phi)_0 \times 100$, for the one-dimensional multi-component shock tube computed as a function of physical time computed using the initial integrated quantity, $\int_\Omega(\phi)_0 d\Omega$, and current integrated quantity, $\int_\Omega(\phi)_t d\Omega$, where $\phi = \rho e_t$ for total energy and $\phi = \rho$ for density. The conservation error is on the order of $10^{-14}\%$.

Figure 5.1: Solution and conservation error for the one-dimensional multi-component shock tube computed using DG ($p = 2$) on a grid consisting of linear line elements with $h = 0.0005$ m. The initialization is given by (5.1).

5.2. Two-dimensional non-reacting air shock with helium bubble interaction

This two-dimensional test case is modeled after an experiment of an air shock wave traveling though a suspended helium bubble that was performed by Hass and Sturtevant [70]. Although this configuration is naturally three-dimensional, it has been used previously as a two-dimensional simulation validation case [71, 72, 59, 16]. Here we present the same two-dimensional case as previously simulated on a rectangular domain, $\Omega = (0, 0.325) \text{ m} \times (0, 0.0455) \text{ m}$, that has initial conditions with a normal shock located at $x = 0.225$ m and a helium bubble to the left of the shock,

$$\begin{aligned}
 (v_1, v_2) &= \begin{cases} (M_2 c_2 - M_1 c_1, 0) & x \geq 0.225 \\ (0, 0) \text{ m/s} & x < 0.225 \end{cases}, \\
 Y_{N_2} &= \begin{cases} 0.785 & \sqrt{(x - 0.175)^2 + y^2} \geq 0.025 \text{ m} \\ 0 & \sqrt{(x - 0.175)^2 + y^2} < 0.025 \text{ m} \end{cases} \\
 Y_{O_2} &= \begin{cases} 0.215 & \sqrt{(x - 0.175)^2 + y^2} \geq 0.025 \text{ m} \\ 0 & \sqrt{(x - 0.175)^2 + y^2} < 0.025 \text{ m} \end{cases}, \\
 Y_{He} &= \begin{cases} 0 & \sqrt{(x - 0.175)^2 + y^2} \geq 0.025 \text{ m} \\ 1 & \sqrt{(x - 0.175)^2 + y^2} < 0.025 \text{ m} \end{cases}, \\
 T &= \begin{cases} 300 \frac{T_2}{T_1} \text{ K} & x \geq 0.225 \\ 300 \text{ K} & x < 0.225 \end{cases}, \\
 p &= \begin{cases} \frac{p_2}{p_1} \text{ bar} & x \geq 0.225 \\ 1 \text{ bar} & x < 0.225 \end{cases}.
 \end{aligned} \tag{5.2}$$

where $c = \sqrt{\gamma R T}$ and the normal shock ratios, T_2/T_1 and p_2/p_1 , and post shock Mach number, M_2 , can be calculated from the isentropic flow relations for air $\gamma = 1.4$ which yields, for a $M_1 = 1.22$ normal shock,

$T_2/T_1 = 1.14054133$, $p_2/p_1 = 1.56979999$, and $M_2 = 0.82998648$. The shifting of velocity by the pre-shock velocity condition gives an inflow boundary condition on the right hand side. For this configuration we used the unstructured linear triangular grid shown in Figure 5.2. The grid is built so that it is refined where the shock and bubble interact. The grid has a target grid spacing of $h = 0.005$ m on the left and right boundaries and refines to $h = 0.0001$ m where the shock and bubble interact. We also constructed the mesh so that the helium bubble is initially grid aligned.

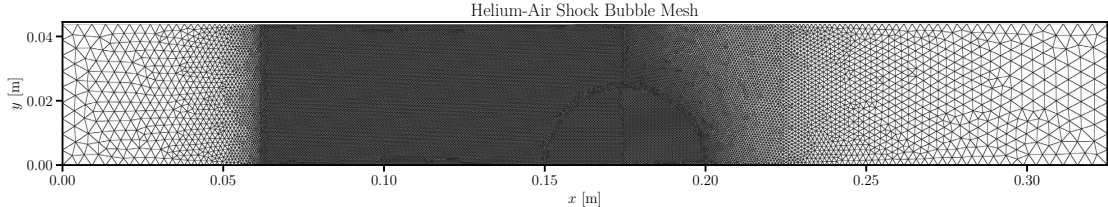
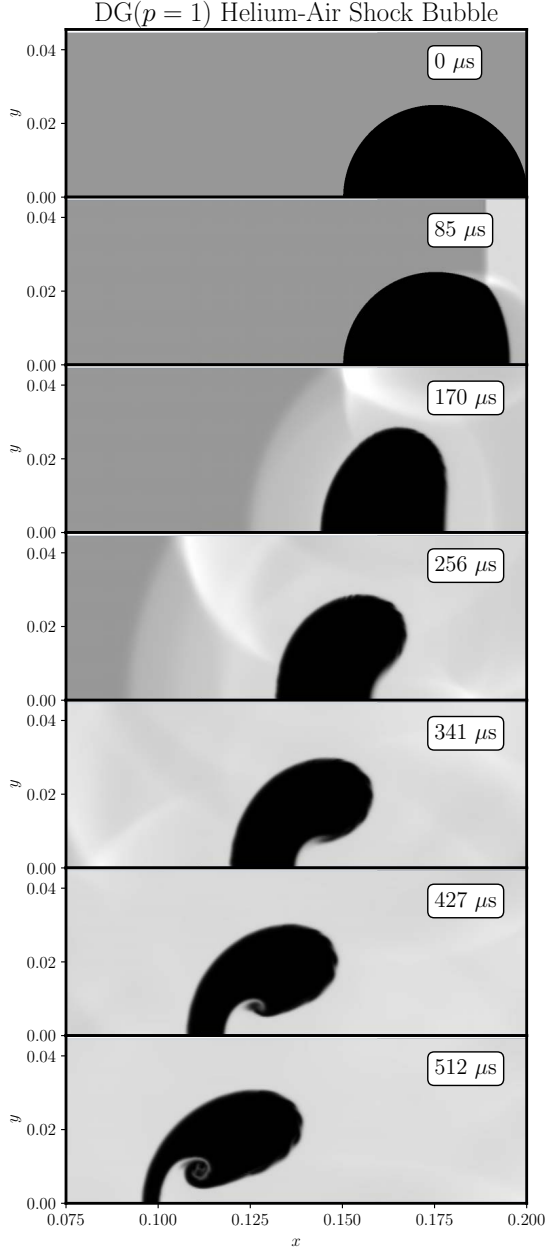


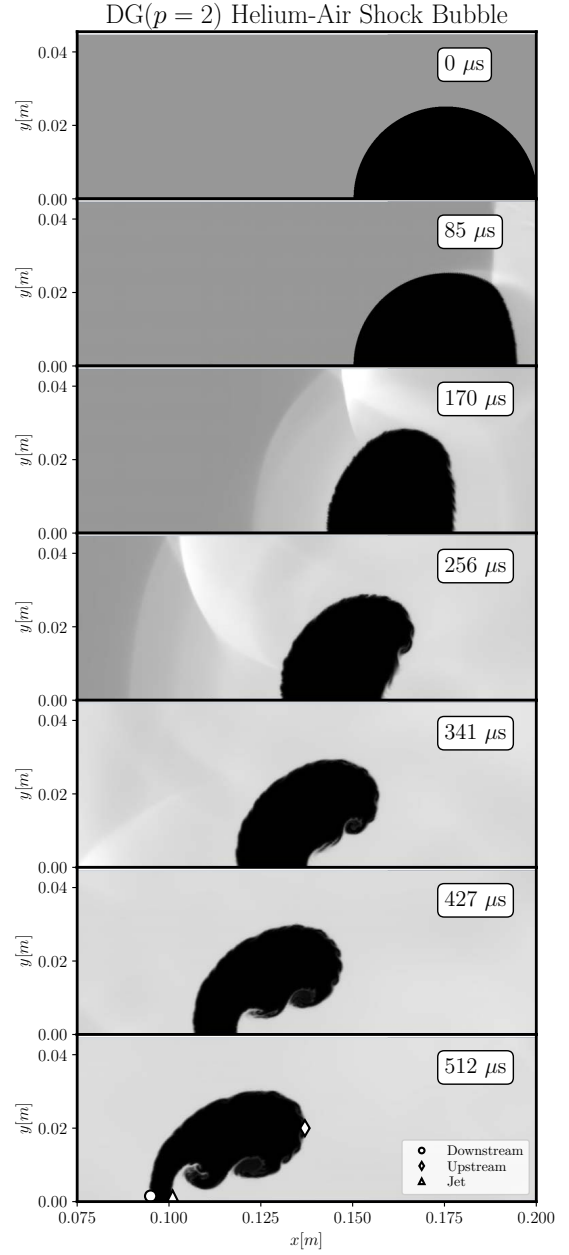
Figure 5.2: Unstructured mesh for Helium-air shock bubble test case.

The evolution of the helium bubble as it interacts with the shock is shown for DG ($p = 1$) and DG ($p = 2$) in Figures 5.3a and 5.3b, respectively. The shock wave collides with the helium bubble and causes compression and expansion as well as mixing of the helium into the surrounding air. The DG ($p = 2$) solution more accurately resolves this interaction of the pressure waves than the DG ($p = 1$) solution. Additionally, the mixing of the helium on the left and right sides of the bubble are more resolved with the DG ($p = 2$) solution. For these simulations we did not notice any spurious pressure oscillations at the material interfaces, as is expected based on the results presented in Section 4 as the shock waves are stabilized with the addition of artificial viscosity, resulting in sharp, yet smooth, profiles in temperature and pressure.

We have labeled three points as downstream, jet, and upstream for the solution at time $t = 512 \mu\text{s}$ in Figure 5.3b. The downstream point is the left-most location of the helium bubble, the jet point is the right-most location of the helium bubble at $y = 0$ m, and the upstream point is the right-most location of the helium bubble in the entire domain. The impact of the shock on the helium bubble causes these locations to move as a function of time, where the jet and downstream location eventually merge. Figure 5.4 shows the trajectory of these points for the DG ($p = 2$) solution and agrees well with the accompanying solid lines from [73].



(a) Density profile using DG ($p = 1$) for shock and helium bubble interaction at different times.



(b) Density profile using DG ($p = 2$) for shock and helium bubble interaction at different times.

Figure 5.3: Density profile snapshots for DG ($p = 1$) and DG ($p = 2$) at different times. The initialization is given by (5.2). Unphysical pressure oscillations at the material interface were not observed as pressure and temperature discontinuities were stabilized with the addition of artificial viscosity, resulting in sharp, yet continuous, profiles, thus confirming the results presented in Section 4.

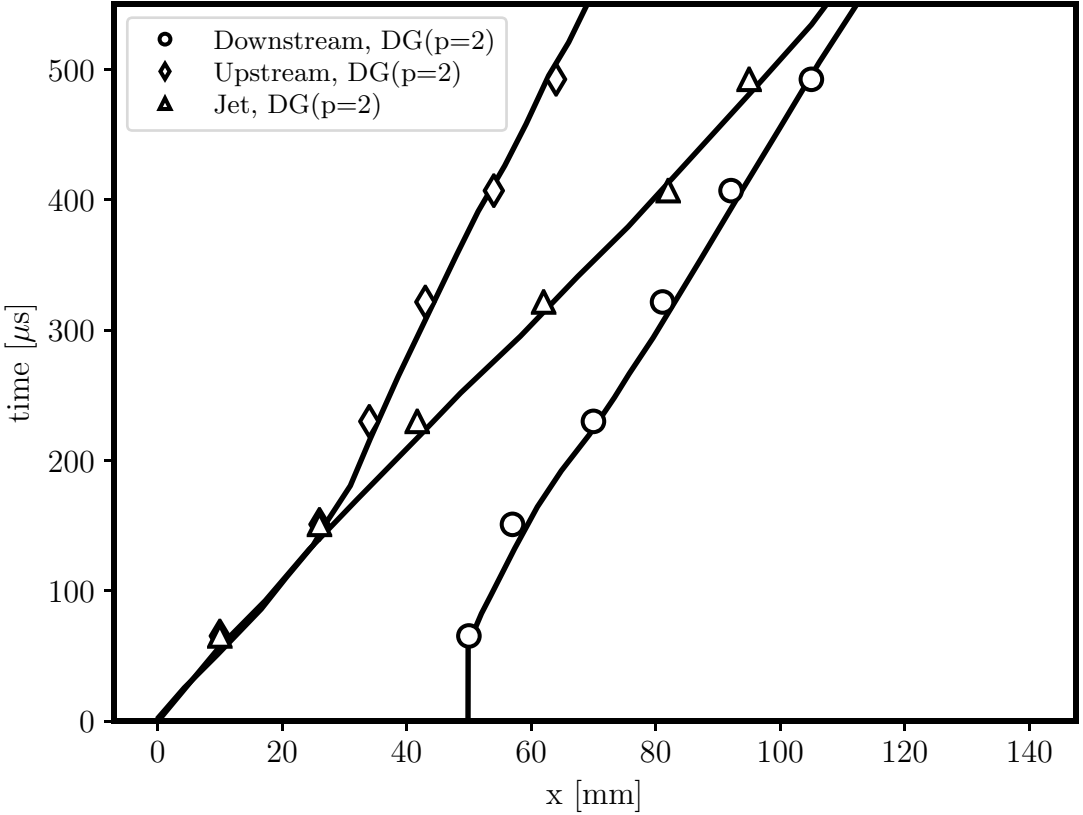


Figure 5.4: Front Locations for the DG ($p = 2$) solution (symbols) and accompanying data from [73] (solid lines).

5.3. One-dimensional detonation wave

Here we present a one-dimensional hydrogen-oxygen detonation wave diluted in Argon. A 0.45 m long one-dimensional domain, $(0, 0.45)$ m, with walls at both ends and grid spacing, $h = 9 \times 10^{-5}$ m is used with the following initial conditions

$$\begin{aligned}
 v_1 &= 0 \text{ m/s,} \\
 X_{Ar} : X_{O_2} : X_{H_2} &= 7 : 1 : 2 \quad x > 0.025 \text{ m,} \\
 X_{Ar} : X_{O_2} : X_{H_2} : X_{OH} &= 7 : 1 : 2 : 0.01 \quad 0.015 \text{ m} < x < 0.025 \text{ m,} \\
 X_{Ar} : X_{H_2O} : X_{OH} &= 8 : 2 : 0.01 \quad x < 0.015 \text{ m,} \\
 p &= \begin{cases} 5.50e5 & \text{Pa} \\ 6.67e3 & \text{Pa} \end{cases} \quad \begin{cases} x < 0.015 \text{ m} \\ x > 0.015 \text{ m} \end{cases}, \\
 T &= \begin{cases} 298 & \text{K} \\ 350 & \text{K} \\ 3500 & \text{K} \end{cases} \quad \begin{cases} x > 0.025 \text{ m} \\ 0.015 \text{ m} < x < 0.025 \text{ m} \\ x < 0.015 \text{ m} \end{cases}.
 \end{aligned} \tag{5.3}$$

The region $0.015 \text{ m} < x < 0.025 \text{ m}$ has a small amount of OH -radical with the premixed fuel to encourage reactivity as the large shock moves to the right from the region with the initial driver pressure, $x < 0.015 \text{ m}$. The detailed chemical kinetics are described by the reaction mechanism of Westbrook [74]. This test case is similar to the cases presented by [27] and [16] with the difference being in the initialization. Regardless of the initialization, the final detonation will correspond to the Chapman-Jouget detonation solution for a mixture with the mole fraction ratios $X_{Ar} : X_{O_2} : X_{H_2} = 7 : 1 : 2$.

Figure 5.5 shows the temperature, adapted polynomial degree of the DGODE approximation, heat release, $-\sum_{k=1}^{n_s} \omega_k W_k h_k^0$, and pressure as function of distance as the detonation evolves in time. Initially a shock travels to the right with a reaction zone lagging behind the high pressure front, as indicated by the heat release at solution times $31 \mu\text{s}$ and $62 \mu\text{s}$. As the reactivity increases the largest heat release reaches the shock front, at solution time $94 \mu\text{s}$, and a steady detonation front is achieved and maintained, as shown for solution times greater than $125 \mu\text{s}$.

For the steady detonation, the polynomial degree of the DGODE approximation is greatest at the detonation front, reaching a value of $p = 2$, and relaxes to $p = 0$ as the distance from the detonation increases. At start-up, the polynomial degree of the DGODE approximation is $p = 1$ in the high temperature regions where the initialization is only water and hydroxyl. This is due to the large initial temperature, $T = 3500 \text{ K}$, in the driver zone that causes backwards reactions. As the temperature in this region decreases due to the backwards moving expansion, the polynomial degree of the DGODE approximation decreases accordingly, as can be seen with solutions at time $31 \mu\text{s}$ and $62 \mu\text{s}$. A spike in the polynomial degree of the DGODE approximation exists to the left of the detonation wave for the solution at time $94 \mu\text{s}$. This location has a weaker discontinuity than the detonation but is strong enough to offset the reacted zone away from chemical equilibrium to require high-order chemistry integration.

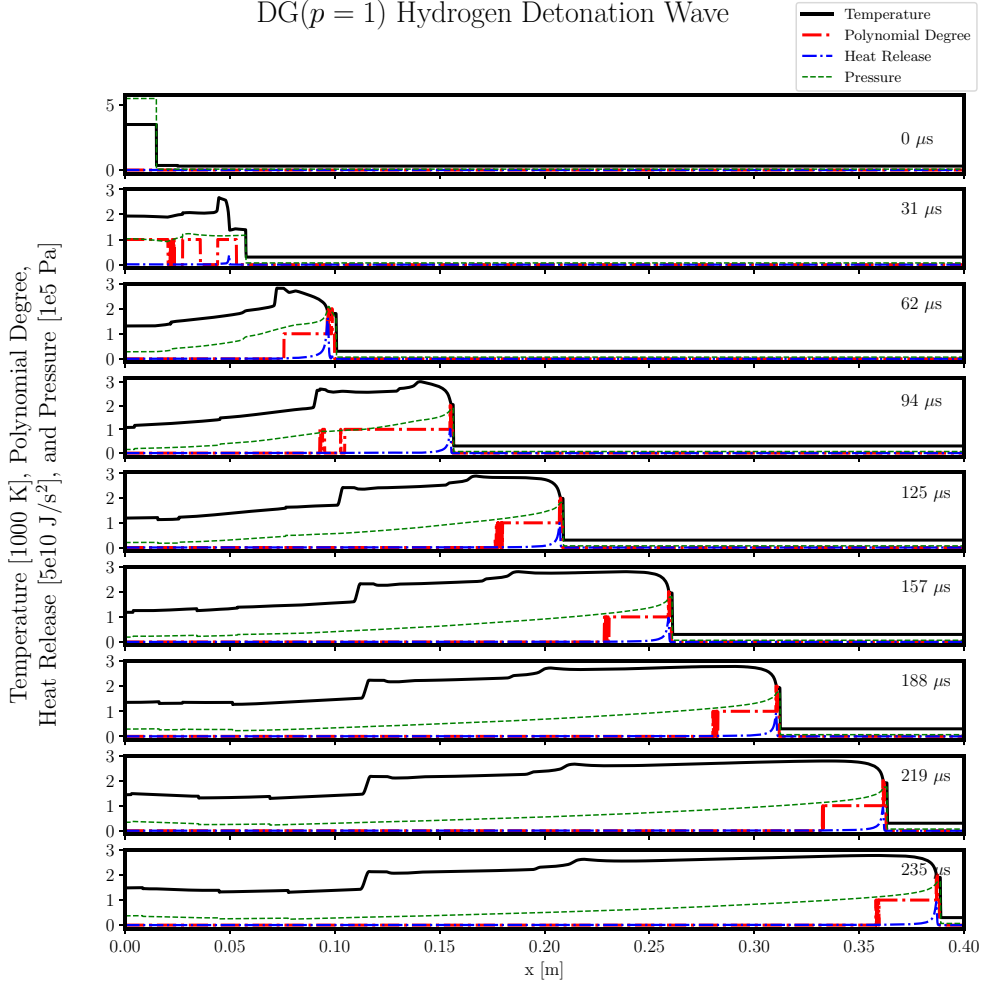
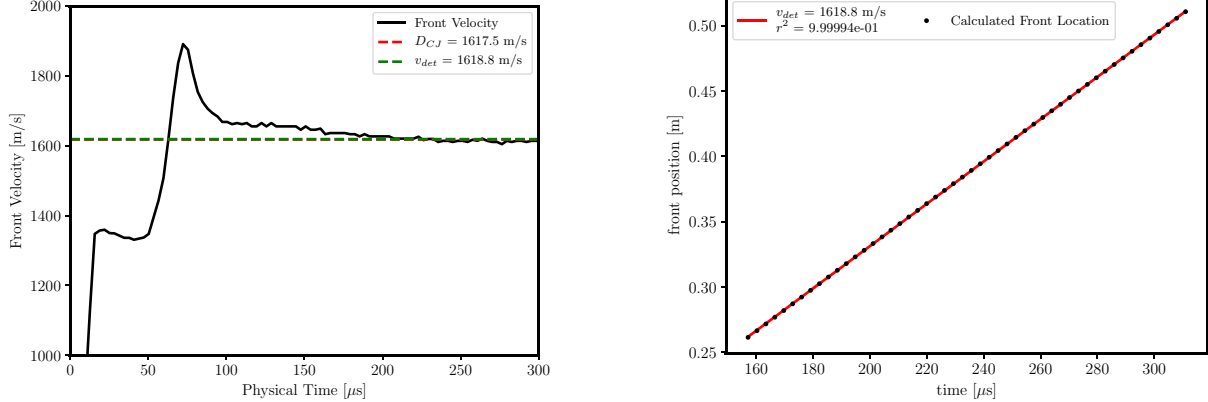


Figure 5.5: One-dimensional hydrogen detonation test case temperature and pressure evolution from a high pressure and high temperature initialization to a steady traveling detonation front. Heat release, $-\sum_{k=1}^{n_s} \omega_k W_k h_k^0$, and DGODE polynomial degree are also shown to indicate areas of chemical activity and stiffness. The discontinuous solution at the detonation front is stabilized with the addition of artificial viscosity. The initialization is given by (5.3).

Figure 5.6a shows the velocity of the leading shock front as function of time. We define the front location as the right most location where the jump in temperature from 300 K was larger than 10 K and a second order finite differencing scheme was used to calculate the instantaneous velocity. Initially, the front moves as a detached oblique shock traveling through the unreacted medium, as seen in solution time 40-80 μ s. Eventually the reaction zone behind the front begins to influence the shock and an overdriven detonation event occurs. The detonation velocity, v_{det} , falls to the steady value of 1618.8 m/s which was calculated using linear regression with $r^2 = 0.999994$. The calculated front location and the approximated linear propagation using the computed detonation velocity are shown in Figure 5.4. The Chapman-Jouget detonation velocity, $v_{det} = D_{CJ} = 1617.5$ m/s, as well as the post shock profiles for temperature, pressure, and species concentrations can be calculated using Shock and Detonation Toolbox [67]. Figures 5.7a and 5.7b show the solution at time $t = 235$ μ s in direct comparison to the Shock Detonation Toolbox computed results (dashed black lines) for temperature, pressure, and species mass fractions. Additionally, Table 2 summarizes the post shock values and detonation velocity corresponding to the current simulation and compares them with the values calculated using the Shock Detonation Toolbox and the values reported by Houim and Kuo [27] as well as Lv and Ihme [16]. The results presented in this work agree well with all past reported

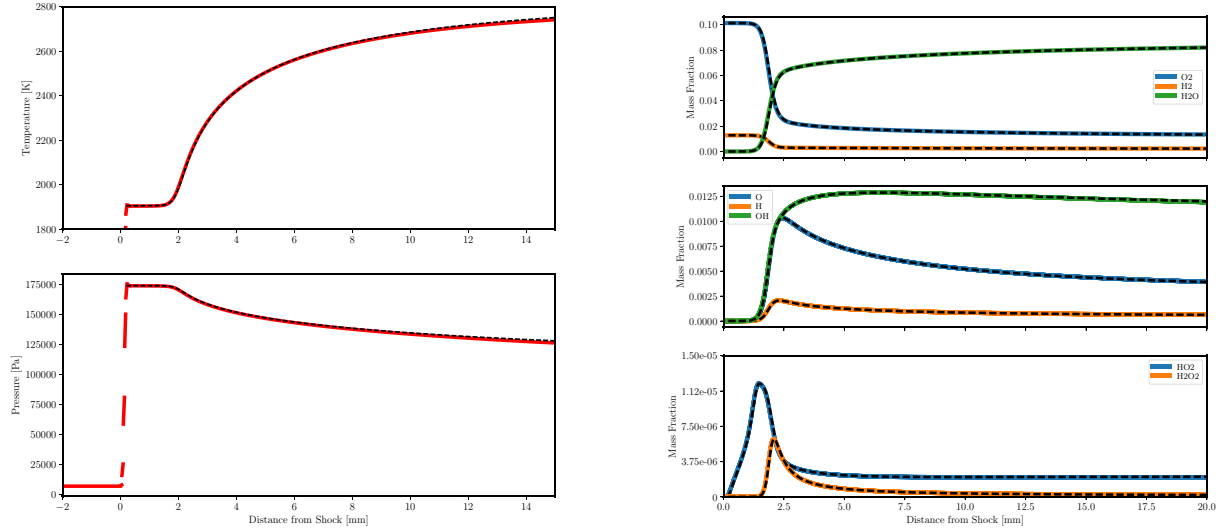
solutions and the Shock Detonation Toolbox in particular.



(a) Velocity of the leading shock front as function of time, the front location is defined as the right most location where the jump in temperature from 300 K was larger than 10 K and a second order finite differencing scheme was used to calculate the instantaneous velocity.

(b) The calculated front location and the approximated linear propagation using the calculated velocity of 1618.8 m/s using linear regression with $r^2 = 0.999994$.

Figure 5.6: Front location and velocity as a function of physical time.



(a) Comparison of the temperature and pressure profiles corresponding to DG ($p = 1$) (solid red lines) and the solution computed via the Shock Detonation Toolbox (dashed black lines) for the one-dimensional hydrogen detonation described in Section 5.3.

(b) Comparison between Shock Detonation Toolbox (dashed black lines) and current simulations (solid colored lines) for species mass fractions.

Figure 5.7: Comparison of the DG ($p = 1$) solution for $h = 9 \times 10^{-5} \text{ m}$ and the solution computed via the Shock Detonation Toolbox at at time $t = 235 \mu\text{s}$ for the one-dimensional hydrogen detonation described in Section 5.3. The discontinuous solution at the detonation front is stabilized with the addition of artificial viscosity.

Table 2: Table of post-shock values for one-dimensional detonation wave case.

Reference	p_{vN} [kPa]	T_{vN} [K]	v_{det} [m/s]
Shock and Detonation Toolbox [67]	173.6	1904.7	1617.5
Current Simulations	173.5	1904.7	1618.8
Houim and Kuo [27]	173.9	1915.2	1619.8
Lv and Ihme [16]	179.4	1926.0	1634.6

Spurious pressure oscillations were not generated during the simulation of this test case, indicating the formulation can stably compute detonations. For this test case, the integrated total energy, $\int_{\Omega} (\rho e_t)_0 d\Omega$, and the density, $\int_{\Omega} (\rho)_0 d\Omega$, are conserved as the domain has walls at both the left and right boundaries. Figure 5.5 shows the percent loss of the integrated total energy, $(\int_{\Omega} (\rho e)_0 d\Omega - \int_{\Omega} (\rho e)_t d\Omega) / \int_{\Omega} (\rho e)_0 d\Omega \times 100$, as well as the percent loss of the integrated density, $(\int_{\Omega} (\rho)_0 d\Omega - \int_{\Omega} (\rho)_t d\Omega) / \int_{\Omega} (\rho)_0 d\Omega \times 100$, as a function of time. The error remains on the order of 1e–13% for the entire simulation which is expected for a conservative method.

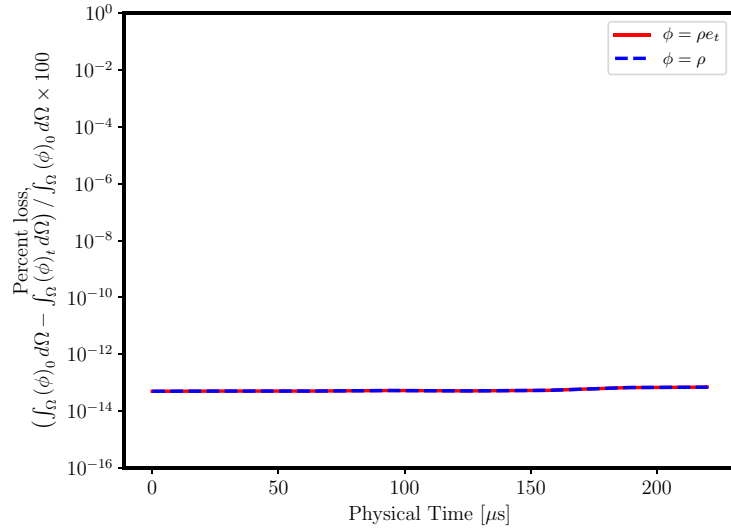


Figure 5.8: Percent loss of conservation quantities, $(\int_{\Omega} (\phi)_0 - \int_{\Omega} (\phi)_t) / \int_{\Omega} (\phi)_0 \times 100$, for the one-dimensional detonation computed using DG ($p = 1$) for $h = 9 \times 10^{-5}$ m as a function of physical time computed using the initial integrated quantity, $\int_{\Omega} (\phi)_0 d\Omega$, and current integrated quantity, $\int_{\Omega} (\phi)_t d\Omega$, where $\phi = \rho e_t$ for total energy and $\phi = \rho$ for density.

5.4. Two-dimensional detonation wave

Here we present the two-dimensional extension of the test case presented in Section 5.3 with a 0.45 m long domain that has a channel height of 0.06 m, $\Omega = (0, 0.45) \text{ m} \times (0, 0.06) \text{ m}$, with a uniform quadrilateral mesh with grid spacing $h = 9 \times 10^{-5}$ m. Each quadrilateral element was split into two triangular elements. The results presented here used a DG ($p = 1$) approximation. The top and bottom boundaries are simulated as walls. The initial conditions are the same as Section 5.3 with the exception of two additional high pressure and high temperature regions, located within the circles $\sqrt{(x - 0.019)^2 + (y - 0.015)^2} = 0.0025$ m and $\sqrt{(x - 0.010)^2 + (y - 0.044)^2} = 0.0025$ m, with conditions

$$\begin{aligned}
 (v_1, v_2) &= (0, 0) \text{ m/s}, \\
 X_{Ar} : X_{H_2O} : X_{OH} &= 8 : 2 : 0.01, \\
 p &= 5.5e5 \text{ Pa}, \\
 T &= 3500 \text{ K}.
 \end{aligned} \tag{5.4}$$

These circular regions were added to perturb the detonation and develop cellular structures and they were aligned with the unstructured grid interfaces at initialization as shown in Figure (5.9). This test case is similar to one performed by Oran et al. [30] with the exception that they initialized their solution from a one-dimensional detonation and their domain was 0.10 m longer, $\Omega = (0, 0.55) \text{ m} \times (0, 0.06) \text{ m}$. Their simulations revealed two detonation cells in the vertical direction with each cell computed to be $(0.055) \text{ m} \times (0.03) \text{ m}$. Their results were consistent with experiments performed by Lefebvre et al. [75]. Houim and Kuo [27], as well as Lv and Ihme [16], ran similar test cases but the domain was half the height of the one considered in this work. Houim and Kuo [27] shifted their simulation to be in the detonation frame of reference whereas Lv and Ihme [16] ran the simulation in the laboratory frame of reference. In both cases, the solutions were initialized from the corresponding one-dimensional detonation solutions. Their simulations revealed one detonation cell, which is consistent with domain height considered in their respective works.

Figure (5.9) presents the temperature solutions as the detonation front progresses through the simulation domain. As the initial shock progresses into the domain, it collides with the two circular high pressure and high temperature regions before $t = 30 \mu\text{s}$, the detonation is then established and the perturbations lead to transverse waves traveling in the vertical directions that reflect off the top and bottom walls. To the left of the detonation, complex, two-dimensional structures develop, including Kelvin–Helmholtz instabilities as well as the triple point that connects the Mach stems and incident shock.

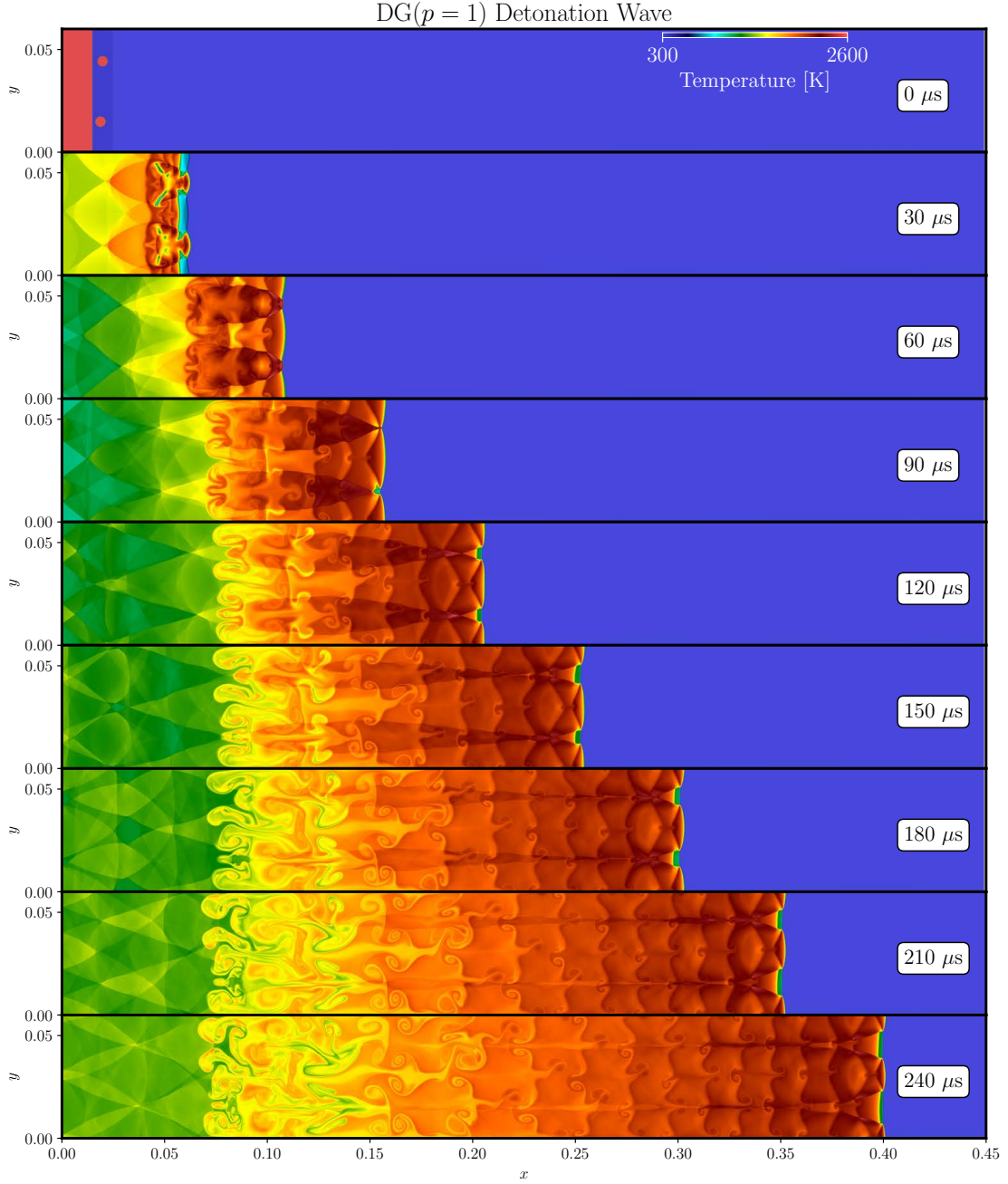


Figure 5.9: Temperature contours for two-dimensional detonation wave. The discontinuous solution at the detonation front is stabilized with the addition of artificial viscosity. The corresponding one-dimensional initialization given by (5.2) is augmented with two additional circular two additional high pressure and high temperature regions (5.3).

Figure (5.10) shows the adapted polynomial degree for the DGODE chemistry solve at each degree of freedom as the detonation propagates through the simulation domain. The adapted polynomial degree is largest in the vicinity of the detonation, reaching $p = 3$ in the regions behind the detonation front and at the triple points. The majority of the adapted polynomial degree reduces to $p = 0$ downstream of the shock. Thin regions of $p = 1$ exist downstream of the shock along the vertically traveling transverse waves. This indicates that the traveling waves are strong enough to push the chemistry out of equilibrium and

require high-order integration to solve the chemistry. These thin regions of higher order are similar to the spike in the adapted polynomial degree as shown in Section 5.3's one-dimensional detonation results at time $t = 94 \mu\text{s}$, see Figure 5.5.

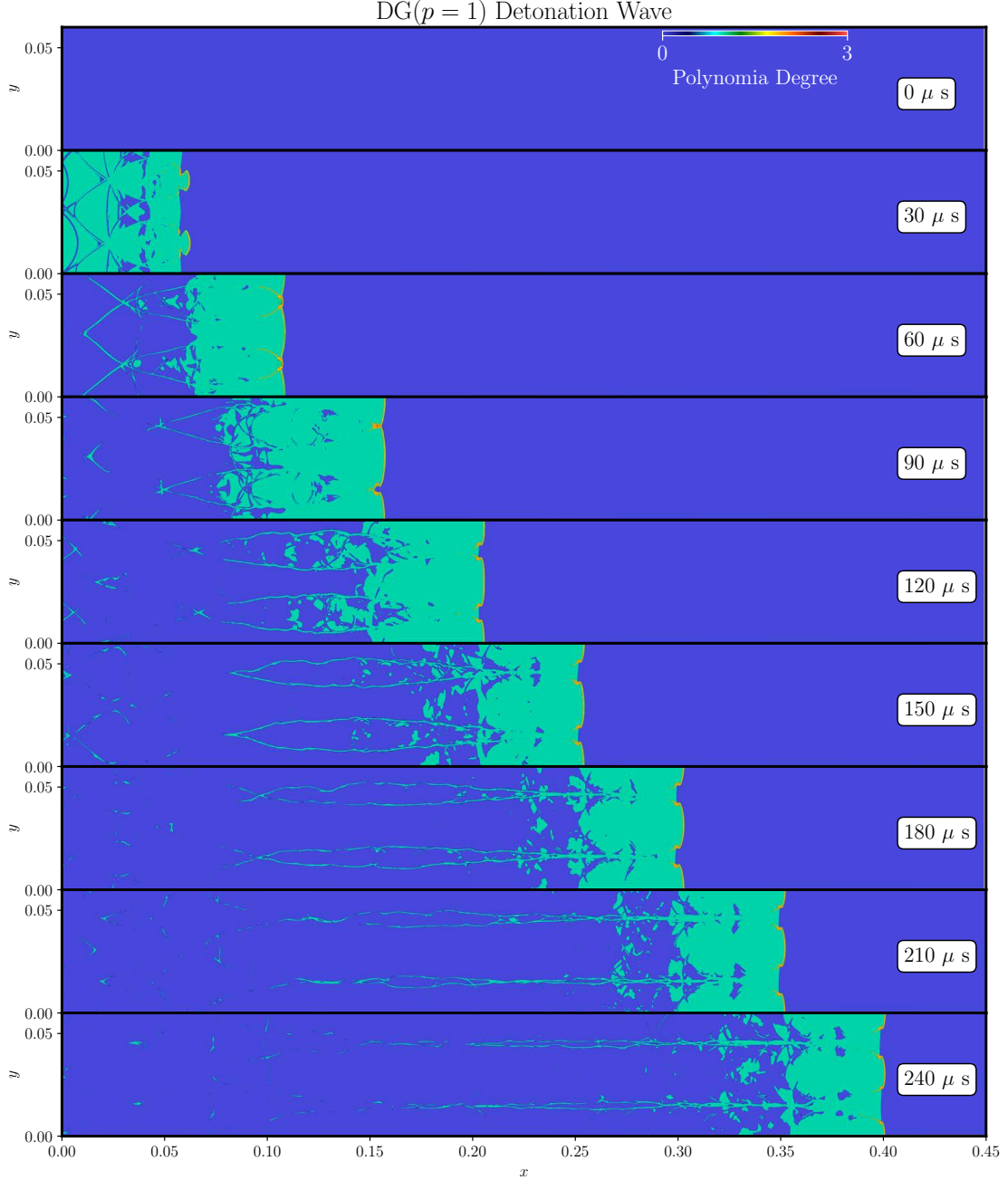


Figure 5.10: The adapted polynomial degree of the DGODE approximation for two-dimensional detonation wave.

Figure 5.11 shows the maximum pressure experienced at each location as the solution evolved, $\max(p, p_{max})$. This metric is a good indicator of the detonation cell structures and shows two distinct detonation cells in the vertical direction. A large burst of pressure exists between $x = 0.04 \text{ m}$ and $x = 0.1 \text{ m}$ from the over

driven detonation as the shock transitions to a detonation in the early stages of development. The last solution, at $t = 240 \mu\text{s}$, displays two dashed white lines that indicated the measured horizontal and vertical size of a detonation cell. For this solution the detonation cell was computed to be $(0.055) \text{ m} \times (0.03) \text{ m}$ which is consistent with experimental work [75] and previous numerical results [30].

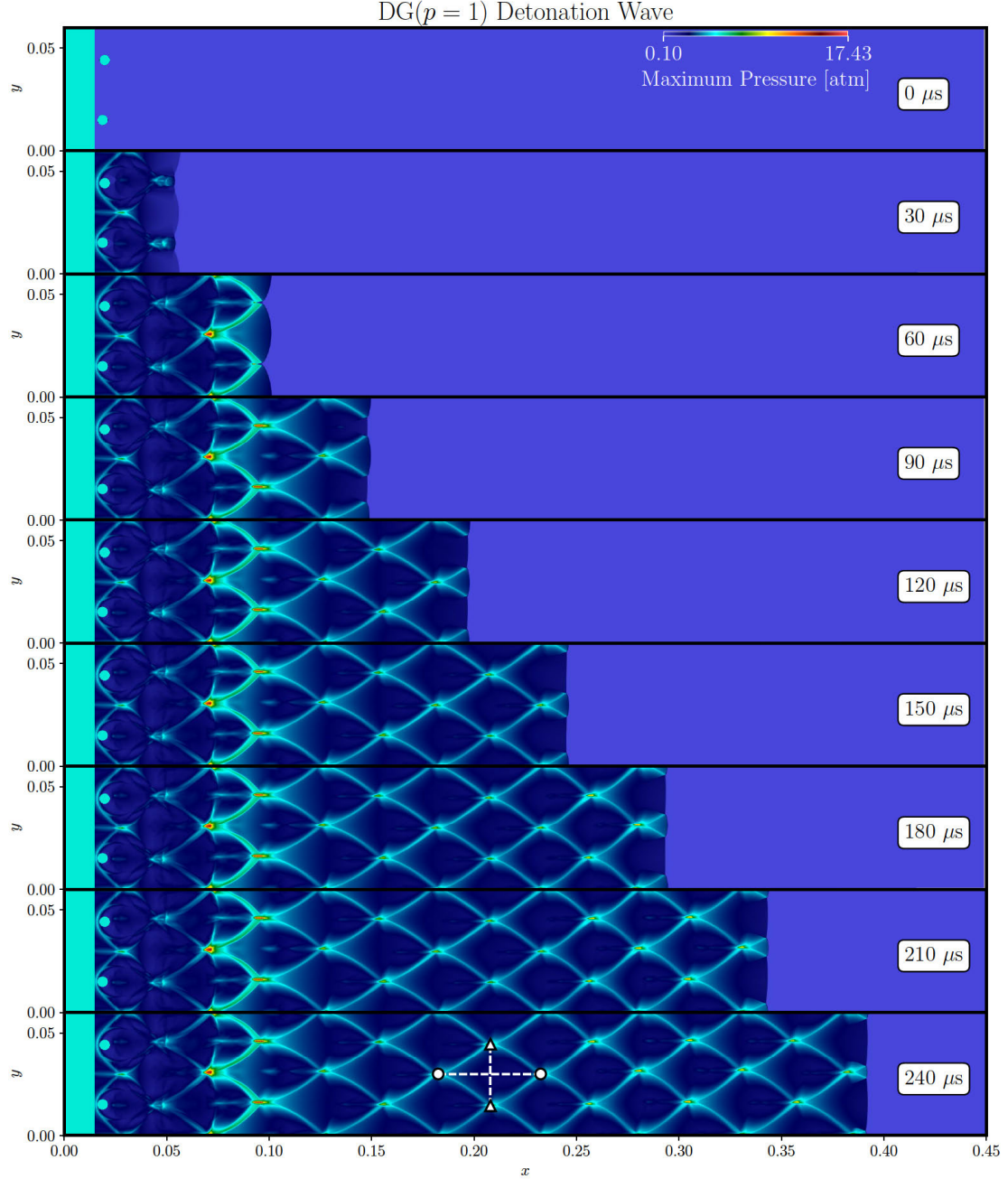


Figure 5.11: Maximum pressure, $\max(p, p_{max})$, revealing two distinct detonation cellular structure, cf. [30] and [75].

No spurious pressure oscillations were noticed for the entire simulation of this test case, indicating that the formulation presented in this work is stable for two-dimensional detonations. For this test case, the integrated

total energy, $\int_{\Omega} (\rho e_t)_0 d\Omega$, and the density, $\int_{\Omega} (\rho)_0 d\Omega$, are conserved as the domain has walls at all boundaries. Figure 5.12 shows the percent loss of the integrated total energy, $(\int_{\Omega} (\rho e)_0 d\Omega - \int_{\Omega} (\rho e)_t d\Omega) / \int_{\Omega} (\rho e)_0 d\Omega \times 100$, as well as the percent loss of the integrated density, $(\int_{\Omega} (\rho)_0 d\Omega - \int_{\Omega} (\rho)_t d\Omega) / \int_{\Omega} (\rho)_0 d\Omega \times 100$, as a function of time. The error remains on the order of 10^{-13} % for the entire simulation which is on the order of the expected machine error and assures that the method remains conservative.

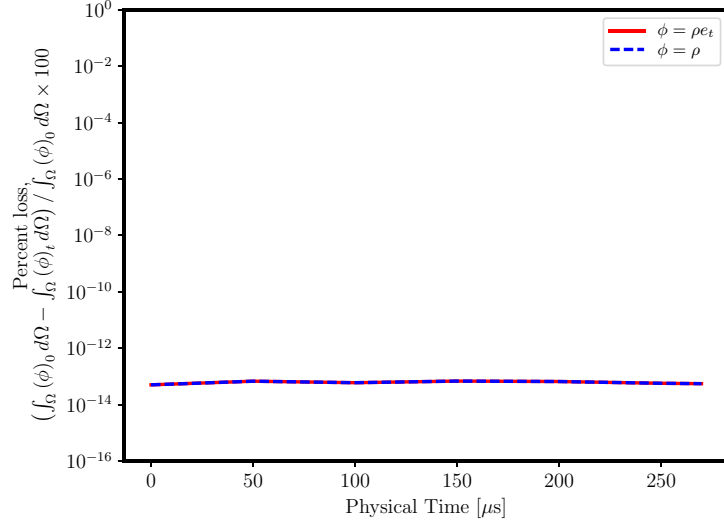


Figure 5.12: Percent loss of conservation quantities, $(\int_{\Omega} (\phi)_0 - \int_{\Omega} (\phi)_t) / \int_{\Omega} (\phi)_0 \times 100$, for the two-dimensional detonation computed using the initial integrated quantity, $\int_{\Omega} (\phi)_0 d\Omega$, and current integrated quantity, $\int_{\Omega} (\phi)_t d\Omega$, where $\phi = \rho e_t$ for total energy and $\phi = \rho$ for density.

5.5. One-dimensional premixed flame

In this section we consider a fully compressible multi-component reacting Navier-Stokes flow corresponding to a one-dimensional premixed flame using the Hydrogen-Air chemistry from [76]. The chosen domain is 6 cm in length and discretized with uniform linear line elements with $h = 5 \times 10^{-5}$ m. The initialization is given by

$$(p, T, X_{O_2}, X_{H_2}, X_{N_2}) = (1 \text{ bar}, 300 \text{ K}, 0.170, 0.188, 0.642) \quad x < 5.8 \text{ cm} \\ y = \hat{y} \quad x > 5.8 \text{ cm}, \quad (5.5)$$

where \hat{y} corresponds to the fully reacted state from Cantera's homogeneous constant pressure reactor simulation calculated from the unreacted conditions specified at $x < 5.8$ cm [66]. The solution at the initially discontinuous interface immediately diffuses to form a continuous, smooth, solution. No additional stabilization, e.g., artificial viscosity, limiting or filtering was needed for the duration of the simulation.

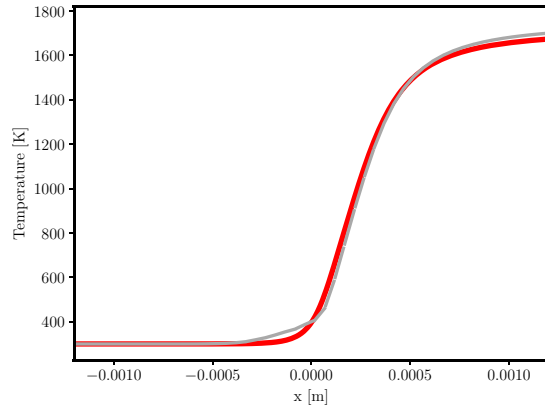
The right hand side boundary is a fixed pressure outflow characteristic boundary condition with $p_{\infty} = 1$ bar. The left hand side boundary is a characteristic farfield wave boundary condition with $T_{\infty} = 300$ K and $v_{\infty} = 0$ m/s. This boundary allows any pressure waves caused by the initialization to exit the domain. The initialization contains a temperature and species discontinuity which gives rise to a pressure wave that leaves the system as the reaction front diffuses into the unreacted region. Eventually, the solution converges to a propagating flame traveling at a unique velocity.

Table 3: Computed flame speeds corresponding to the one-dimensional premixed flame described in Section 5.5.

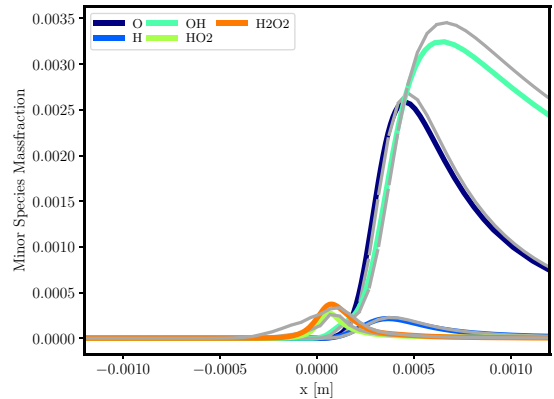
Method	Flame Speed [m/s]
Cantera	0.643
DG ($p = 1$)	0.641
DG ($p = 2$)	0.643

Figures 5.13 and 5.14 present the DG ($p = 1$) and DG ($p = 2$) solutions, respectively. The temperature and species mass fraction profiles are compared to the Cantera flame solution with $h = 10^{-5}$ m and the profiles are shifted so that $T = 400$ K at $x = 0$ m. The DG ($p = 1$) solutions reach the correct reacted state but cannot fully resolve the flame structures in the $-0.0005 < x < 0$ region. The DG ($p = 2$) solution overcomes these errors and is in good agreement with the Cantera solution. Despite the under resolved profiles in the DG ($p = 1$) solution, the flame speeds corresponding to both solutions compare well to the flame speed calculated in Cantera as presented in Table 3. The Cantera flame speed, given as the inflow velocity for the constant mass flow-rate, is 0.643 m/s. We considered the flame front in the unsteady DG ($p = 1$) and DG ($p = 2$) solutions to be the location corresponding to $T = 1000$ K. We tracked this location and computed a steady velocity of 0.641 m/s and 0.643 m/s for the DG ($p = 1$) and DG ($p = 2$) solutions, respectively.

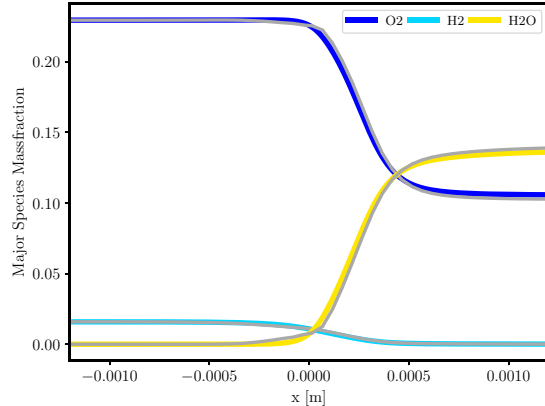
Figures 5.13d and 5.14d show the pressure through the entire computational domain for DG ($p = 1$) and DG ($p = 2$), respectively. For the DG ($p = 1$) solution, there are small oscillations, on the order of 0.25% of the ambient pressure. These oscillations are not present for the DG ($p = 2$) solution, where only a slight variation is seen through the flame front but is constant on both sides of the flame within 0.1% of the desired ambient pressure. The lack of pressure oscillations in the higher order solution indicate that the DG ($p = 1$) solution is under-resolved.



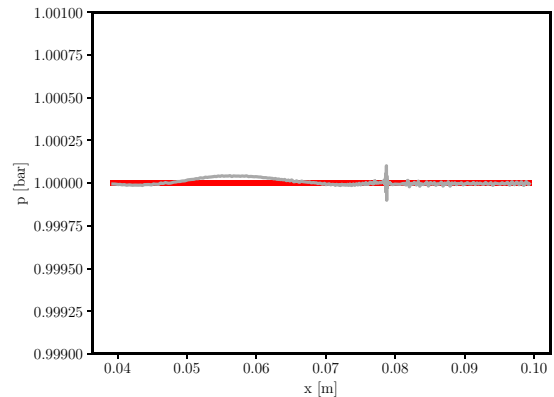
(a) The temperature profile correspond to the DG ($p = 1$) solution (grey lines) and the Cantera solution (solid lines) on a uniform $h = 5 \times 10^{-5}$ m grid. Both the DG ($p = 1$) and Cantera solutions have been shifted so that $T = 400$ K at $x = 0$.



(b) Minor species profiles correspond to the DG ($p = 1$) solution (grey lines) and the Cantera solution (solid lines) on a uniform $h = 5 \times 10^{-5}$ m grid. Both the DG ($p = 1$) and Cantera solutions have been shifted so that $T = 400$ K at $x = 0$.

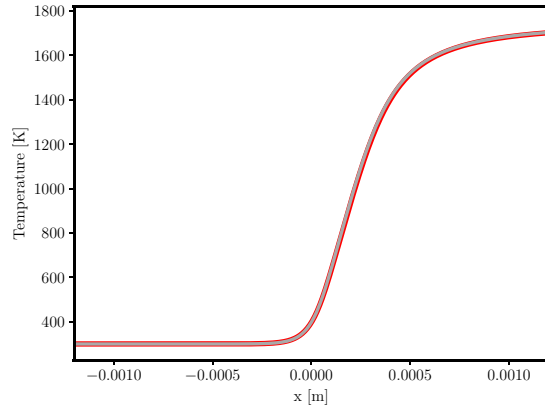


(c) Major species profiles correspond to the DG ($p = 1$) solution (grey lines) and the Cantera solution (solid lines) on a uniform $h = 5 \times 10^{-5}$ m grid. Both the DG ($p = 1$) and Cantera solutions have been shifted so that $T = 400$ K at $x = 0$.

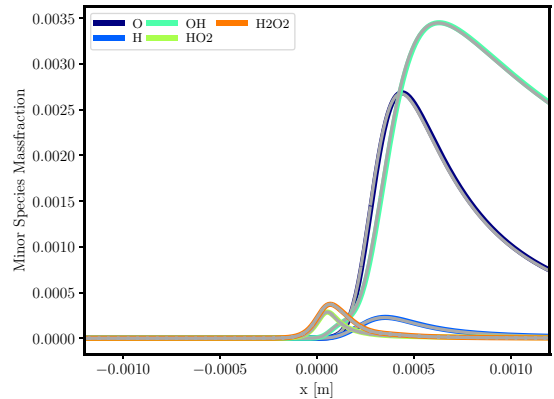


(d) The pressure profile corresponding to the DG ($p = 1$) solution (grey line) for the entire simulation domain. For reference the the pressure profile corresponding to a constant 1 bar solution is included (solid red line). The initialization is given by (5.5).

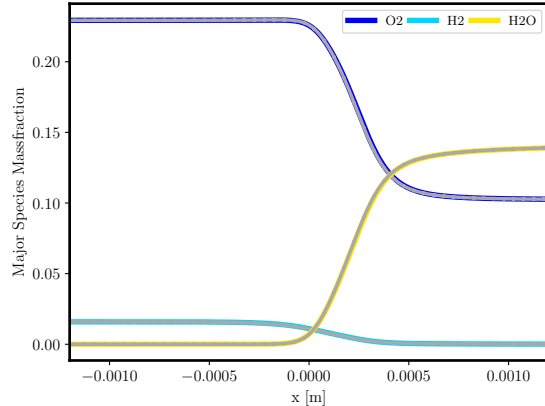
Figure 5.13: The profiles corresponding to the DG ($p = 1$) solution for the one-dimensional premixed flame, described in Section 5.5, computed on a uniform grid with on a uniform $h = 5 \times 10^{-5}$ m grid. The initialization is given by (5.3). The flame speed of 0.641 m/s corresponding to the DG ($p = 1$) solution compares well with the flame speed corresponding to the Cantera solution of 0.643 m/s. This smooth solution of a multi-component chemically reacting Navier-Stokes flow was computed without the use of additional stabilization, e.g., artificial viscosity, limiting or filtering. The pressure oscillations visible in Figure 5.13d are not present in the corresponding DG ($p = 2$) solution shown in Figure 5.14d, indicating the DG ($p = 1$) solution is under-resolved.



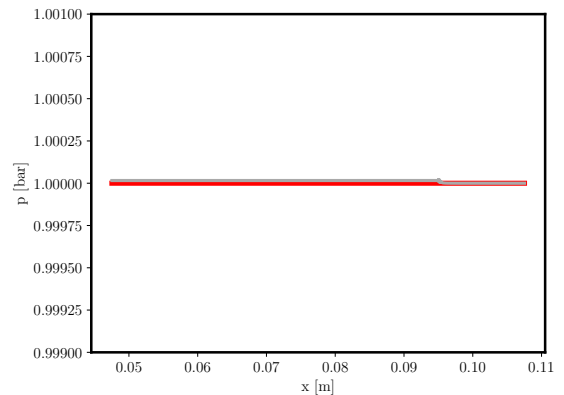
(a) The temperature profile correspond to the DG ($p = 2$) solution (grey lines) and the Cantera solution (solid lines) on a uniform $h = 5 \times 10^{-5}$ m grid. Both the DG ($p = 2$) and Cantera solutions have been shifted so that $T = 400$ K at $x = 0$.



(b) Minor species profiles correspond to the DG ($p = 2$) solution (grey lines) and the Cantera solution (solid lines) on a uniform $h = 5 \times 10^{-5}$ m grid. Both the DG ($p = 2$) and Cantera solutions have been shifted so that $T = 400$ K at $x = 0$.



(c) Major species profiles correspond to the DG ($p = 2$) solution (grey lines) and the Cantera solution (solid lines) on a uniform $h = 5 \times 10^{-5}$ m grid. Both the DG ($p = 2$) and Cantera solutions have been shifted so that $T = 400$ K at $x = 0$.



(d) The pressure profile corresponding to the DG ($p = 2$) solution (grey line) for the entire simulation domain. For reference the the pressure profile corresponding to a constant 1 bar solution is included (solid red line).

Figure 5.14: The profiles corresponding to the DG ($p = 2$) solution for the one-dimensional premixed flame, described in Section 5.5, computed on a uniform grid with on a uniform $h = 5 \times 10^{-5}$ m grid. The initialization is given by (5.3). The flame speed of 0.643 m/s corresponding to the DG ($p = 2$) solution compares well with the flame speed corresponding to the Cantera solution of 0.643 m/s. This smooth solution of a multi-component chemically reacting Navier-Stokes flow was computed without the use of additional stabilization, e.g., artificial viscosity, limiting or filtering.

5.6. Hydrogen-Air chemically reacting shear layer

We use the viscous reacting formulation of Equations (3.6)- (3.8) with detailed chemical kinetics and transport to approximate the solution of a chemically reacting shear layer using the Hydrogen-Air chemistry extracted from the GRI Mech II mechanism [76]. This test case was designed to test the stability and robustness of the formulation presented in this work and verify that smooth multidimensional multi-component reacting flows can be computed without artificial viscosity, limiting, or filtering. The entire simulation domain is depicted in Figure 5.15. The bounding domain is 0.10 m in length and 0.05 m in height, $\Omega = (0, 0.10) \text{ m} \times (0, 0.05) \text{ m}$. A splitter plate is used to separate the incoming streams, anchor the flame, and to test slip and adiabatic wall boundary conditions described in Section 3.1. The plate is 0.001 m

thick and 0.005 m long and is centered at $y = 0.025$ m. The flow is initialized with the following conditions

$$(M, T, p, Y_{O_2}, Y_{N_2}, Y_{H_2}) = \begin{cases} (0.8, 2000 \text{ K}, 101325 \text{ Pa}, 0.21, 0.79, 0) & y < 0.025 \text{ m} \\ (0.8, 2000 \text{ K}, 101325 \text{ Pa}, 0, 0, 1) & y > 0.025 \text{ m} \end{cases}, \quad (5.6)$$

where M is the freestream Mach number.

The upstream half of the plate, $0 \text{ m} < x < 0.0025 \text{ m}$, is specified as a slip wall, whereas the downstream half of the plate, $0.0025 \text{ m} < x < 0.005 \text{ m}$, is an adiabatic no-slip wall. The remaining boundaries, at $x = 0 \text{ m}$, $x = 0.1 \text{ m}$, $y = 0 \text{ m}$, and $y = 0.05 \text{ m}$, are specified as non-reflecting characteristic boundary conditions where the freestream state is given by (5.6). The characteristic conditions downstream of the plate at $x = 0.1 \text{ m}$ allow for pockets of supersonic flow to exit the domain if the heat release from reactions is large enough to transition the flow to supersonic.

Initial simulations were run to determine the regions of refinement required to adequately capture the reacting mixing layer. Figure 5.15 presents the final grid corresponding to the entire domain, which was constructed using Gmsh [77]. The finest resolution in the mixing region corresponds to a mesh size of $200 \times 10^{-6} \text{ m}$ and transitions to $500 \times 10^{-6} \text{ m}$ at $x = 0.1 \text{ m}$. This region begins at a thickness of 0.0035 m, $0.02325 \text{ m} < y < 0.02675 \text{ m}$, at $x = 0 \text{ m}$, and grows to a thickness of 0.015 m, $0.0155 \text{ m} < y < 0.0355 \text{ m}$, at $x = 0.1 \text{ m}$.

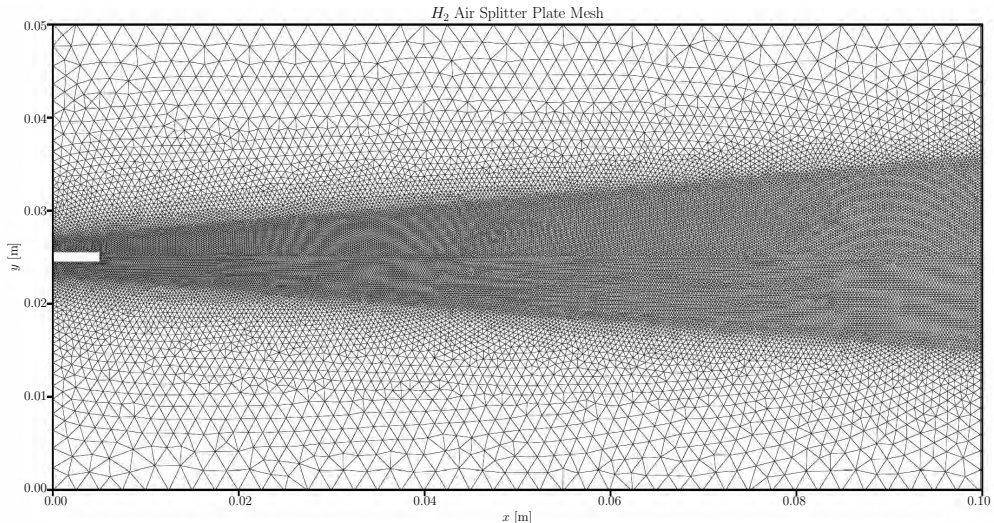
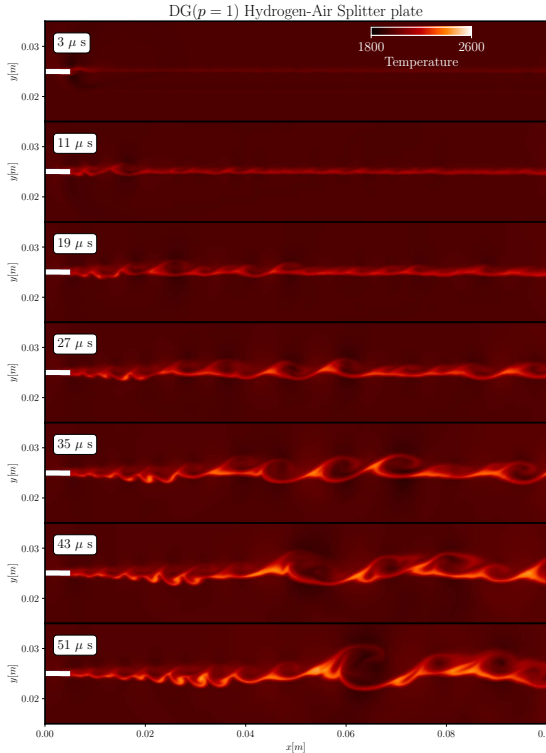
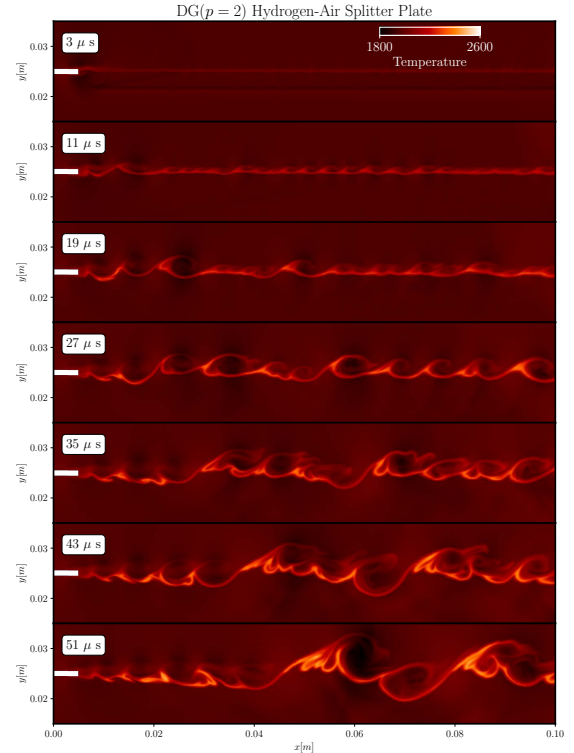


Figure 5.15: Splitter plate mesh comprised of linear triangular elements with increased resolution mixing region. This mesh was generated using Gmsh [77].

Figures 5.16a and 5.16b show the temporal evolution for $\text{DG}(p = 1)$ and $\text{DG}(p = 2)$ temperature solutions, respectively. The initial interface between H₂ and air diffuses and reactions occur along the mid-line. As the reactions progress, flow features develop that create mixing structures that grow in the downstream direction. As the $\text{DG}(p = 1)$ and $\text{DG}(p = 2)$ solutions evolve in time, they begin to diverge from each other. Figure 5.17 shows a direct comparison of the solutions at $t = 51 \mu\text{s}$. The profiles for the $\text{DG}(p = 2)$ solution are thinner and less diffuse than the $\text{DG}(p = 1)$ solution which contributes to the difference in the downstream features. Figures 5.18a and 5.18b show the upstream and downstream Y_{H_2O} profiles, respectively, for both the $\text{DG}(p = 1)$ and $\text{DG}(p = 2)$ at $t = 51 \mu\text{s}$. The $\text{DG}(p = 2)$ solution resolves a sharper flame attachment to the splitter wall than the $\text{DG}(p = 1)$ solution. In the downstream region a large structure is apparent in both solutions, with the $\text{DG}(p = 2)$ solution resolving more fine scale features than the $\text{DG}(p = 1)$ solution.



(a) Evolution of temperature profile using DG ($p = 1$) for H2-air splitter plate.



(b) Evolution of temperature profile using DG ($p = 2$) for H2-air splitter plate.

Figure 5.16: Evolution of temperature profile corresponding to the DG ($p = 1$) and DG ($p = 2$) solutions at different times. The initialization is given by (5.6). This smooth solution of a multi-component chemically reacting Navier-Stokes flow was computed without the use of additional stabilization, e.g., artificial viscosity, limiting or filtering.

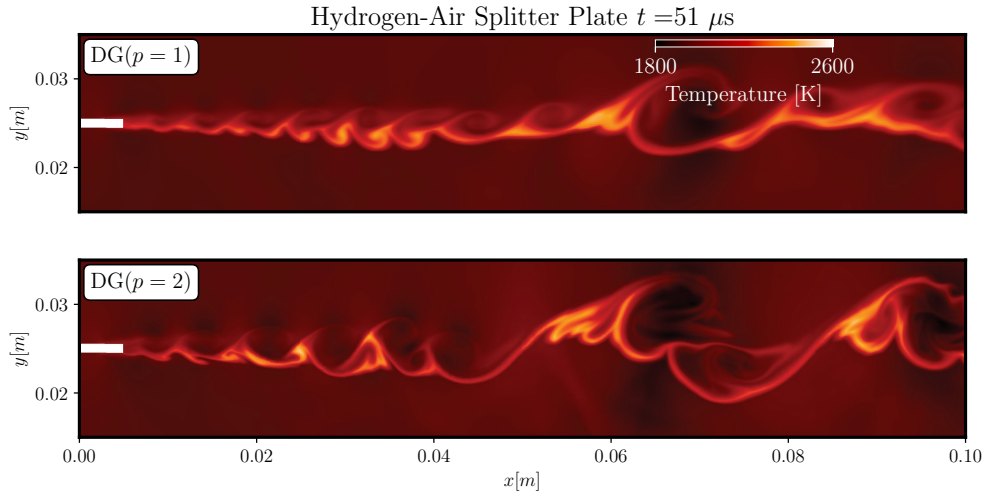
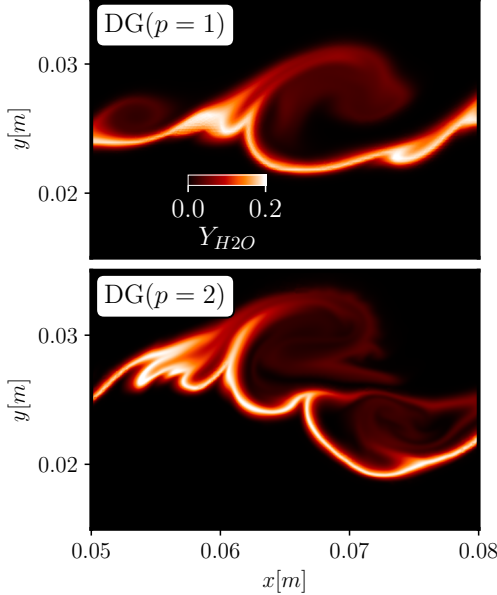


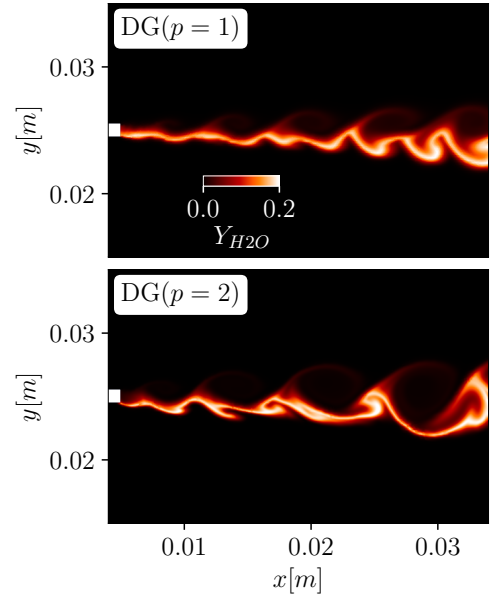
Figure 5.17: Comparison of splitter plate temperature solution for DG ($p = 1$) and DG ($p = 2$) at $t = 51 \mu s$.

Hydrogen-Air Splitter Plate $t = 51 \mu\text{s}$



(a) Upstream structures of H_2O for DG ($p = 1$) and DG ($p = 2$) at $t = 51 \mu\text{s}$.

Hydrogen-Air Splitter Plate $t = 51 \mu\text{s}$



(b) Downstream structures of H_2O for DG ($p = 1$) and DG ($p = 2$) at $t = 51 \mu\text{s}$.

Figure 5.18: Comparison of splitter plate H_2O mass fraction solution for DG ($p = 1$) and DG ($p = 2$) at $t = 51 \mu\text{s}$. The initialization is given by (5.6). This smooth solution of a multi-component chemically reacting Navier-Stokes flow was computed without the use of additional stabilization, e.g., artificial viscosity, limiting or filtering.

We extended this two-dimensional shear layer problem to three dimensions by extruding the mesh in the z -direction. To save on computational cost, the domain was changed to 0.03 m in height but maintained a length of 0.10 m, $\Omega = (0, 0.10) \text{ m} \times (0, 0.03) \text{ m}$. The splitter plate is the same size but is centered at $y = 0.015$ m. The mixing region resolution and size is the same as the two dimensional problem but shifted to center the new plate location. The mesh was constructed using Gmsh and was extruded in the z -direction at a cellular width of 200×10^{-6} m for a total width of 0.0028 m. The boundary conditions in the resulting xz -planes and yz -planes were the same as the two dimensional splitter plate shifted to be centered at $y = 0.015$ m for the left hand side boundary with the exception of a spatiotemporal variation introduced to the momentum at the $x = 0$ boundaries,

$$\begin{aligned}
 M &= 0.8, \\
 v_1 &= Mc + \frac{M}{10}c \sin\left(\frac{\pi}{w}z\right) \sin\left(\frac{2\pi}{\tau}t\right) & \text{m/s,} \\
 v_2 &= 0 & \text{m/s,} \\
 v_3 &= \frac{M}{5}c + \frac{M}{50}c \sin\left(\frac{\pi}{w}z\right) \sin\left(\frac{2\pi}{\tau}t\right) & \text{m/s,}
 \end{aligned} \tag{5.7}$$

where $c = \sqrt{\gamma RT}$ with γ and R calculated from the mixture properties at the boundary. This inflow boundary condition was used to encourage three-dimensional breakup and unsteadiness in the z -direction. Periodicity is enforced between the resulting xy -planes at $z = 0$ m and $z = 0.0028$ m. The initialization is the same as in two dimensional case, which is given by (5.6) at time $t = 0$ s. The DG($p = 1$) approximation was used for the first 100 μs of the simulation, at which point the approximate solution was interpolated to the space corresponding to the DG($p = 2$) approximation. No artificial viscosity, limiting, or filtering was required throughout the entire simulation as the physical diffusion present in the solution provided adequate stabilization.

Figure 5.19 shows the Y_{H_2O} solution for xy -planes located at $z = 0$ m and $z = 0.0014$ m. The variation of Y_{H_2O} in the z -direction is greater downstream of $x = 0.04$ m. This is seen particularly in the solution

for $y > 0$, where the flow-field inertia is not as great since the species has less mass and is therefore more susceptible to mixing due to the inflow perturbations. Figure 5.20 shows the three dimensional isocontours for $T = 2200$ K between times $t = 350$ and $t = 370 \mu\text{s}$. The splitter plate is shown as a black surfaces, where as the isocontours are colored by the absolute value of the z -component of the isocontour surface normal, labeled as $|n_z|$. Red and white surfaces represent areas where the flame is wrinkled in the z -direction, whereas blue surfaces represent areas of the flame that are planar in the z -direction, $|n_z| \rightarrow 0$. These isocontours confirm that the flame becomes less uniform in the z -direction in the region downstream of $x = 0.04$ m, particularly in the top half of the domain, $y > 0.015$ m.

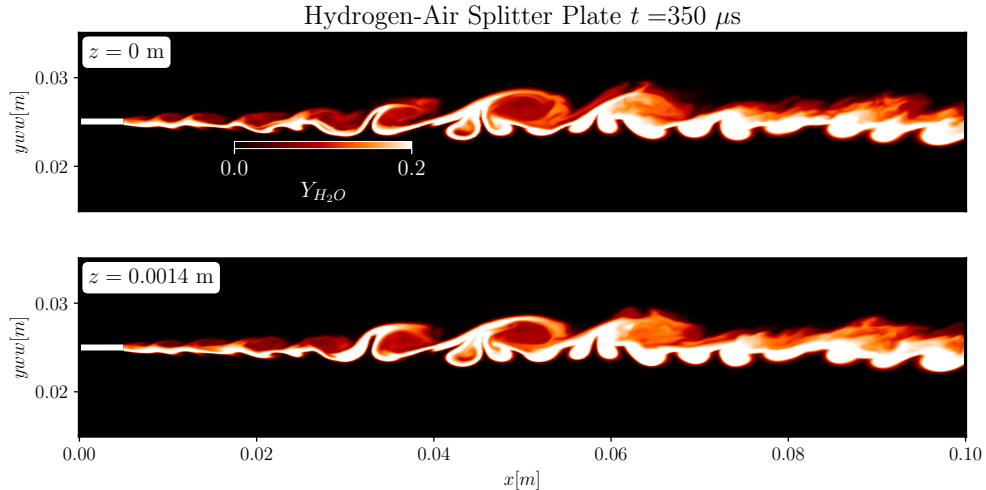


Figure 5.19: Three dimensional DG ($p = 2$) splitter plate Y_{H_2O} xy-plane solutions at two different z -locations at $t = 350 \mu\text{s}$. This smooth solution of a multi-component chemically reacting Navier-Stokes flow was computed without the use of additional stabilization, e.g., artificial viscosity, limiting or filtering.

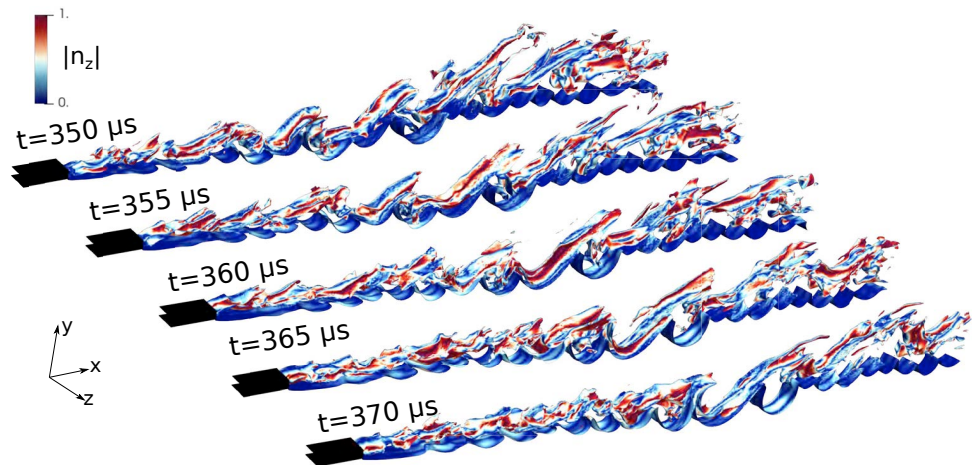


Figure 5.20: Three dimensional DG ($p = 2$) splitter plate $T = 2200$ K isocontour solution from $t = 350$ to $t = 370 \mu\text{s}$. This smooth solution of a multi-component chemically reacting Navier-Stokes flow was computed without the use of additional stabilization, e.g., artificial viscosity, limiting or filtering.

These results indicate that the conservative DG formulation presented in this work is capable of computing smooth multidimensional, multi-component, chemically reacting Navier-Stokes flows without the need

for artificial viscosity, limiting, filtering. Furthermore, since the formulation maintains discrete temperature and pressure equilibrium it is capable of incorporating the viscous and diffusive operators without caveats or creating additional concerns. As expected, the formulation behaves exactly like its single-component counterpart for the case of viscous multi-component reacting flows.

6. Conclusion

We have presented a a fully conservative discontinuous Galerkin finite element method for the multi-component chemically reacting Navier-Stokes equations that retains the desirable properties of DG, namely discrete conservation and high-order accuracy in smooth regions of the flow. In contrast to previous DG implementations for multi-component chemically reacting flows, the formulation presented in this work does not freeze the thermodynamics; instead a nonlinear relationship for temperature is solved which ensures consistency between the internal energy of the conserved state and the internal energy defined by a mixture averaged polynomial expression based on temperature. Furthermore, the discrete solution is represented in terms of a nodal basis with coefficients defined on the element interfaces so that temperature and pressure equilibrium between adjacent elements is maintained and the resulting weak form is evaluated in terms of basis coefficients that are designed to maintain pressure equilibrium. As such, unphysical pressure oscillations are not generated at material interfaces if the temperature is continuous. Furthermore, if the temperature is discontinuous, the unphysical pressure oscillations remain small and do not lead to numerical failure. Other numerical instabilities do arise at discontinuous interfaces, e.g., shocks and detonations, but these are not specific to multi-component flows and they are suppressed in this work by the addition of a residual based artificial viscosity.

A coupled hp -adaptive ODE solver, DGODE, has been developed for the integration of the stiff chemical source term. The solver adapts the local time-step, h , as well as the polynomial degree, p , corresponding to the local approximation in order to efficiently integrate the system of ODEs. The solver was shown to successfully integrate the stiff source term corresponding to the one- and two-dimensional H_2-O_2-Ar detonation waves, where the local polynomial degree adapted to the local stiffness of the chemical system.

The generation of unphysical pressure oscillations was studied in the context of the formulation described in this work. We found that pressure oscillations generated for formulations based on frozen thermodynamics did not reach the magnitudes previously reported in literature [25, 26, 15, 27, 16]. However, when it was assumed that the mean specific heat at constant pressure was the same as the NASA polynomial specific heat at constant pressure, $\bar{c}_p = c_p$, the oscillations did reach the same levels as previously reported, indicating that the severity of the pressure oscillations is directly related to the method in which the thermodynamic quantities are evaluated. Regardless, frozen thermodynamic formulations generate pressure oscillations that grow in time as the solution evolves. In contrast, evaluating the thermodynamics quantities exactly does not lead to pressure oscillations at a material interface if the temperature is continuous. We therefore concluded that the conservative DG discretization presented in this work can stably compute solutions to smooth multi-component chemically reacting Navier-Stokes flows without additional stabilization.

The discretization was applied to several multi-component non-reacting and reacting test cases including: a one-dimensional He and N_2 shock-tube, a two dimension shock interaction with a helium bubble suspended in air, one-dimensional H_2-O_2-Ar detonation wave, and two-dimensional H_2-O_2-Ar detonation. We confirmed that additional stabilization is not required for well-resolved smooth regions of the flow. Where applicable, i.e., for wall-bounded problems, we computed the integrated percent loss of the conserved quantities at each time-step. The value was shown to be on the order of machine error while remaining constant for the duration of the simulation. The solutions for the one- and two-dimensional H_2-O_2-Ar detonation simulations were compared to results previously reported in the literature. The profile of the one-dimensional solution in the region of the detonation was shown to be in close agreement with the profile predicted by the detonation toolbox and two-dimensional solution was shown to reproduce the correct cellular detonation structure.

We also presented a one-dimensional premixed hydrogen-air flame and two- and three-dimensional reacting shear layer with a splitter plate. The H_2 -air deflagration flame speed compared well to the speed computed via Cantera for both the $DG(p=1)$ and $DG(p=2)$ solutions. Discrepancies between the Cantera

solution and the $DG(p = 1)$ solution were not observed in the $DG(p = 2)$ solution, indicating the $DG(p = 2)$ solution better resolved the flame. The two- and three-dimensional shear layer simulations confirmed, in a practical setting, that the conservative DG formulation does not require additional stabilization for smooth multi-component chemically reacting Navier-Stokes flows.

Acknowledgements

This work is sponsored by the Office of Naval Research through the Naval Research Laboratory 6.1 Computational Physics Task Area.

References

- [1] R. Johnson, A. Kercher, A conservative discontinuous Galerkin discretization for the total energy formulation of the reacting Navier Stokes equations, arXiv preprint arXiv:1910.10544.
- [2] W. H. Reed, T. Hill, Triangular mesh methods for the neutron transport equation, Tech. rep., Los Alamos Scientific Lab., N. Mex.(USA) (1973).
- [3] F. Bassi, S. Rebay, A high-order accurate discontinuous finite element method for the numerical solution of the compressible Navier-Stokes equations, *Journal of Computational Physics* 131 (2) (1997) 267–279.
- [4] F. Bassi, S. Rebay, High-order accurate discontinuous finite element solution of the 2D Euler equations, *Journal of Computational Physics* 138 (2) (1997) 251–285.
- [5] B. Cockburn, C.-W. Shu, The Runge–Kutta discontinuous Galerkin method for conservation laws V: multidimensional systems, *Journal of Computational Physics* 141 (2) (1998) 199–224.
- [6] B. Cockburn, G. Karniadakis, C.-W. Shu, The development of discontinuous Galerkin methods, in: *Discontinuous Galerkin Methods*, Springer, 2000, pp. 3–50.
- [7] D. Arnold, F. Brezzi, B. Cockburn, L. Marini, Unified analysis of discontinuous Galerkin methods for elliptic problems, *SIAM Journal on Numerical Analysis* 39 (5) (2002) 1749–1779.
- [8] R. Hartmann, P. Houston, Adaptive discontinuous Galerkin finite element methods for the compressible Euler equations, *Journal of Computational Physics* 183 (2) (2002) 508–532.
- [9] K. Fidkowski, T. Oliver, J. Lu, D. Darmofal, p-Multigrid solution of high-order discontinuous Galerkin discretizations of the compressible Navier–Stokes equations, *Journal of Computational Physics* 207 (1) (2005) 92–113.
- [10] H. Luo, J. Baum, R. Löhner, A p-multigrid discontinuous Galerkin method for the euler equations on unstructured grids, *Journal of Computational Physics* 211 (2) (2006) 767–783.
- [11] H. Luo, J. Baum, R. Löhner, A hermite weno-based limiter for discontinuous Galerkin method on unstructured grids, *Journal of Computational Physics* 225 (1) (2007) 686–713.
- [12] H. Luo, J. Baum, R. Löhner, A discontinuous Galerkin method based on a taylor basis for the compressible flows on arbitrary grids, *Journal of Computational Physics* 227 (20) (2008) 8875–8893.
- [13] P.-O. Persson, J. Peraire, Newton-GMRES preconditioning for discontinuous Galerkin discretizations of the Navier–Stokes equations, *SIAM Journal on Scientific Computing* 30 (6) (2008) 2709–2733.
- [14] R. Hartmann, T. Leicht, Higher order and adaptive DG methods for compressible flows, in: H. Deconinck (Ed.), *VKI LS 2014-03: 37th Advanced VKI CFD Lecture Series: Recent developments in higher order methods and industrial application in aeronautics*, Dec. 9-12, 2013, Von Karman Institute for Fluid Dynamics, Rhode Saint Genèse, Belgium, 2014.
- [15] G. Billet, J. Ryan, A Runge–Kutta discontinuous Galerkin approach to solve reactive flows: The hyperbolic operator, *Journal of Computational Physics* 230 (4) (2011) 1064 – 1083. doi:<https://doi.org/10.1016/j.jcp.2010.10.025>.
- [16] Y. Lv, M. Ihme, Discontinuous Galerkin method for multicomponent chemically reacting flows and combustion, *Journal of Computational Physics* 270 (2014) 105 – 137. doi:<https://doi.org/10.1016/j.jcp.2014.03.029>.
- [17] G. P. Smith, D. M. Golden, M. Frenklach, N. W. Moriarty, B. Eiteneer, M. Goldenberg, C. T. Bowman, Gri-mech 3.0, version 3.0 (2000).
- [18] R. Abgrall, Generalisation of the Roe scheme for the computation of mixture of perfect gases, *La Recherche Aérospatiale* 6 (1988) 31–43.
- [19] S. Karni, Multicomponent flow calculations by a consistent primitive algorithm, *Journal of Computational Physics* 112 (1) (1994) 31 – 43. doi:<https://doi.org/10.1006/jcph.1994.1080>.
- [20] R. Abgrall, How to prevent pressure oscillations in multicomponent flow calculations: A quasi conservative approach, *Journal of Computational Physics* 125 (1) (1996) 150 – 160. doi:<https://doi.org/10.1006/jcph.1996.0085>.
- [21] P. Jenny, B. Mueller, H. Thomann, Correction of conservative euler solvers for gas mixtures, *Journal of Computational Physics* 132 (1) (1997) 91 – 107. doi:<https://doi.org/10.1006/jcph.1996.5625>.
- [22] M. Zahr, P.-O. Persson, An optimization-based approach for high-order accurate discretization of conservation laws with discontinuous solutions, *Journal of Computational Physics*.
- [23] A. Corrigan, A. Kercher, D. Kessler, A moving discontinuous Galerkin finite element method for flows with interfaces, *International Journal for Numerical Methods in Fluids* 89 (9) (2019) 362–406. doi:[10.1002/fld.4697](https://doi.org/10.1002/fld.4697).

[24] Z. Sun, M. Braack, J. Lang, An adaptive moving finite element method for steady low mach number compressible combustion problems, *International Journal for Numerical Methods in Fluids* n/a (n/a). doi:[10.1002/fld.4818](https://doi.org/10.1002/fld.4818).

[25] R. Abgrall, S. Karni, Computations of compressible multifluids, *Journal of Computational Physics* 169 (2) (2001) 594 – 623. doi:<https://doi.org/10.1006/jcph.2000.6685>.

[26] G. Billet, R. Abgrall, An adaptive shock-capturing algorithm for solving unsteady reactive flows, *Computers and Fluids* 32 (10) (2003) 1473 – 1495. doi:[https://doi.org/10.1016/S0045-7930\(03\)00004-5](https://doi.org/10.1016/S0045-7930(03)00004-5).

[27] R. Houim, K. Kuo, A low-dissipation and time-accurate method for compressible multi-component flow with variable specific heat ratios, *Journal of Computational Physics* 230 (23) (2011) 8527 – 8553. doi:<https://doi.org/10.1016/j.jcp.2011.07.031>.

[28] E. Johnsen, F. Ham, Preventing numerical errors generated by interface-capturing schemes in compressible multi-material flows, *Journal of Computational Physics* 231 (17) (2012) 5705 – 5717. doi:<https://doi.org/10.1016/j.jcp.2012.04.048>.

[29] B. Thornber, M. Groom, D. Youngs, A five-equation model for the simulation of miscible and viscous compressible fluids, *Journal of Computational Physics* 372 (2018) 256 – 280. doi:<https://doi.org/10.1016/j.jcp.2018.06.028>.

[30] E. S. Oran, E. I. Weber J. W. and Stefaniw, M. H. Lefebvre, J. D. Anderson, A numerical study of a two-dimensional h2-o2-ar detonation using a detailed chemical reaction model, *Combustion and Flame* 113 (1) (1998) 147 – 163. doi:[https://doi.org/10.1016/S0010-2180\(97\)00218-6](https://doi.org/10.1016/S0010-2180(97)00218-6).

[31] E. S. Oran, J. P. Boris, *Numerical Simulation of Reactive Flow*, 2nd Edition, Cambridge University Press, 2000. doi:[10.1017/CBO9780511574474](https://doi.org/10.1017/CBO9780511574474).

[32] J. B. Chen, H. G. Im, Stretch effects on the burning velocity of turbulent premixed hydrogen/air flames, *Proceedings of the Combustion Institute* 28 (1) (2000) 211 – 218. doi:[https://doi.org/10.1016/S0082-0784\(00\)80213-1](https://doi.org/10.1016/S0082-0784(00)80213-1).

[33] E. R. Hawkes, R. Sankaran, S. J. C., J. H. Chen, Direct numerical simulation of turbulent combustion: fundamental insights towards predictive models, *Journal of Physics: Conference Series* 16 (2005) 65–79. doi:[10.1088/1742-6596/16/1/009](https://doi.org/10.1088/1742-6596/16/1/009).

[34] B. D. Taylor, D. A. Kessler, V. N. Gamezo, E. S. Oran, Numerical simulations of hydrogen detonations with detailed chemical kinetics, *Proceedings of the Combustion Institute* 34 (2) (2013) 2009 – 2016. doi:<https://doi.org/10.1016/j.proci.2012.05.045>.

[35] B. Taylor, D. Schwer, A. Corrigan, Implementation of thermochemistry and chemical kinetics in a GPU-based CFD code, in: 53rd AIAA Aerospace Sciences Meeting Including The New Horizons Forum and Aerospace Exposition, 2015, 2015-0842.

[36] C. A. Kennedy, M. H. Carpenter, Several new numerical methods for compressible shear-layer simulations, *Applied Numerical Mathematics* 14 (4) (1994) 397 – 433. doi:[https://doi.org/10.1016/0168-9274\(94\)00004-2](https://doi.org/10.1016/0168-9274(94)00004-2).

[37] R. Deiterding, Parallel adaptive simulation of multi-dimensional detonation structures, *Dissertation. de*, 2003.

[38] A. Y. Poludnenko, B. D. Taylor, Turbulent chemical and thermonuclear flames: Intrinsic instability and anisotropic turbulence amplification, in: *TSFP DIGITAL LIBRARY ONLINE*, Begel House Inc., 2015.

[39] P. Colella, P. Woodward, The piecewise parabolic method (PPM) for gas-dynamical simulations, *Journal of Computational Physics* 54 (1) (1984) 174–201.

[40] B. J. McBride, M. J. Zehe, S. Gordon, NASA Glenn coefficients for calculating thermodynamic properties of individual species.

[41] R. J. Kee, J. A. Miller, G. H. Evans, G. Dixon-Lewis, A computational model of the structure and extinction of strained, opposed flow, premixed methane-air flames, *Symposium (International) on Combustion* 22 (1) (1989) 1479 – 1494. doi:[https://doi.org/10.1016/S0082-0784\(89\)80158-4](https://doi.org/10.1016/S0082-0784(89)80158-4).

[42] C. R. Wilke, A viscosity equation for gas mixtures, *J. Chem. Phys* 18 (1950) 517–519. doi:[10.1063/1.1747673](https://doi.org/10.1063/1.1747673).

[43] S. Mathur, P. K. Tondon, S. C. Saxena, Thermal conductivity of binary, ternary and quaternary mixtures of rare gases, *Molecular Physics* 12 (1967) 569–579. doi:[10.1080/00268976700100731](https://doi.org/10.1080/00268976700100731).

[44] R. Kee, F. Rupley, J. Miller, *Chemkin-ii*: A Fortran chemical kinetics package for the analysis of gas-phase chemical kinetics.

[45] T. J. Poinsot, S. K. Lele, Boundary conditions for direct simulations of compressible viscous flows, *Journal of Computational Physics* 101 (1) (1992) 104 – 129. doi:[https://doi.org/10.1016/0021-9991\(92\)90046-2](https://doi.org/10.1016/0021-9991(92)90046-2).

[46] J. D. Anderson, *Hypersonic and High Temperature Gas Dynamics*, McGraw-Hill series in aeronautical and aerospace engineering, American Institute of Aeronautics and Astronautics, 2000.

[47] A. Corrigan, D. Williams, A. Kercher, Weak formulation of a conservation law in reference space, *Tech. rep.*, U.S. Naval Research Laboratory (March 2020).

[48] A. Kercher, A. Corrigan, D. Kessler, The moving discontinuous Galerkin finite element method with interface condition enforcement for compressible viscous flows, *arXiv preprint arXiv:2002.12740* <https://arxiv.org/pdf/2002.12740.pdf>.

[49] E. Toro, *Riemann solvers and numerical methods for fluid dynamics: a practical introduction*, Springer Science & Business Media, 2013.

[50] F. Bassi, S. Rebay, An implicit high-order discontinuous Galerkin method for the steady state compressible Navier-Stokes equations, *Computational fluid dynamics'98* (1998) 1226–1233.

[51] F. Bassi, S. Rebay, GMRES discontinuous Galerkin solution of the compressible Navier-Stokes equations, in: *Discontinuous Galerkin Methods*, Springer, 2000, pp. 197–208.

[52] F. Bassi, S. Rebay, Numerical evaluation of two discontinuous galerkin methods for the compressible navier–stokes equations, *International journal for numerical methods in fluids* 40 (1-2) (2002) 197–207.

[53] S. Gottlieb, C. Shu, E. Tadmor, Strong stability-preserving high-order time discretization methods, *SIAM review* 43 (1) (2001) 89–112.

[54] R. Spiteri, S. Ruuth, A new class of optimal high-order strong-stability-preserving time discretization methods, *SIAM Journal on Numerical Analysis* 40 (2) (2002) 469–491.

[55] Q. Zhang, C.-W. Shu, Error estimates to smooth solutions of Runge–Kutta discontinuous Galerkin methods for scalar conservation laws, *SIAM Journal on Numerical Analysis* 42 (2) (2004) 641–666.

[56] G. Strang, On the construction and comparison of difference schemes, *SIAM Journal on Numerical Analysis* 5 (3) (1968) 506–517.

[57] H. Atkins, C. Shu, Quadrature-free implementation of discontinuous galerkin methods for hyperbolic equations, ICASE Report 96-51, 1996, Tech. rep., NASA Langley Research Center, nASA-CR-201594 (August 1996).

[58] H. L. Atkins, C.-W. Shu, Quadrature-free implementation of discontinuous Galerkin method for hyperbolic equations, *AIAA journal* 36 (5) (1998) 775–782.

[59] T. Johnsen, T. Colonius, Implementation of WENO schemes in compressible multicomponent flow problems, *Journal of Computational Physics* 219 (2) (2006) 715 – 732. doi:<https://doi.org/10.1016/j.jcp.2006.04.018>.

[60] E. Johnsen, On the treatment of contact discontinuities using WENO schemes, *Journal of Computational Physics* 230 (24) (2011) 8665 – 8668. doi:<https://doi.org/10.1016/j.jcp.2011.08.017>.

[61] E. Ching, Y. Lv, P. Gnoffo, M. Barnhardt, M. Ihme, Shock capturing for discontinuous Galerkin methods with application to predicting heat transfer in hypersonic flows, *Journal of Computational Physics* 376 (2019) 54–75.

[62] P.-O. Persson, J. Peraire, Sub-cell shock capturing for discontinuous Galerkin methods, in: AIAA (Ed.), 44th AIAA Aerospace Sciences Meeting and Exhibit, 2006, AIAA-2006-112. doi:[10.2514/6.2006-112](https://doi.org/10.2514/6.2006-112).

[63] R. Bauer, Discontinuous galerkin methods for ordinary differential equations, Ph.D. thesis, University of Colorado at Denver (June 1995).

[64] M. Delfour, W. Hager, F. Trochu, Discontinuous galerkin methods for ordinary differential equations, *Math. Comp.* 36 (1) (1981) 455–473.

[65] E. Hairer, G. Wanner, Solving Ordinary Differential Equations II. Stiff and Differential-Algebraic Problems, Vol. 14, 1996. doi:[10.1007/978-3-662-09947-6](https://doi.org/10.1007/978-3-662-09947-6).

[66] D. G. Goodwin, H. K. Moffat, r. l. speth, cantera: an object-oriented software toolkit for chemical kinetics, thermodynamics, and transport processes, version 2.4.0 (2018). doi:[10.5281/zenodo.1174508](https://doi.org/10.5281/zenodo.1174508).
URL <http://www.cantera.org>

[67] J. E. Shephard, Explosion dynamics laboratory: Shock and detonation toolbox - 2018 version, *jES* 9-19-2018 (2018).
URL <http://shepherd.caltech.edu/EDL/PublicResources/sdt/>

[68] A. Cuoci, A. Frassoldati, T. Faravelli, E. Ranzi, Numerical modeling of laminar flames with detailed kinetics based on the operator-splitting method, *Energy & Fuels* 27 (12) (2013) 7730–7753. doi:[10.1021/ef4016334](https://doi.org/10.1021/ef4016334).
URL <https://doi.org/10.1021/ef4016334>

[69] H. Wang, X. You, A. V. Joshi, S. G. Davis, A. Laskin, F. L. Egolfopoulos, C. K., Usc mech version ii. high-temperature combustion reaction model of h2/co/c1-c4 compounds (2007).
URL http://ignis.usc.edu/USC_mech_II.htm

[70] J. F. Haas, B. Sturtevant, Interaction of weak-shock waves, *Journal of Fluid Mechanics* 181 (1) (1987) 41 – 76.

[71] J. Quirk, S. Karni, On the dynamics of a shock-bubble interaction, *Journal of Fluid Mechanics* 318 (1996) 129–163. doi:[10.1017/S0022112096007069](https://doi.org/10.1017/S0022112096007069).

[72] A. Marquina, P. Mulet, A flux-split algorithm applied to conservative models for multicomponent compressible flows, *Journal of Computational Physics* 185 (1) (2003) 120 – 138. doi:[https://doi.org/10.1016/S0021-9991\(02\)00050-5](https://doi.org/10.1016/S0021-9991(02)00050-5).

[73] H. Terashima, G. Tryggvason, A front-tracking/ghost-fluid method for fluid interfaces in compressible flows, *Journal of Computational Physics* 228 (11) (2009) 4012 – 4037. doi:<https://doi.org/10.1016/j.jcp.2009.02.023>.

[74] C. K. Westbrook, Chemical kinetics of hydrocarbon oxidation in gaseous detonations, *Combustion and Flame* 46 (1982) 191 – 210. doi:[https://doi.org/10.1016/0010-2180\(82\)90015-3](https://doi.org/10.1016/0010-2180(82)90015-3).

[75] M. H. Lefebvre, J. Weber, J. W., E. S. Oran, Proceedings of the IUTAM Symposium (B. Deshaies and L. F. da Silva, eds.) (30) (1998) 347 – 358.

[76] M. Ó Conaire, H. J. Curran, J. M. Simmie, W. J. Pitz, C. K. Westbrook, A comprehensive modeling study of hydrogen oxidation, *International Journal of Chemical Kinetics* 36 (11) (2004) 603–622. arXiv:<https://onlinelibrary.wiley.com/doi/10.1002/kin.20036>, doi:[10.1002/kin.20036](https://doi.org/10.1002/kin.20036).

[77] C. Geuzaine, J.-F. Remacle, Gmsh: a three-dimensional finite element mesh generator with built-in pre- and post-processing facilities, *International Journal for Numerical Methods in Engineering* (79(11)) (2009) 1310–1331.

[78] K. E. Niemeyer, N. J. Curtis, C.-J. Sung, pyjac: Analytical jacobian generator for chemical kinetics, *Computer Physics Communications* 215 (2017) 188 – 203. doi:<https://doi.org/10.1016/j.cpc.2017.02.004>.

[79] F. Perini, E. Galligani, R. D. Reitz, An analytical jacobian approach to sparse reaction kinetics for computationally efficient combustion modeling with large reaction mechanisms, *Energy & Fuels* 26 (8) (2012) 4804–4822. doi:[10.1021/ef300747n](https://doi.org/10.1021/ef300747n).
URL <https://doi.org/10.1021/ef300747n>

[80] D. Kuzmin, R. Löhner, Flux-Corrected Transport: Principles, Algorithms, and Applications, 2nd Edition, Applied mathematical sciences, Springer-Netherlands, Springer-Verlag New York Inc, 2012. doi:<https://doi.org/10.1007/978-94-007-4038-9>.

[81] A. A. Madja, Compressible fluid flow and systems of conservation laws in several space variables / A. Majda, Vol. 4 of Applied mathematical sciences, Springer-Verlag, Springer-Verlag New York Inc, 1984.

Appendix A. Jacobian of the chemically reacting source term

For brevity we do not present details on the differentiation of the complex reactions found in large chemical mechanisms and instead refer the reader to [78] and [79]. Therefore, in the following we assume

the derivatives of chemical source term, ω_i , with respect to concentrations and temperature, $\frac{\partial \omega_i}{\partial C_j}$ and $\frac{\partial \omega_i}{\partial T}$ are known for all i and j .

The perturbation of the source term is found via the chain rule

$$\delta \mathcal{S} = \mathcal{S}' \delta y = \frac{\partial \mathcal{S}}{\partial T} T' \delta y + \sum_{j=1}^{N_s} \frac{\partial \mathcal{S}}{\partial C_j} C'_j \delta y. \quad (\text{A.1})$$

The first term, $\frac{\partial \mathcal{S}}{\partial T} T' \delta y$, relies on temperature and its implicit relationship to the conserved state, whereas the second term, $\frac{\partial \mathcal{S}}{\partial C_j} C'_j \delta y$, can be extracted from the species elements corresponding to the perturbation,

$$C'_j \delta y = \left(0, \dots, 0, \delta_{j,1}, \dots, \delta_{j,N_s} \right) \begin{pmatrix} \delta \rho v_1 \\ \vdots \\ \delta \rho v_d \\ \delta \rho e_t \\ \delta C_1 \\ \vdots \\ \delta C_{N_s} \end{pmatrix} \begin{cases} \delta_{j,i} = 1 & i = j \\ \delta_{j,i} = 0 & \text{otherwise} \end{cases} = \delta C_j. \quad (\text{A.2})$$

The temperature jacobian, T' , in Equation A.1 is extracted by first applying the chain rule to the definition total energy,

$$\rho e_t = \rho u + \frac{1}{2} \sum_{k=1}^d \rho v_k v_k \quad (\text{A.3})$$

and grouping elements of the state perturbation together. Since temperature is implicitly related to total energy through the internal energy, $\rho u = \sum_{j=1}^{n_s} W_j C_j \sum_{k=1}^{n_p} a_{jk} T^k$, we extract the temperature perturbation by using the derivatives of internal energy, $\frac{\partial \rho u}{\partial T} = \sum_{j=1}^{n_s} W_j C_j \sum_{k=1}^{n_p} k a_{jk} T^{k-1}$ and $\frac{\partial \rho u}{\partial C_j} = W_j \sum_{k=1}^{n_p} a_{jk} T^k$, combined with the perturbations of the kinetic energy,

$$\delta \rho e_t = \frac{\partial \rho u}{\partial T} \delta T + \sum_{j=1}^{n_s} \frac{\partial \rho u}{\partial C_j} \delta C_j + \frac{1}{2} \left(\sum_{k=1}^d (\delta \rho v_k) v_k + \sum_{k=1}^d \rho v_k \delta v_k \right). \quad (\text{A.4})$$

The internal energy derivatives are can be evaluated if the polynomial fits for internal energy have been defined such that they are differentiable. The perturbations of total energy, ρe_t , species, C_k , and momentum, $\delta \rho v_i$, all come from the perturbed state. In order to move forward, we need the velocity perturbation which comes from the following definition,

$$\begin{aligned} v_k &= \frac{\rho v_k}{\rho} \\ \delta v_k &= \frac{\delta \rho v_k}{\rho} - \frac{\rho v_k}{\rho^2} \delta \rho, \end{aligned} \quad (\text{A.5})$$

and the perturbation of density,

$$\begin{aligned} \rho &= \sum_{i=1}^{n_s} W_i C_i \\ \delta \rho &= \sum_{i=1}^{n_s} W_i \delta C_i. \end{aligned} \quad (\text{A.6})$$

By substituting A.5 and A.6 into A.4 we arrive at a total energy perturbation dependent only on the state and temperature perturbations,

$$\delta\rho e_t = \frac{\partial\rho u}{\partial T} \delta T + \sum_{j=1}^{n_s} \frac{\partial\rho u}{\partial C_j} \delta C_j + \sum_{k=1}^d (\delta\rho v_k) v_k - \frac{1}{2\rho} \sum_{k=1}^d v_k v_k \sum_{j=1}^{n_s} W_j \delta C_j.$$

The temperature perturbation is then solved for,

$$\begin{aligned} \delta T = T' \delta y = -\frac{\partial\rho u}{\partial T}^{-1} & \left(\sum_{k=i}^{n_s} \frac{\partial\rho u}{\partial C_i} \delta C_i + \sum_{k=1}^d (\delta\rho v_k) v_k \right. \\ & \left. - \frac{1}{2\rho} \sum_{k=1}^d v_k v_k \sum_{j=1}^{n_s} W_j \delta C_j - \delta\rho e_t \right) \end{aligned} \quad (\text{A.7})$$

and the temperature jacobian is extracted by grouping like terms,

$$\begin{aligned} \delta T = T' \delta y = -\frac{\partial\rho u}{\partial T}^{-1} & \left(v_1, \dots, v_d, -1, \frac{\partial\rho u}{\partial C_1} - \frac{1}{2\rho} \sum_{k=1}^d v_k v_k W_1, \dots, \frac{\partial\rho u}{\partial C_{n_s}} - \frac{1}{2\rho} \sum_{k=1}^d v_k v_k W_{n_s} \right) \begin{pmatrix} \delta\rho v_1 \\ \vdots \\ \delta\rho v_d \\ \delta\rho e_t \\ \delta C_1 \\ \vdots \\ \delta C_{n_s} \end{pmatrix} \\ T' = -\frac{\partial\rho u}{\partial T}^{-1} & (v_1, \dots, v_d, -1, \alpha_1, \dots, \alpha_{n_s}), \end{aligned} \quad (\text{A.8})$$

where

$$\alpha_i = \frac{\partial\rho u}{\partial C_i} - \frac{1}{2\rho} \sum_{k=1}^d v_k v_k W_i. \quad (\text{A.9})$$

We now use A.8 and A.2 together to form the source term jacobian,

$$S' = \frac{dS}{dT} T' + \sum_{j=1}^{n_s} \frac{dS}{dC_j} C'_j = -\frac{\partial\rho u}{\partial T}^{-1} \begin{pmatrix} 0 \\ \vdots \\ 0 \\ 0 \\ \frac{d\omega_1}{dT} \\ \vdots \\ \frac{d\omega_{n_s}}{dT} \end{pmatrix} (v_1, \dots, v_d, -1, \alpha_1, \dots, \alpha_{n_s}) \quad (\text{A.10})$$

$$+ \sum_{j=1}^{n_s} \begin{pmatrix} 0 \\ \vdots \\ 0 \\ \frac{\partial\omega_1}{\partial C_j} \\ \vdots \\ \frac{\partial\omega_{n_s}}{\partial C_j} \end{pmatrix} (0, \dots, 0, 0, \delta_{j,1}, \dots, \delta_{j,n_s}) \begin{cases} \delta_{j,i} = 1 & i = j \\ \delta_{j,i} = 0 & \text{otherwise} \end{cases} \quad (\text{A.11})$$

which gives

$$\mathcal{S}' = \begin{pmatrix} 0 & \dots & 0 & 0 & 0 & \dots & 0 \\ \vdots & \ddots & \vdots & \vdots & \vdots & \ddots & \vdots \\ 0 & \dots & 0 & 0 & 0 & \dots & 0 \\ 0 & \dots & 0 & 0 & 0 & \dots & 0 \\ -\beta_1 v_1 & \dots & -\beta_1 v_d & \beta_1 & \chi_{11} & \dots & \chi_{n_s 1} \\ \vdots & \ddots & \vdots & \vdots & \vdots & \ddots & \vdots \\ -\beta_{n_s} v_1 & \dots & -\beta_{n_s} v_d & \beta_{N_s} & \chi_{1n_s} & \dots & \chi_{n_s n_s} \end{pmatrix} \quad (\text{A.12})$$

where $\beta_i = \frac{\partial \rho u}{\partial T}^{-1} \frac{d\omega_i}{dT}$, $\chi_{ij} = -\alpha_i \beta_j + \frac{\partial \omega_j}{\partial C_i}$, and finally

$$\delta \mathcal{S} = \begin{pmatrix} 0 & \dots & 0 & 0 & 0 & \dots & 0 \\ \vdots & \ddots & \vdots & \vdots & \vdots & \ddots & \vdots \\ 0 & \dots & 0 & 0 & 0 & \dots & 0 \\ 0 & \dots & 0 & 0 & 0 & \dots & 0 \\ -\beta_1 v_1 & \dots & -\beta_1 v_d & \beta_1 & \chi_{11} & \dots & \chi_{n_s 1} \\ \vdots & \ddots & \vdots & \vdots & \vdots & \ddots & \vdots \\ -\beta_{n_s} v_1 & \dots & -\beta_{n_s} v_d & \beta_{N_s} & \chi_{1n_s} & \dots & \chi_{n_s n_s} \end{pmatrix} \begin{pmatrix} \delta \rho v_1 \\ \vdots \\ \delta \rho v_n \\ \delta \rho e_t \\ \delta C_1 \\ \vdots \\ \delta C_{N_s} \end{pmatrix} = \begin{pmatrix} 0 \\ \vdots \\ 0 \\ 0 \\ \frac{\partial \omega_1}{\partial T} \delta T + \sum_{i=1}^{n_s} \frac{\partial \omega_1}{\partial C_i} \delta C_k \\ \vdots \\ \frac{\partial \omega_{N_s}}{\partial T} \delta T + \sum_{i=1}^{n_s} \frac{\partial \omega_{N_s}}{\partial C_i} \delta C_i \end{pmatrix} \quad (\text{A.13})$$

Appendix B. Non-reflecting boundary conditions

The Riemann invariants for the calorically perfect Euler equations with boundary normal, $n = (n_1, \dots, n_d)$, and normal velocity $v_n = \sum_{k=1}^d v_k \cdot n_k$ are specified in Kuzmin et al. [80]

$$w = \left(v_n - \frac{2c}{\bar{\gamma} - 1}, \bar{c}_v \log \left(\frac{p}{\rho^{\bar{\gamma}}} \right), v_{\xi}, v_{\eta}, v_n + \frac{2c}{\bar{\gamma} - 1} \right)^T, \quad (\text{B.1})$$

where v_{ξ} and v_{η} are the velocity components tangential to the boundary surface and $c = \sqrt{\gamma RT}$ is the speed of sound where R is calculated from Equation (2.23). The specific heat at constant volume is $\bar{c}_v = \bar{c}_p - R$. These invariants have the corresponding eigenvalues

$$\Lambda = \text{diag} \{ v_n - c, v_n, v_n, v_n, v_n + c \} \quad (\text{B.2})$$

which determine what is specified at a subsonic inflow and outflow boundary conditions.

For a subsonic outlet $v_n > 0$ and $M < 1$ so $\Lambda_1 = v_n - c$ is negative and requires w_1 to be specified from the prescribed state, y_{∞} , and w_2-w_5 come from the interior state, y^+ ,

$$w_1 = v_{n,\infty} - \frac{2c_{\infty}}{\bar{\gamma}_{\infty} - 1} \quad (\text{B.3})$$

$$w_2 = \bar{c}_v^+ \log \left(\frac{p^+}{(\rho^{\bar{\gamma}})^+} \right) \quad (\text{B.4})$$

$$w_3 = v_{\xi}^+ \quad (\text{B.5})$$

$$w_4 = v_{\eta}^+ \quad (\text{B.6})$$

$$w_5 = v_n^+ + \frac{2c^+}{\bar{\gamma}^+ - 1}. \quad (\text{B.7})$$

The species mass fractions and mole fractions are assumed to be from the interior state which gives $c_\infty = \sqrt{\gamma^+ R^+ T_\infty}$ where T_∞ is specified but the gas properties come from the interior. It is often inconvenient to specify temperature and velocity, which is required for w_1 at an outflow, unless the boundary is specified far enough away to not interfere with the flow. For a downstream outflow condition, the pressure, p_∞ , can be specified and the temperature, T_∞ , can be calculated from a constant entropy process assuming the mole fractions are constant. Here entropy is

$$S = \sum_{i=1}^{n_s} X_i \sum_{k=0}^{n_p} s_{ik} T^k - X_i R \log X_i - X_i R \ln \frac{p}{p_{atm}} \quad (\text{B.8})$$

where s_{ik} are the polynomial coefficients for the species specific entropies. The constant entropy process temperature, T_∂ , is computed such that the following is satisfied to machine precision for a given initial temperature guess:

$$\delta T = \frac{\sum_{i=1}^{n_s} X_i \sum_{k=0}^{n_p} s_{ik} (T^+)^k + R \ln \frac{p_\partial}{p^+} - \sum_{i=1}^{n_s} X_i \sum_{k=0}^{n_p} s_{ik} T_\partial^k}{\frac{\partial S}{\partial T}}, \quad (\text{B.9})$$

where δT is the temperature decrement corresponding to Newton's method and

$$\frac{\partial S}{\partial T} = \sum_{i=1}^{n_s} X_i \sum_{k=1}^K k s_{ik} T_\partial^{k-1}. \quad (\text{B.10})$$

With T_∂ known, $\bar{\gamma}_\partial$ and ρ_∂ can be calculated and the incoming characteristic can be specified,

$$w_1 = w_5 - \frac{4}{\bar{\gamma}_\infty - 1} \sqrt{\frac{\bar{\gamma}_\infty p_\infty}{\rho_\infty}}. \quad (\text{B.11})$$

The thermodynamic state for the boundary is then given by

$$\rho^* = \left(\frac{c_\infty^2}{\bar{\gamma}^+} e^{-\frac{w_2}{c_v^+}} \right)^{\frac{1}{\bar{\gamma}^+ - 1}} \quad (\text{B.12})$$

$$c^* = (\gamma^+ - 1)(w_5 - w_1) \quad (\text{B.13})$$

$$p^* = \frac{\rho^* (c^*)^2}{\bar{\gamma}^+} \quad (\text{B.14})$$

$$T^* = \frac{p^*}{\rho^* R^+} \quad (\text{B.15})$$

$$v^* = \frac{w_1 + w_5}{2} (n_1, \dots, n_d) + v^+ - v_n (n_1, \dots, n_d) \quad (\text{B.16})$$

$$Y_i^* = Y_i^+. \quad (\text{B.17})$$

Likewise, the subsonic inflow requires $w_1 - w_4$ to be specified,

$$w_1 = v_n - \frac{2c_\infty}{\bar{\gamma}_\infty - 1}, \quad (\text{B.18})$$

$$w_2 = c_{v,\partial} \log \left(\frac{p_\infty}{(\rho^{\bar{\gamma}})_\infty} \right), \quad (\text{B.19})$$

$$w_3 = v_{\xi,\infty}, \quad (\text{B.20})$$

$$w_4 = v_{n,\infty}, \quad (\text{B.21})$$

where all the gas properties come from the specified exterior state. The last invariant comes from the interior, $w_5 = v_n^+ + \frac{2c_\infty^+}{\bar{\gamma}^+ - 1}$. This gives the thermodynamic state at the boundary as

$$\rho^* = \rho_\infty \quad (B.22)$$

$$c^* = (\gamma_\infty - 1) \frac{(w_5 - w_1)}{4} \quad (B.23)$$

$$p^* = \frac{\rho^* (c^*)^2}{\gamma_\infty} \quad (B.24)$$

$$T^* = \frac{p^*}{\rho^* \bar{R}_\infty} \quad (B.25)$$

$$v^* = \frac{w_1 + w_5}{2} (n_1, \dots, n_d) + v_\infty - v_n (n_1, \dots, n_d) \quad (B.26)$$

$$Y_i^* = Y_{i,\infty} \quad (B.27)$$

The estimates for the thermodynamic state are used to construct the boundary value,

$$y^* (y^+, y_\infty, n^+) = \left(\rho^* v_1^*, \dots, \rho^* v_n^*, \rho e_t, \frac{\rho^* Y_1^*}{W_i}, \dots, \rho Y_{n_s}^* \right), \quad (B.28)$$

where

$$\rho e_t = \rho u + \frac{1}{2} \sum_{k=1}^d \rho^* v_k^* v_k^* \quad (B.29)$$

with

$$\rho u = \sum_{i=1}^{n_s} W_i C_i \sum_{k=0}^{n_p} a_{ik} (T^*)^k. \quad (B.30)$$

Appendix C. Material discontinuities in multi-component flows

A material discontinuity is defined as a discontinuity across which there is no mass flow. The velocity and pressure are constant across the discontinuity but other material quantities are not. In this appendix we analyze problems involving material interfaces for the formulation presented in this work by considering the non-reacting inviscid formulation of Equations (3.6)-(3.8) where $\mathcal{F}^v(y, \nabla y) = (0, \dots, 0)$ in Equation (2.2) and $\mathcal{S}(y) = (0, \dots, 0)$ in Equation (3.6). A discontinuous solution, in one dimension satisfies, the inviscid form of Equations (3.6)-(3.8) if the jump in the flux is equal to the product of the jump in the state and the material interface velocity [81],

$$\mathcal{F}(y_r) - \mathcal{F}(y_l) = v_s (y_r - y_l), \quad (C.1)$$

where y_r is the state on the right of the discontinuity, y_l is the state on the left of the discontinuity, and v_s is the material velocity normal to the interface.

Below we introduce a material discontinuity by considering a one-dimensional two species discontinuity at x_j where the velocity and pressure are constant and the temperature is discontinuous,

$$\begin{aligned}
v &= \bar{v}, \\
C_1 &= \begin{cases} C_1^0 & \text{if } x > x_j \\ 0 & \text{otherwise} \end{cases}, \\
C_2 &= \begin{cases} 0 & \text{if } x < x_j \\ C_2^0 & \text{otherwise} \end{cases}, \\
T &= \begin{cases} \eta \bar{T} & \text{if } x < x_j \\ \bar{T} & \text{otherwise} \end{cases}, \\
p &= \bar{p}.
\end{aligned}$$

The species with index $i = 1$, species 1, has molecular weight W_1 and the species with index $i = 2$, species 2, has molecular weight W_2 . The initial fluid state from Equation (2.3) is therefore

$$y(x, t=0) = \begin{cases} (W_1 C_1^0 \bar{v}, \frac{1}{2} W_1 C_1^0 \bar{v}^2 + W_1 C_1^0 \sum_{k=0}^{n_p} a_{1k} \bar{T}^k, C_1^0, 0) & x > x_j \\ (W_2 C_2^0 \bar{v}, \frac{1}{2} W_2 C_2^0 \bar{v}^2 + W_2 C_2^0 \sum_{k=0}^{n_p} a_{2k} (\eta \bar{T})^k, 0, C_2^0) & \text{otherwise} \end{cases}. \quad (\text{C.2})$$

Substituting the fluid state from Equation (C.2) in Equation (C.1) we arrive at the following condition

$$W_1 C_1^0 \bar{v}^2 - W_2 C_2^0 \bar{v}^2 = v_s (W_1 C_1^0 v - W_2 C_2^0 v), \quad (\text{C.3})$$

$$\begin{aligned}
\left(\frac{1}{2} W_1 C_1^0 v^2 + C_1^0 W_1 \sum_{k=0}^{n_p} a_{1k} T^k + \bar{p} \right) \bar{v} \\
- \left(\frac{1}{2} W_2 C_2^0 v^2 + C_2^0 W_2 \sum_{k=0}^{n_p} a_{2k} (\eta T)^k + \bar{p} \right) \bar{v} = v_s \left(\frac{1}{2} W_1 C_1^0 v^2 + W_1 C_1^0 \sum_{k=0}^{n_p} a_{1k} T^k \right. \\
\left. - \frac{1}{2} W_2 C_2^0 v^2 - W_2 C_2^0 \sum_{k=0}^{n_p} a_{2k} (\eta T)^k \right), \quad (\text{C.4})
\end{aligned}$$

$$C_1^0 \bar{v} = v_s (C_1^0), \quad (\text{C.5})$$

$$-C_2^0 \bar{v} = v_s (-C_2^0). \quad (\text{C.6})$$

Therefore a material discontinuity where velocity and pressure are constant and the temperature is discontinuous satisfies Equations (3.6)-(3.8) with $v_s = \bar{v}$. A diagram of the space-time solution is shown in Figure C.1a.

We now present the effect of a linear discretization on the same two species discontinuity. Using the notation from Abgrall and Karni [25], the inviscid non-reacting conservation equations can be written as

$$\delta(\rho v) + \nu \Delta(\rho v^2 + p) = 0, \quad (\text{C.7})$$

$$\delta(\rho e_t) + \nu \Delta((\rho e_t + p)v) = 0, \quad (\text{C.8})$$

$$\delta(C_i) + \nu \Delta(C_i v) = 0 \text{ for } i = 1 \dots n_s, \quad (\text{C.9})$$

where the inviscid form of Equation (2.1) has been linearized with respect to space and time. Here, $\delta(\cdot) = (\cdot)_j^{n+1} - (\cdot)_j^n$ denotes the temporal change of the state, $\Delta(\cdot)$ denotes spatial variation across the interface $\Delta(\cdot) = (\cdot)_j^n - (\cdot)_{j-1}^n$, and $\nu = \frac{\Delta t}{\Delta x}$ where Δt is the chosen time step and Δx is the spatial distance across the interface. As in the [25] and [28], $\Delta(\cdot) = (\cdot)_j^n - (\cdot)_{j-1}^n$ is assumed to have the following properties: $\Delta(ab + c) = a(b)_j^n - a(b)_{j-1}^n + (c)_j^n - (c)_{j-1}^n$ for a constant, and b and c not constant. We are deriving

in the context of first order approximations without reconstruction, however, it should be noted that these properties do not always apply to all schemes. The material interface is initially between two nodes, j and $j - 1$, as depicted at time t^n in Figure C.1b. Specifically, the initial flow state at t^n is

$$y_j^n = \left(W_1 C_1^0 \bar{v}, \frac{1}{2} W_1 C_1^0 \bar{v}^2 + W_1 C_1^0 \sum_{k=0}^{n_p} a_{1k} \bar{T}^k, C_1^0, 0 \right), \quad (\text{C.10})$$

$$y_{j-1}^n = \left(W_2 C_2^0 \bar{v}, \frac{1}{2} W_2 C_2^0 \bar{v}^2 + W_2 C_2^0 \sum_{k=0}^{n_p} a_{2k} (\eta \bar{T})^k, 0, C_2^0 \right). \quad (\text{C.11})$$

For simplification purposes, we define the initial concentration of species 2 in terms of the initial concentration of species 1 through the constant initial pressure conditions, $p_j^n = p_{j-1}^n = \bar{p}$, and the equation of state, Equation (2.6),

$$R^o \bar{T} C_1^0 = R^o \eta \bar{T} C_2^0 \rightarrow C_2^0 = \frac{C_1^0}{\eta}. \quad (\text{C.12})$$

The species conservation, Equation (C.9), gives the concentrations at t^{n+1} in terms of the initial species 1 concentration,

$$C_{1,j}^{n+1} = C_1^0 - \nu \bar{v} C_1^0, \quad (\text{C.13})$$

$$C_{2,j}^{n+1} = \nu \bar{v} C_2^0 = \nu \bar{v} \frac{C_1^0}{\eta}. \quad (\text{C.14})$$

Equations (C.13) and (C.14) show that there is numerical mixing of the species at time t^{n+1} and node j , as depicted in Figure C.1b. This is a departure from the exact solution that satisfies the interface condition, depicted in Figure C.1a, and we continue in this section by examining the effect that the numerical mixing of the species concentrations has on the stability of the material interface.

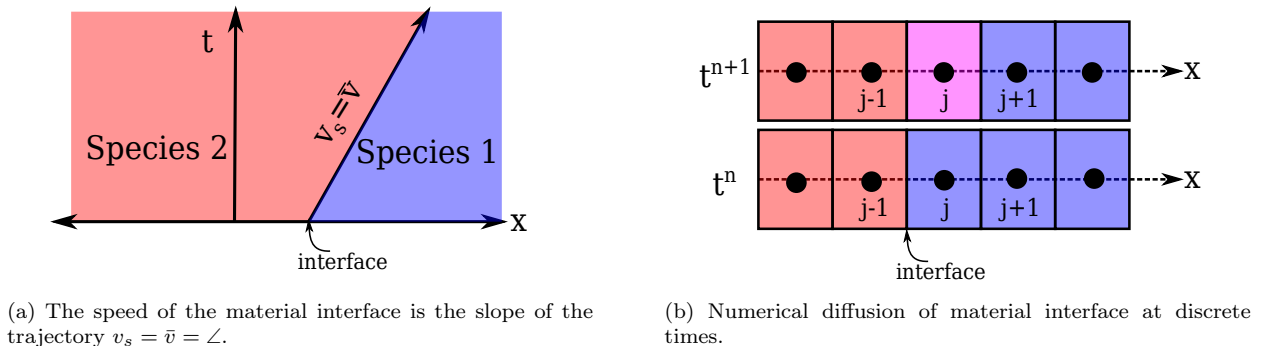


Figure C.1: Diagrams of moving material interfaces.

Substituting the concentrations from Equations (C.13) and (C.14) into Equation (2.4) gives the density at t^{n+1} ,

$$\rho_j^{n+1} = \left(W_1 + \nu \bar{v} \left(\frac{W_2}{\eta} - W_1 \right) \right) C_1^0. \quad (\text{C.15})$$

Using Equations (C.13)-(C.15) and Equation (2.4) for the initial density and substituting into Equation (C.7) reveals that the velocity remains constant,

$$\left(W_1 + \nu \bar{v} \left(\frac{W_2}{\eta} - W_1 \right) \right) C_1^0 v^{n+1} - W_1 C_1^0 \bar{v} + \nu \bar{v}^2 \left(W_1 C_1^0 - W_2 \frac{C_1^0}{\eta} \right) = 0 \rightarrow v_j^{n+1} = \bar{v}. \quad (\text{C.16})$$

Using Equations (C.13)-(C.16) we consider the change in total energy to analyze the stability of the material interface. We derive a relationship for kinetic energy by multiplying Equation (C.7) by $\frac{1}{2} \bar{v}$,

$$\left(\frac{1}{2} \rho_j^{n+1} \bar{v}^2 - \frac{1}{2} \rho_j^n \bar{v}^2 + \nu \bar{v} \left(\frac{1}{2} \rho_j^n \bar{v}^2 - \frac{1}{2} \rho_{j-1}^n \bar{v}^2 \right) \right) = 0, \quad (\text{C.17})$$

and we derive a relationship for pressure by noting pv is constant across the interface at t^n ,

$$\Delta(pv) = 0. \quad (\text{C.18})$$

Combining Equation (C.17) and Equation (C.18) with Equation (C.8) we remove the kinetic energy, contained in $\rho e_t = \rho v^2/2 + \rho u$, and the pressure term to yield a linear relationship for the internal energy across the interface,

$$\delta \rho u + \nu v \Delta(\rho u) = 0. \quad (\text{C.19})$$

We substitute Equation (2.8), Equation (C.12), and Equations (C.13)-(C.15) in Equation (C.19) and arrive at n_p expressions for the temperature at time t^{n+1} by collecting like terms,

$$\begin{aligned} T_j^{n+1} &= \bar{T} \frac{(W_1 a_{11} - \nu \bar{v} (W_1 a_{11} - W_2 a_{21}))}{W_1 (1 - \nu \bar{v}) a_{11} + \frac{W_2}{\eta} (\nu \bar{v}) a_{21}} \\ &\quad \vdots \quad \vdots \quad \vdots \\ (T_j^{n+1})^{n_p} &= (\bar{T})^{n_p} \frac{(W_1 a_{1n_p} - \nu \bar{v} (W_1 a_{1N_p} - W_2 a_{2N_p} \eta^{n_p-1}))}{W_1 (1 - \nu \bar{v}) a_{1n_p} + \frac{W_2}{\eta} (\nu \bar{v}) a_{2n_p}}. \end{aligned} \quad (\text{C.20})$$

Finally, the change in pressure is given as

$$p_j^{n+1} - p_j^n = R^o T_j^{n+1} \left(C_1^0 - \nu \bar{v} C_1^0 + \nu \bar{v} \frac{C_1^0}{\eta} \right) - R^o \bar{T} C_1^0. \quad (\text{C.21})$$

From analyzing Equations (C.20) and (C.21) we come to the same conclusions to those of Jenny et al [21], that pressure oscillations, $p_j^{n+1} - p_j^n \neq 0$, do not exist if one of the following conditions is true

1. The temperature is continuous, $\eta = 1$.
2. The contact discontinuity remains grid aligned, $\nu \bar{v} = 1$.
3. The contact discontinuity is stationary, $\bar{v} = 0$.
4. The internal energies are linear, $n_p = 1$, with respect to temperature *and* the species are the same across the interface, i.e., molecular weights are constant across the interface, $W_1 = W_2$, and the internal energies are the same across the interface, $a_{1k} = a_{2k}$.

For condition (1), the numerical mixing of species concentrations, Equations (C.13) and (C.14), inside the cell does not cause a pressure oscillation as both species are at the same temperature despite having different internal energies.

When $\eta \neq 1$ the temperature is discontinuous and stabilization, e.g., artificial viscosity, would be required if (2)-(4) were not satisfied. Satisfaction of condition (2) would require an interface fitting method [22, 23]

that dynamically fits a priori unknown discontinuities and is therefore beyond the scope of this manuscript. Condition (3) is a trivial case. Condition (4) applies to ideal gases that have a linear relationship between temperature and internal energy and are assumed to be the same species in all regions of the flow.

Applying the same linearization to Equation (2.31) we can arrive at a similar relationship for the internal energy based on $\bar{\gamma}$ and p ,

$$\frac{p_j^{n+1}}{\bar{\gamma}_j^{n+1} - 1} = \frac{\bar{p}}{\bar{\gamma}_1 - 1} - \nu v \left(\frac{\bar{p}}{\bar{\gamma}_1 - 1} - \frac{\bar{p}}{\bar{\gamma}_2 - 1} \right), \quad (\text{C.22})$$

where $\bar{\gamma}_1$ and $\bar{\gamma}_2$ are the known specific heat ratios of the right and left hand side based on C_1^0 at temperature \bar{T} and C_2^0 at temperature $\eta\bar{T}$, respectively. The equivalent process for this formulation would be to use the definition of pressure and $\bar{\gamma}$ in terms of known concentrations, C_1^{n+1} , C_2^{n+1} , C_i^0 , and C_2^0 , and temperatures, $\eta\bar{T}$ and \bar{T} , to solve for T^{n+1} . This results in similar nonlinear relationships for temperature but instead from the h_i polynomials. It follows that the same stability properties found for formulation presented in this work also apply when the formulation is written in terms of specific heats that are computed exactly, i.e., not frozen. However, when $\bar{\gamma}$ is frozen and the temperature is not solved for exactly, pressure oscillations occur according to the analysis of [25].